

# STUDY OF THE FUNDAMENTAL STRUCTURE OF MATTER WITH AN ELECTRON-ION COLLIDER

---

Abhay Deshpande,<sup>1</sup> Richard Milner,<sup>2</sup> Raju Venugopalan,<sup>3</sup>  
and Werner Vogelsang<sup>4</sup>

<sup>1</sup>*Department of Physics & Astronomy, State University of New York at Stony Brook,  
New York 11794 and RIKEN-BNL Research Center, Brookhaven National Laboratory,  
Upton, New York 11973; email: abhay@bnl.gov*

<sup>2</sup>*Physics Department and Laboratory for Nuclear Science, Massachusetts Institute of  
Technology, Cambridge, Massachusetts 02139; email: milner@mit.edu*

<sup>3</sup>*Physics Department, Brookhaven National Laboratory, Upton, New York 11973;  
email: raju@quark.phy.bnl.gov*

<sup>4</sup>*Physics Department and RIKEN-BNL Research Center, Brookhaven National  
Laboratory, Upton, New York 11973; email: vogelsan@quark.phy.bnl.gov*

*This review is dedicated to the memory of Professor Vernon W. Hughes.*

**Key Words** Quantum Chromodynamics, DIS structure functions, Polarized ep Scattering, Nucleon Spin, DIS off Nuclei, Saturation, Color Glass Condensate, EIC, eRHIC

■ **Abstract** We present an overview of the scientific opportunities that would be offered by a high-energy electron-ion collider. We discuss the relevant physics of polarized and unpolarized electron-proton collisions and of electron-nucleus collisions. We also describe the current accelerator and detector plans for a future electron-ion collider.

## CONTENTS

1. INTRODUCTION .....	166
2. STATUS OF THE EXPLORATION OF THE PARTONIC STRUCTURE OF HADRONS AND NUCLEI .....	170
2.1. Deeply-Inelastic Scattering .....	170
2.2. Spin Structure of the Nucleon .....	173
2.3. Nuclear Modifications .....	181
2.4. Space-Time Correlations in QCD .....	187
3. SCIENTIFIC OPPORTUNITIES WITH AN ELECTRON-ION COLLIDER . . . .	190
3.1. Unpolarized e-p Collisions at EIC .....	190
3.2. Polarized <i>ep</i> Collisions at EIC .....	191
3.3. Exploring the Nucleus with an Electron-Ion Collider .....	200

4. ELECTRON-ION COLLIDER-ACCELERATOR ISSUES .....	212
4.1. eRHIC: Ring-Ring Design .....	213
4.2. eRHIC: Linac-Ring Design .....	216
4.3. Other Lepton-Ion Collider Designs: ELIC .....	216
5. DETECTOR IDEAS FOR THE EIC .....	217

## 1. INTRODUCTION

Understanding the fundamental structure of matter is one of the central goals of scientific research. In the closing decades of the twentieth century, physicists developed a beautiful theory, Quantum Chromodynamics (QCD), which explains all of strongly interacting matter in terms of point-like quarks interacting by the exchange of gauge bosons, known as gluons. The gluons of QCD, unlike the photons of QED, can interact with each other. The color force which governs the interaction of quarks and gluons is responsible for more than 99% of the observable mass in the physical universe and explains the structure of nucleons and their composite structures, atomic nuclei, as well as astrophysical objects such as neutron stars.

During the last 30 years, experiments have verified QCD quantitatively in collisions involving a very large momentum exchange between the participants. These collisions occur over very short distances much smaller than the size of the proton. In these experiments, the confined quarks and gluons act as if they are nearly free point-like particles and exhibit many properties that are predicted by perturbative QCD (pQCD). This experimental phenomenon was first discovered in deeply inelastic scattering (DIS) experiments of electrons off nucleons. The discovery resulted in the 1990 Nobel Prize in Physics being awarded to Friedman, Kendall, and Taylor. The phenomenon, that quarks and gluons are quasi-free at short distances, follows from a fundamental property of QCD known as *asymptotic freedom*. Gross, Politzer, and Wilczek, who first identified and understood this unique characteristic of QCD, were awarded the 2004 Nobel Prize in Physics.

When the interaction distance between the quarks and gluons becomes comparable to or larger than the typical size of hadrons, the fundamental constituents of the nucleon are no longer free. They are confined by the strong force that does not allow for the observation of any “colored” object. In this strong coupling QCD regime, where most hadronic matter exists, the symmetries of the underlying quark-gluon theory are hidden, and QCD computations in terms of the dynamical properties of quarks and gluons are difficult. A major effort is underway worldwide to carry out *ab initio* QCD calculations in the strong QCD regime using Monte-Carlo simulations on large scale computers.

The experimental underpinnings for QCD are derived from decades of work at the CERN, DESY, Fermilab, and SLAC accelerator facilities. Some highlights include the determination of the nucleon quark momentum and spin distributions and the nucleon gluon momentum distribution, the verification of the QCD

prediction for the running of the strong coupling constant  $\alpha_s$ , the discovery of jets, and the discovery that quark and gluon momentum distributions in a nucleus differ from those in a free nucleon.

However, thirty years after QCD has been established as the Standard Model of the strong force, and despite impressive progress made in the intervening decades, understanding how QCD works in detail remains one of the outstanding issues in physics. Some crucial open questions that need to be addressed are listed below.

*What is the gluon momentum distribution in the atomic nucleus?* QCD tells us that the nucleon is primarily made up of specks of matter (quarks) bound by tremendously powerful gluon fields. Thus atomic nuclei are primarily composed of glue. Very little is known about the gluon momentum distribution in a nucleon. Determining these gluon distributions is therefore a fundamental measurement of high priority. This quantity is also essential for an understanding of other important questions in hadronic physics. For example, the interpretation of experiments searching for a deconfined quark-gluon state in relativistic heavy ion collisions is dependent on the knowledge of the initial quark and gluon configuration in a heavy nucleus. This will be especially true for heavy ion experiments at the Large Hadron Collider (LHC) at CERN. Further, there are predictions that gluonic matter at high parton densities has novel properties that can be probed in hard scattering experiments on nuclear targets. Hints of the existence of this state may have been seen in Deuteron-Gold experiments at the Relativistic Heavy Ion Collider (RHIC) at Brookhaven.

*How is the spin structure of the nucleon understood to arise from the quark and gluon constituents?* High energy spin-dependent lepton scattering experiments from polarized nucleon targets have produced surprising results. The spins of the quarks account for only about 20% of the spin of the proton. The contribution of the gluons may be large. Dramatic effects are predicted for measurements beyond the capability of any existing accelerator. There are hints from other experiments that the contribution of orbital angular momentum may be large.

*Testing QCD.* It is imperative to continue to subject QCD to stringent tests because there is so much about the theory that remains a mystery. QCD can be tested in two ways: one is by precision measurements, and the other is by looking for novel physics which is sensitive to the confining properties of the theory. Both of these can be achieved at a high luminosity lepton-ion collider with a detector that has a wide rapidity and angular coverage. An example of precision physics is the Bjorken Sum Rule in spin-dependent lepton scattering from a polarized nucleon. This fundamental sum rule relates inclusive spin-dependent lepton scattering to the ratio of axial to vector coupling constants in neutron  $\beta$ -decay. Present experiments test it to about  $\pm 10\%$ : it would be highly desirable to push these tests to about  $\pm 1\%$ . Further, with lattice QCD expected to make substantial progress in the ability to make *ab initio* QCD calculations during the next decade, precise measurements of the calculable observables will be required. An example of a physics measurement sensitive to confinement is hard diffraction, where large mass final states are formed with large “color-less” gaps in rapidity separating them from the hadron or nucleus.

At the Hadron Electron Ring Accelerator (HERA) at DESY, roughly 10% of events are of this nature. The origins of these rapidity gaps, which must be intimately related to the confining properties of the theory, can be better understood with detectors that are able to provide detailed maps of the structure of events in DIS.

This article motivates and describes the next generation accelerator required by nuclear and particle physicists to study and test QCD, namely a polarized leptonion collider. The basic characteristics of the collider are motivated as follows:

- *Lepton beam.* The lepton probe employs the best understood interaction in nature (QED) to study hadron structure. Electrons and positrons couple directly to the quarks. The experimental conditions which maximize sensitivity to valence and sea quarks as well as probe gluons are well understood. Further, the availability of both positron and electron beams will enable experiments that are sensitive to the exchange of the parity violating Z and W-bosons.
- *Range of center-of-mass (CM) energies.* To cleanly interact with quarks, a minimum center-of-mass (CM) energy of about 10 GeV is required. To explore and utilize the powerful  $Q^2$  evolution equations of QCD, CM energies of order 100 GeV are desirable. This consideration strongly motivates the collider geometry.
- *High luminosity.* The QED interaction between the lepton probe and the hadron target is relatively weak. Thus precise and definitive measurements demand a high collision luminosity of order  $10^{33}$  nucleons  $\text{cm}^{-2} \text{s}^{-1}$ .
- *Polarized beams.* Polarized lepton and nucleon beams are essential to address the central question of the spin structure of the nucleon. Both polarized proton and neutron (effectively polarized  $^2\text{H}$  or  $^3\text{He}$ ) are required for tests of the fundamental Bjorken Sum Rule. The polarization direction of at least one of the beams must be reversible on a rapid timescale to minimize systematic uncertainties.
- *Nuclear beams.* Light nuclear targets are useful for probing the spin and flavor content of parton distributions. Heavy nuclei are essential for experiments probing the behavior of quarks and gluons in the nuclear medium.
- *Detector considerations.* The collider geometry has a significant advantage over fixed-target experiments at high energy because it makes feasible the detection of complete final-states. A central collider detector with momentum and energy measurements and particle identification for both leptons and hadrons will be essential for many experiments. Special purpose detectors that provide wide angular and rapidity coverage will be essential for several specific measurements.

These considerations constrain the design parameters of the collider to be a 5 to 10 GeV energy electron (or positron) beam colliding with a nucleon beam of energy 25 GeV to 250 GeV. The collider is anticipated to deliver nuclear beams of energies ranging from 20–100 GeV/nucleon. The lepton and nucleon beams must be highly polarized and the collision luminosity must be of order  $10^{33}$  nucleons  $\text{cm}^{-2} \text{s}^{-1}$ .

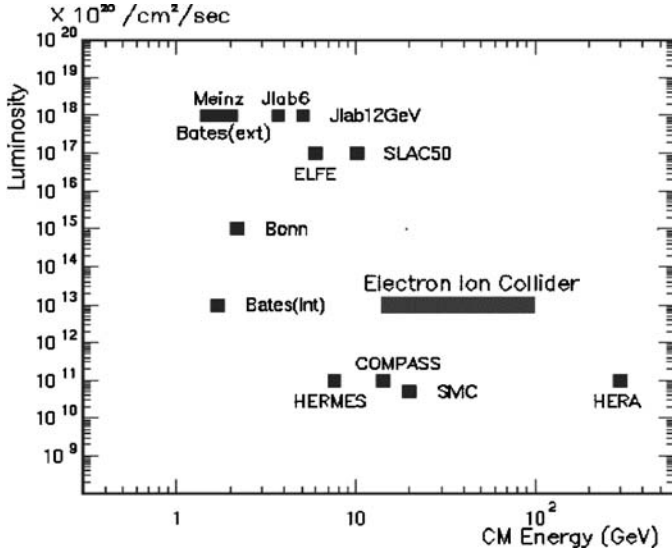


**Figure 1** The center-of-mass energy vs. luminosity of the proposed Electron-Ion Collider eRHIC compared to other lepton scattering facilities.

The proposed eRHIC design (described in Section 4) realizes the required specifications in a cost effective and timely way by using the existing RHIC facility at BNL. The characteristics of eRHIC are well beyond the capability of any existing accelerator, as is clear from Figure 1.

By delivering high energies to the collision, the collider provides an increased range for investigating quarks and gluons with small momentum fraction ( $x$ ) and for studying their behavior over a wide range of momentum transfers ( $Q^2$ ). In deeply inelastic scattering, the accessible values of the Bjorken variable  $x$  (defined in Section 2) are limited by the available CM energy. For example, collisions between a 10 GeV lepton beam and nuclear beams of 100 GeV/nucleon provide access to values of  $x$  as small as  $3 \times 10^{-4}$  for  $Q^2 \sim 1 \text{ GeV}^2$ . In a fixed-target configuration, a 2.1 TeV lepton beam would be required to produce the same CM energy. Figure 2 shows the  $x$ - $Q^2$  range possible with the proposed eRHIC machine and compares that range to the currently explored kinematic region.

In this article, the scientific case and accelerator design for a new facility to study the fundamental quark and gluon structure of strongly interacting matter are presented. Section 2 describes the current understanding of the quark and gluon structure of hadrons and nuclei. Section 3 presents highlights of the scientific opportunities available with a lepton-ion collider. Section 4 describes the accelerator design effort and Section 5 describes the interaction region and eRHIC detector design.

## 2. STATUS OF THE EXPLORATION OF THE PARTONIC STRUCTURE OF HADRONS AND NUCLEI

This section will summarize our current understanding of the partonic structure of hadrons and nuclei in QCD, accumulated during the past three decades from a variety of deeply inelastic and hadronic scattering experiments. We will also comment on what new information may become available from DIS as well as from RHIC and other experimental facilities around the world before a future electron-ion collider starts taking data. We will outline the status of our knowledge on i) the parton distributions in nucleons, ii) spin and flavor distributions in the nucleon, iii) nuclear modifications to the inclusive nucleon distributions such as the European Muon Collaboration (EMC) effect and quark and gluon shadowing, and iv) color coherent phenomena in nuclei that probe the space-time structure of QCD such as color transparency and opacity, partonic energy loss and the  $p_T$  broadening of partons in media. In each case, we will outline the most important remaining questions and challenges. These will be addressed further in Section 3.

### 2.1. Deeply-Inelastic Scattering

The cross-section for the inclusive deeply inelastic scattering (DIS) process shown in Figure 3 can be written as a product of the leptonic tensor  $\mathcal{L}_{\mu\nu}$  and the hadronic tensor  $\mathcal{W}^{\mu\nu}$  as

$$\frac{d^2\sigma}{dx dy} \propto \mathcal{L}_{\mu\nu}(k, q, s) \mathcal{W}^{\mu\nu}(P, q, S), \quad 1.$$

where one defines the Lorentz invariant scalars, the famous Bjorken variable  $x = -q^2/2Pq$ , and  $y = Pq/Pk$ . Note that as illustrated in Figure 3,  $k(k')$  is the 4-momentum of the incoming (outgoing) electron,  $P$  is the 4-momentum of the incoming hadron, and  $q = k - k'$  is the 4-momentum of the virtual photon. The center of mass energy squared is  $s = (P + k)^2$ . From these invariants, one can deduce simply that  $xy \approx Q^2/s$ , where  $Q^2 = -q^2 > 0$ .

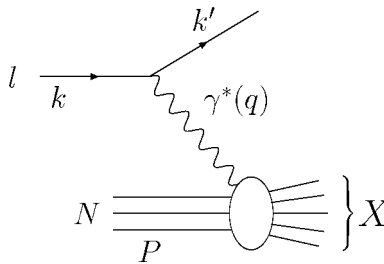


**Figure 3** Deeply-inelastic lepton-nucleon scattering mediated by virtual photon exchange.

The hadronic tensor can be written in full generality as

$$\begin{aligned}
 \mathcal{W}^{\mu\nu}(P, q, S) &= \frac{1}{4\pi} \int d^4z e^{iqz} \langle P, S | [\mathcal{J}_\mu(z), \mathcal{J}_\nu(0)] | P, S \rangle = -g^{\mu\nu} F_1(x, Q^2) \\
 &+ \frac{P^\mu P^\nu}{Pq} F_2(x, Q^2) - i\varepsilon^{\mu\nu\rho\sigma} \frac{q_\rho P_\sigma}{2Pq} F_3(x, Q^2) + i\varepsilon^{\mu\nu\rho\sigma} q_\rho \left[ \frac{S_\sigma}{Pq} g_1(x, Q^2) \right. \\
 &+ \left. \frac{S_\sigma(Pq) - P_\sigma(Sq)}{(Pq)^2} g_2(x, Q^2) \right] + \left[ \frac{P^\mu S^\nu + S^\mu P^\nu}{2Pq} - \frac{Sq}{(Pq)^2} P^\mu P^\nu \right] \\
 &\times g_3(x, Q^2) + \frac{Sq}{(Pq)^2} P^\mu P^\nu g_4(x, Q^2) - \frac{Sq}{Pq} g^{\mu\nu} g_5(x, Q^2). \quad 2.
 \end{aligned}$$

The  $F_i$  are referred to as the ‘‘unpolarized’’ structure functions, whereas the  $g_i$  are the ‘‘spin-dependent’’ ones, because their associated tensors depend on the nucleon spin vector  $S^\mu$ . Note that parity-violating interactions mediated by electroweak boson exchange are required for  $F_3, g_3, g_4, g_5$  to contribute.

Inserting Equation 2 and the straightforwardly calculated leptonic tensor into Equation 1, one obtains the DIS cross section in terms of the structure functions. If one averages over the hadronic spins and restricts oneself to parity conserving (for  $Q^2 \ll M_Z^2$ ) electron-nucleon scattering alone, one finds the simple expression

$$\frac{d^2\sigma}{dx dQ^2} = \frac{2\pi\alpha_{\text{em}}^2}{Q^4} \left[ (1 + (1 - y)^2) F_2(x, Q^2) - y^2 F_L(x, Q^2) \right]. \quad 3.$$

Here,  $\alpha_{\text{em}}$  is the coupling constant of Quantum Electrodynamics and  $F_L$  is the ‘‘longitudinal’’ structure function, defined by the relation  $F_L = F_2 - 2x F_1$ .

In the leading logarithmic approximation of QCD the measured structure function  $F_2(x, Q^2)$  can be written as

$$F_2(x, Q^2) = \sum_{q=u,d,s,c,b,t} e_q^2 (xq(x, Q^2) + x\bar{q}(x, Q^2)), \quad 4.$$

where  $q(x, Q^2)$  ( $\bar{q}(x, Q^2)$ ) is the probability density for finding a quark (anti-quark) with momentum fraction  $x$  at a momentum resolution scale  $Q^2$ ;  $e_q$  is the quark charge.

In the simple parton model one has Bjorken scaling,  $F_2(x, Q^2) \rightarrow F_2(x)$ . The ‘‘scaling violations’’ seen in the  $Q^2$ -dependence of  $F_2(x, Q^2)$  arise from the fact that QCD is not a scale invariant theory and has an intrinsic scale  $\Lambda_{\text{QCD}} \approx 200$  MeV. They are only logarithmic in the Bjorken limit of  $Q^2 \rightarrow \infty$  and  $s \rightarrow \infty$  with  $x \sim Q^2/s$  fixed. As one moves away from the asymptotic regime, the scaling violations become significant. They can be quantitatively computed in QCD perturbation theory using for example the machinery of the operator product expansion and the renormalization group. The result is most conveniently summarized by the Dokshitzer-Gribov-Lipatov-Altarelli-Parisi (DGLAP) evolution equations for the

parton densities (1, 2):

$$\frac{d}{d \ln Q^2} \begin{pmatrix} q \\ g \end{pmatrix} (x, Q^2) = \begin{pmatrix} P_{qq}(\alpha_s, x) & P_{qg}(\alpha_s, x) \\ P_{gq}(\alpha_s, x) & P_{gg}(\alpha_s, x) \end{pmatrix} \otimes \begin{pmatrix} q \\ g \end{pmatrix} (x, Q^2), \quad 5.$$

where  $\otimes$  denotes a convolution, and the  $P_{ij}$  are known as ‘‘splitting functions’’ (2) and are evaluated in QCD perturbation theory. They are now known to three-loop accuracy (3). The evolution of the quark densities  $q, \bar{q}$  involves the gluon density  $g(x, Q^2)$ . The physical picture behind evolution is the fact that the virtuality  $Q^2$  of the probe sets a resolution scale for the partons, so that a change in  $Q^2$  corresponds to a change in the parton state seen. The strategy is then to parameterize the parton distributions at some initial scale  $Q^2 = Q_0^2$ , and to determine the parameters by evolving the parton densities to (usually, larger)  $Q^2$  and by comparing to experimental data for  $F_2(x, Q^2)$ .

The pioneering DIS experiments, which first measured Bjorken scaling of  $F_2$ , were performed at SLAC (4). However, because of the (relatively) small energies, these experiments were limited to the region of  $x \geq 0.1$ . With the intense muon beams of CERN and Fermilab, with energies in excess of 100 GeV, the DIS cross-section of the proton was measured down to and below  $x \sim 10^{-3}$  (5). In the 1990’s, the HERA collider at DESY extended the DIS cross-section of the proton to below  $x = 10^{-4}$  (6, 7). The current experimental determination of  $F_2^{\text{proton}}(x, Q^2)$  extends over 4 orders of magnitude in  $x$  and  $Q^2$ . This is shown in Figure 4. The left panel in Figure 4 shows next-to-leading order (NLO) QCD global fits by the ZEUS and H1 detector collaborations at HERA to  $F_2$  as a function of  $Q^2$  for the world DIS data. The data and the QCD fit are in excellent agreement over a wide range in  $x$  and  $Q^2$ . In the right panel of Figure 4, the  $x$  dependence of  $F_2$  is shown for different bins in  $Q^2$ . The rapid rise in  $F_2$  with decreasing  $x$  reflects the sizeable contribution from the sea quark distribution at small  $x$ .

In Figure 5 we show the valence up and down quark distributions as well as the gluon and sea quark distributions extracted by the H1 and ZEUS collaborations as functions of  $x$  for fixed  $Q^2 = 10 \text{ GeV}^2$ . The valence parton distributions are mainly distributed at large  $x$  whereas the glue and sea quark distributions dominate hugely at small  $x$ . Indeed, the gluon and sea quark distributions are divided by a factor of 20 to ensure they can be shown on the scale of the plot. Already at  $x \sim 0.1$ , the gluon distribution is nearly a factor of two greater than the sum of the up and down quark valence distributions.

As follows from Equation 5, the gluon distribution in DIS may be extracted from scaling violations of  $F_2$ :  $xg(x, Q^2) \propto \frac{\partial F_2(x, Q^2)}{\partial \ln Q^2}$ . As one goes to low  $Q^2$ ,  $xg(x, Q^2)$  becomes small, and some analyses find a preference for a negative gluon distribution at low  $x$ , modulo statistical and systematic uncertainties (9,10). This is in principle not a problem in QCD beyond leading order. However, the resulting longitudinal structure function  $F_L$  also comes out close to zero or even



negative for  $Q^2 \sim 2 \text{ GeV}^2$ ,<sup>1</sup> which is unphysical because  $F_L$  is a positive-definite quantity. A likely explanation for this finding is that contributions to  $F_L$  that are suppressed by inverse powers of  $Q^2$  are playing a significant role at these values of  $Q^2$  (11). These contributions are commonly referred to as higher twist effects.

It has been shown recently (12) that the HERA data on the virtual photon-proton cross-section ( $\sigma^{\gamma^*p} = 4\pi^2\alpha_{\text{em}}F_2(x, Q^2)/Q^2$ ), for all  $x \leq 10^{-2}$  and  $0.045 \leq Q^2 < 450 \text{ GeV}^2$ , exhibit the phenomenon of “geometrical scaling” shown in Figure 6. The data are shown to scale as a function of  $\tau = Q^2/Q_s^2$ , where  $Q_s^2(x) = Q_0^2(x_0/x)^{-\lambda}$  with  $Q_0^2 = 1 \text{ GeV}^2$ ,  $x_0 = 3 \cdot 10^{-4}$  and  $\lambda \approx 0.3$ . The scale  $Q_s^2$  is called the saturation scale. Geometrical scaling, although very general, is realized in a simple model, the Golec-Biernat-Wüsthoff model which includes all twist contributions (13). The model (and variants) provides a phenomenological description of the HERA data on diffractive cross-sections and inclusive vector meson production (14–18). The saturation scale and geometrical scaling will be discussed further in Section 3.

## 2.2. Spin Structure of the Nucleon

2.2.1. WHAT WE HAVE LEARNED FROM POLARIZED DIS Spin physics has played a prominent role in QCD for several decades. The field has been driven by the successful experimental program of polarized deeply-inelastic lepton-nucleon scattering at SLAC, CERN, DESY and the Jefferson Laboratory (19). A main focus has been on measurements with longitudinally polarized lepton beam and target. For leptons with helicity  $\lambda$  scattering off nucleons polarized parallel or antiparallel to the lepton direction, one has (20)

$$\frac{d^2\sigma^{\lambda, \Rightarrow}}{dx dQ^2} - \frac{d^2\sigma^{\lambda, \Leftarrow}}{dx dQ^2} \propto C(G_v, G_a, \lambda) [\lambda xy(2-y)g_1 + (1-y)g_4 + xy^2g_5], \tag{6}$$

where  $C(G_v, G_a, \lambda)$  are factors depending on the vector and axial couplings of the lepton to the exchanged gauge boson. The terms involving  $g_4$  and  $g_5$  in Equation 6 are associated with  $Z$  and  $W$  exchange in the DIS process and violate parity. In the fixed-target regime, pure-photon exchange strongly dominates, and scattering off a longitudinally polarized target determines  $g_1$ . Figure 7 (left) shows a recent compilation (21) of the world data on  $g_1(x, Q^2)$ , for proton, deuteron, and neutron targets. Roughly speaking,  $g_1$  is known about as well now as the unpolarized  $F_2$  was in the mid-eighties, prior to HERA. Figure 7 (right) shows the measured  $Q^2$ -dependence of  $g_1$ ; the predicted scaling violations are visible in the data.

<sup>1</sup>The leading twist expression for  $F_L$  is simply related to  $\alpha_S xg(x, Q^2)$ .

In leading order of QCD,  $g_1$  can be written as

$$g_1(x, Q^2) = \frac{1}{2} \sum_q e_q^2 [\Delta q(x, Q^2) + \Delta \bar{q}(x, Q^2)], \tag{7}$$

where

$$\Delta q \equiv q_{\rightarrow}^{\rightarrow} - q_{\rightarrow}^{\leftarrow} \quad (q = u, d, s, \dots), \tag{8}$$

$q_{\rightarrow}^{\rightarrow}$  ( $q_{\rightarrow}^{\leftarrow}$ ) denoting the number density of quarks of same (opposite) helicity as the nucleon. Clearly, the  $\Delta q(x, Q^2)$ ,  $\Delta \bar{q}(x, Q^2)$  contain information on the nucleon spin structure. Also in the spin-dependent case, QCD predicts  $Q^2$ -dependence of the densities. The associated evolution equations have the same form as Equation 5, but with polarized splitting functions (2, 23, 24). Also, the spin-dependent gluon density  $\Delta g$ , defined in analogy with Equation 8, appears.

The results of a recent QCD analysis (25) of the data for  $g_1(x, Q^2)$  in terms of the polarized parton densities are shown in Figure 8. The shaded bands in the figure give estimates of how well we know the distributions so far. As can be seen, the valence densities are fairly well known and the sea quark densities to some lesser extent. This analysis (25) assumes flavor-SU(3) symmetry for the sea quarks; the actual uncertainties in the individual sea distributions are much larger. Finally, Figure 8 also shows that we know very little about the polarized gluon density. A tendency toward a positive  $\Delta g$  is seen. It is not surprising that the uncertainty in  $\Delta g$  is still large: at LO,  $\Delta g$  enters only through the  $Q^2$ -evolution of the structure function  $g_1$ . Because all polarized DIS experiments thus far have been with fixed targets, the lever arm in  $Q^2$  has been limited. This is also seen in a comparison of Figure 7 with Figure 4.

A particular focus in the analysis of  $g_1$  has been on the integral  $\Gamma_1(Q^2) \equiv \int_0^1 g_1(x, Q^2) dx$ . Ignoring QCD corrections, one has from Equation 7:

$$\Gamma_1 = \frac{1}{12} \Delta \mathcal{A}_3 + \frac{1}{36} \Delta \mathcal{A}_8 + \frac{1}{9} \Delta \Sigma, \tag{9}$$

where

$$\begin{aligned} \Delta \Sigma &= \Delta U + \Delta \bar{U} + \Delta \mathcal{D} + \Delta \bar{\mathcal{D}} + \Delta S + \Delta \bar{S}, \\ \Delta \mathcal{A}_3 &= \Delta U + \Delta \bar{U} - \Delta \mathcal{D} - \Delta \bar{\mathcal{D}}, \\ \Delta \mathcal{A}_8 &= \Delta U + \Delta \bar{U} + \Delta \mathcal{D} + \Delta \bar{\mathcal{D}} - 2(\Delta S + \Delta \bar{S}), \end{aligned} \tag{10}$$

with  $\Delta \mathcal{Q} = \int_0^1 \Delta q(x, Q^2) dx$ , which does not evolve with  $Q^2$  at lowest order. The flavor non-singlet combinations  $\Delta \mathcal{A}_i$  turn out to be proportional to the nucleon matrix elements of the quark non-singlet axial currents,  $\langle P, S | \bar{q} \gamma^\mu \gamma^5 \lambda_i q | P, S \rangle$ . Such currents typically occur in weak interactions, and by SU(3) rotations one may relate the matrix elements to the  $\beta$ -decay parameters  $F$ ,  $D$  of the baryon octet (28, 29). One finds  $\Delta \mathcal{A}_3 = F + D = g_A = 1.267$  and  $\Delta \mathcal{A}_8 = 3F - D \approx 0.58$ .

The first of these remarkable connections between hadronic and DIS physics corresponds to the famous Bjorken sum rule (28),

$$\Gamma_1^p - \Gamma_1^n = \frac{1}{6} \Delta \mathcal{A}_3 [1 + \mathcal{O}(\alpha_s)] = \frac{1}{6} g_A [1 + \mathcal{O}(\alpha_s)], \quad 11.$$

where the superscripts  $p$  and  $n$  denote the proton and neutron respectively. The sum rule has been verified experimentally with about 10% accuracy (19). The QCD corrections indicated in Equation 11 are known (30) through  $\mathcal{O}(\alpha_s^3)$ . Assuming the validity of the sum rule, it can be used for a rather precise determination of the strong coupling constant (31).

Determining  $\Gamma_1$  from the polarized-DIS data, and using the information from  $\beta$ -decays on  $\Delta \mathcal{A}_3$  and  $\Delta \mathcal{A}_8$  as additional input, one may determine  $\Delta \Sigma$ . This quantity is of particular importance because it measures *twice the quark spin contribution to the proton spin*. The analysis reveals a small value  $\Delta \Sigma \approx 0.2$ . The experimental finding that the quarks carry only about 20% of the proton spin has been one of the most remarkable results in the exploration of the structure of the nucleon. Even though the identification of nucleon with parton helicity is not a prediction of QCD (perturbative or otherwise) the result came as a major surprise. It has sparked tremendous theoretical activity and has also been the motivation behind a number of dedicated experiments in QCD spin physics, aimed at further unraveling the nucleon spin.

A small value for  $\Delta \Sigma$  also implies a sizable negative strange quark polarization in the nucleon,  $\Delta S + \Delta \bar{S} \approx -0.12$ . It would be desirable to have independent experimental information on this quantity, to eliminate the uncertainty in the value for  $\Delta \Sigma$  due to SU(3) breaking effects in the determination of  $\Delta \mathcal{A}_8$  from baryon  $\beta$  decays (32). More generally, considering Figure 8, more information is needed on the polarized sea quark distribution functions and their flavor decomposition. Such knowledge is also very interesting for comparisons to model calculations of nucleon structure. For example, there have been a number of predictions (33) for the  $\Delta \bar{u} - \Delta \bar{d}$ . Progress toward achieving a full flavor separation of the nucleon sea has been made recently, through semi-inclusive measurements in DIS (SIDIS) (34, 35). Inclusive DIS via photon exchange only gives access to the combinations  $\Delta q + \Delta \bar{q}$ , as is evident from Equation 7. If one detects, however, a hadron in the final state, the spin-dependent structure function becomes

$$g_1^h(x, z) = \frac{1}{2} \sum_q e_q^2 [\Delta q(x) D_q^h(z) + \Delta \bar{q}(x) D_{\bar{q}}^h(z)]. \quad 12.$$

Here, the  $D_i^h(z)$  are fragmentation functions, with  $z = E^h/\nu$ , where  $E^h$  is the energy of the produced hadron and  $\nu$  the energy of the virtual photon in the Lab frame. Figure 9 shows the latest results on the flavor separation by the HERMES collaboration at HERA (35). Uncertainties are still fairly large; unfortunately, no further improvements in statistics are expected from HERMES. The results are not inconsistent with the large negative polarization of  $\Delta \bar{u} = \Delta \bar{d} = \Delta \bar{s}$  in the sea that has been implemented in many determinations of polarized parton distributions

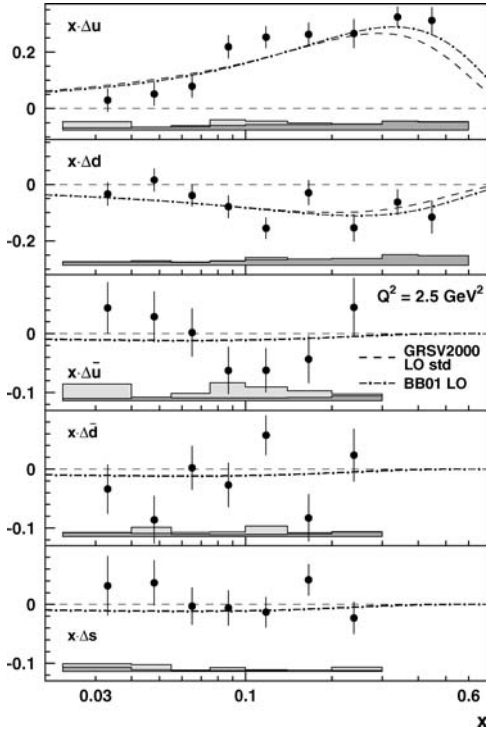


**Figure 9** Recent HERMES results (35) for the quark and antiquark polarizations extracted from semi-inclusive DIS.

from inclusive DIS data (see, e.g., the curves in Figure 8). On the other hand, there is no evidence for a large negative strange quark polarization. The results have sparked much renewed theory activity on SIDIS (36). We note that at RHIC  $W^\pm$  production will be used to determine  $\Delta u$ ,  $\Delta \bar{u}$ ,  $\Delta d$ ,  $\Delta \bar{d}$  with good precision, exploiting the parity-violating couplings of the  $W$  to left-handed quarks and right-handed antiquarks (37). Comparisons of such data taken at much higher scales with those from SIDIS will be extremely interesting.

A measurement of  $\Gamma_1$  obviously relies on an estimate of the contribution to the integral from  $x$  outside the measured region. The extrapolation to small  $x$  constitutes one main uncertainty in the value of  $\Delta\Sigma$ . As can be seen from Figure 7, there is not much information on  $g_1(x, Q^2)$  at  $x < 0.003$ . In addition, the data points at the smaller  $x$  also have  $Q^2$  values that are below the DIS regime, making it conceivable that the “higher-twist” contributions to  $g_1(x, Q^2)$  are important and contaminate the extraction of  $\Delta\Sigma$ . About half of the data points shown in Figure 7 are from the region  $Q^2 \leq 4 \text{ GeV}^2$ ,  $W^2 = Q^2(1-x)/x \leq 10 \text{ GeV}^2$ , which in the unpolarized case is usually excluded in analyses of parton distribution

functions. Clearly, measurements of polarized DIS and SIDIS at smaller  $x$ , as well as at presently available  $x$ , but higher  $Q^2$ , will be vital for arriving at a definitive understanding of the polarized quark distributions, and of  $\Delta\Sigma$  in particular.

**2.2.2. CONTRIBUTORS TO THE NUCLEON SPIN** The partons in the nucleon have to provide the nucleon spin. When formulating a “proton spin sum rule” one has in mind the expectation value of the angular momentum operator (38, 39),

$$\frac{1}{2} = \langle P, 1/2 | \hat{J}_3 | P, 1/2 \rangle = \langle P, 1/2 | \int d^3 [\vec{x} \times \vec{T}]_3 | P, 1/2 \rangle, \quad 13.$$

where  $T^i \equiv T^{0i}$  with  $\mathcal{T}$  the QCD energy-momentum tensor. Expressing the operator in terms of quark and gluon operators, one may write:

$$\frac{1}{2} = \frac{1}{2} \Delta\Sigma + \Delta G(Q^2) + L_q(Q^2) + L_g(Q^2), \quad 14.$$

where  $\Delta G(Q^2) = \int_0^1 \Delta g(x, Q^2)$  is the gluon spin contribution and the  $L_{q,g}$  correspond to orbital angular momenta of quarks and gluons. Unlike  $\Delta\Sigma$ ,  $\Delta G$  and  $L_{q,g}$  depend on the resolution scale  $Q^2$  already at lowest order in evolution. The small size of the quark spin contribution implies that we must look elsewhere for the proton’s spin: sizable contributions to the nucleon spin should come from  $\Delta G$  and/or  $L_{q,g}$ .

Several current experiments are dedicated to a direct determination of  $\Delta g(x, Q^2)$ . High-transverse momentum jet, hadron, and photon final states in polarized  $pp$  scattering at RHIC offer the best possibilities (37). For example, direct access to  $\Delta g$  is provided by the spin asymmetry for the reaction  $pp \rightarrow \gamma X$ , owing to the presence of the QCD Compton process  $qg \rightarrow \gamma q$ . The Spin Muon Collaboration (SMC) and COMPASS fixed-target experiments at CERN, and the HERMES experiment at DESY, access  $\Delta g(x, Q^2)$  in charm or high- $p_T$  hadron pair final states in photon-gluon fusion  $\gamma^* g \rightarrow q\bar{q}$  (40). Additional precision measurements with well established techniques will be needed to determine the integral of the polarized gluon distribution, particularly at lower  $x$ .

Orbital effects are the other candidate for contributions to the proton spin. Close analysis of the  $\vec{x} \times \vec{T}$  matrix elements in Equation 13 revealed (38) that they can be measured from a wider class of parton distribution functions, the so-called generalized parton distributions (GPD) (41). These take the general form  $\langle p + \Delta | \mathcal{O}_{q,g} | p \rangle$ , where  $\mathcal{O}_{q,g}$  are suitable quark and gluon operators and  $\Delta$  is some momentum transfer. The latter is the reason that the GPDs are also referred to as “off-forward” distributions. The explicit factor  $\vec{x}$  in Equation 13 forces one off the forward direction, simply because it requires a derivative with respect to momentum transfer. This is in analogy with the nucleon’s Pauli form factor. In fact, matrix elements of the above form interpolate between DIS structure functions and elastic form factors.

To be more specific (42), the *total* (spin plus orbital) angular momentum contribution of a quark to the nucleon spin is given as (38)

$$J_q = \frac{1}{2} \lim_{\Delta^2 \rightarrow 0} \int dx x [H_q(x, \xi, \Delta^2) + E_q(x, \xi, \Delta^2)]. \quad 15.$$

Here,  $\xi = \Delta^+ / P^+$ , where the light-cone momentum  $\Delta^+ \equiv \Delta^0 + \Delta^z$ , and likewise for  $P^+$ .  $H_q, E_q$  are defined as form factors of the matrix element  $\int dy e^{iyx} \langle P' | \bar{\psi}_+(y) \psi_+(0) | P \rangle$ .  $H_q$  reduces to the ordinary (forward) quark distribution in the limit  $\Delta \rightarrow 0$ ,  $H_q(x, 0, 0) = q(x)$ , whereas the first moments (in  $x$ ) of  $H_q$  and  $E_q$  give the quark's contributions to the nucleon Dirac and Pauli form factors, respectively. In addition, Fourier transforms of  $H_q, E_q$  with respect to the transverse components of the momentum transfer  $\Delta$  give information on the position space distributions of partons in the nucleon (43), for example:

$$H_q(x, \xi = 0, -\vec{\Delta}_\perp^2) = \int d^2\vec{b} e^{-i\vec{\Delta}_\perp \cdot \vec{b}} q(x, b). \quad 16.$$

$q(x, b)$  is the probability density for finding a quark with momentum fraction  $x$  at transverse distance  $\vec{b}$  from the center. It thus gives a transverse profile of the nucleon. GPDs, therefore, may give us remarkably deep new insight into the nucleon.

The classic reaction for a measurement of the  $H_q, E_q$  is “deeply virtual Compton scattering (DVCS),”  $\gamma^* p \rightarrow \gamma p$  (38). It is the theoretically best explored and understood reaction (44). Next-to-leading order calculations are available (45). The GPDs contribute to the reaction at amplitude level. The amplitude for DVCS interferes with that for the Bethe-Heitler process. The pure Bethe-Heitler part of the differential  $ep$  cross-section is calculable and can in principle be subtracted, provided it does not dominate too strongly. Such a subtraction has been performed in DVCS measurements at small  $x$  by H1 and ZEUS (46). A different possibility to eliminate the Bethe-Heitler contribution is to take the difference of cross sections for opposite beam or target polarization. In both cases, contributions from Compton scattering and the Compton-Bethe-Heitler interference survive. The cleanest separation of these pieces can be achieved in experiments with lepton beams of either charge. Because the Compton contribution to the  $ep$  amplitude is linear and the Bethe-Heitler contribution quadratic in the lepton charge, the interference term is projected out in the difference  $d\sigma(e^+p) - d\sigma(e^-p)$  of cross sections, whereas it is absent in their sum. Both the “beam-spin” asymmetry

$$\frac{d\sigma_+(e^-p) - d\sigma_-(e^-p)}{d\sigma_+(e^-p) + d\sigma_-(e^-p)}, \quad 17.$$

where  $\pm$  denote positive (negative) beam helicities, and the “beam-charge” asymmetry

$$\frac{d\sigma(e^+p) - d\sigma(e^-p)}{d\sigma(e^+p) + d\sigma(e^-p)} \quad 18.$$

have been observed (47–49). Figure 10 shows some of the results.

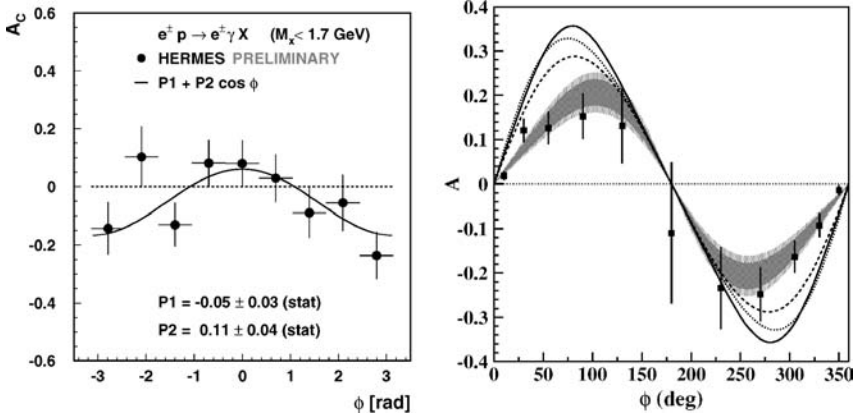


**Figure 10** Data for the beam charge asymmetry in DVCS from HERMES (47) (left) and for the beam spin asymmetry from CLAS (49) (right), as functions of the azimuthal angle  $\phi$ . For the definitions of these asymmetries, see text.

Hard exclusive meson production,  $\gamma^* p \rightarrow Mp$ , is another process that gives access to GPDs, and much activity has gone into this direction as well (42, 50). Both DVCS and exclusive meson production have their practical advantages and disadvantages. Real photon production is cleaner, but the price to be paid is an additional power of  $\alpha_{\text{em}}$ . Meson production may be easier to detect; however, its amplitude is suppressed relatively by a power  $1/Q$ . The importance of using nucleon polarization in off-forward reactions is well established. There have also been first studies for DVCS off nuclei (51).

Practical problems are the fact that GPDs depend on three variables (plus a scale in which they evolve), and that they appear in complicated convolutions with the partonic hard-scattering kernels. We are still far from the quantitative experimental surveys of DVCS and related processes that would allow us to work backwards to new insights into off-diagonal matrix elements and angular momentum. Nevertheless, a direction for the field has been set.

**2.2.3. TRANSVERSE POLARIZATION** In addition to the unpolarized and the helicity-dependent distributions, there is a third set of twist-2 parton distributions, namely transversity (52). In analogy with Equation 8 these distributions measure the net number (parallel minus antiparallel) of partons with transverse polarization in a transversely polarized nucleon:

$$\delta q(x) = q_{\uparrow}^{\uparrow}(x) - q_{\uparrow}^{\downarrow}(x). \quad 19.$$

In a helicity basis (52), transversity corresponds to an interference of an amplitude in which a helicity-+ quark emerges from a helicity-+ nucleon, but is returned as a quark of negative helicity into a nucleon of negative helicity. This helicity-flip

structure makes transversity a probe of chiral symmetry breaking in QCD (53). Perturbative-QCD interactions preserve chirality, and so the helicity flip must primarily come from soft non-perturbative interactions for which chiral symmetry is broken. The required helicity flip also precludes a gluon transversity distribution at leading twist (52).

Measurements of transversity are not straightforward. Again the fact that perturbative interactions in the Standard Model do not change chirality (or, for massless quarks, helicity) means that inclusive DIS is not useful. Collins, however, showed (54) that properties of fragmentation might be exploited to obtain a “transversity polarimeter”: a pion produced in fragmentation will have some transverse momentum with respect to the fragmenting parent quark. There may then be a correlation of the form  $i\vec{S}_T(\vec{P}_\pi \times \vec{k}_\perp)$  among the transverse spin  $\vec{S}_T$  of the fragmenting quark, the pion momentum  $\vec{P}_\pi$ , and the transverse momentum  $\vec{k}_\perp$  of the quark relative to the pion. The fragmentation function associated with this correlation is denoted as  $H_1^{\perp,q}(z)$ , the Collins function. If non-vanishing, the Collins function makes a *leading-power* (54–56) contribution to the single-spin asymmetry  $A_\perp$  in the reaction  $ep^\uparrow \rightarrow e\pi X$ :

$$A_\perp \propto |\vec{S}_T| \sin(\phi + \phi_S) \sum_q e_q^2 \delta q(x) H_1^{\perp,q}(z), \tag{20}$$

where  $\phi(\phi_S)$  is the angle between the lepton plane and the  $(\gamma^*\pi)$  plane (and the transverse target spin). As shown in Equation 20, this asymmetry would then allow access to transversity.

If “intrinsic” transverse momentum in the fragmentation process can play a crucial role in the asymmetry for  $ep^\uparrow \rightarrow e\pi X$ , a natural question is whether  $k_\perp$  in the initial state can be relevant as well. Siverson suggested (57) that the  $k_\perp$  distribution of a quark in a transversely polarized hadron could have an azimuthal asymmetry,  $\vec{S}_T(\vec{P} \times \vec{k}_\perp)$ . It was realized (58, 59) that the Wilson lines in the operators defining the Siverson function, required by gauge invariance, are crucial for the function to be non-vanishing. This intriguing discovery has been one of the most important theoretical developments in QCD spin physics in the past years. Another important aspect of the Siverson function is that it arises as an interference of wave functions with angular momenta  $J_z = \pm 1/2$  and hence contains information on parton orbital angular momentum (58, 60), complementary to that obtainable from DVCS.

Model calculations and phenomenological studies of the Siverson functions  $f_{1T}^{\perp,q}$  have been presented (61). It makes a contribution to  $ep^\uparrow \rightarrow e\pi X$  (55),

$$A_\perp \propto |\vec{S}_T| \sin(\phi - \phi_S) \sum_q e_q^2 f_{1T}^{\perp,q}(x) D_q^\pi(z). \tag{21}$$

This is in competition with the Collins function contribution, Equation 20; however, the azimuthal angular dependence is discernibly different. HERMES has completed a run with transverse polarization and performed an extraction of the contributions from the Siverson and Collins effects (62). There are also first results



from COMPASS (63). First independent information on the Collins functions is now coming from Belle measurements in  $e^+e^-$  annihilation (64). The Collins and Sivers functions are also likely involved (65) in explanations of experimental observations of very large single-transverse spin asymmetries in  $pp$  scattering (66), where none were expected. It was pointed out (59, 67) that comparisons of DIS results and results from  $p^\uparrow p$  scattering at RHIC will be particularly interesting: from the properties of the Wilson lines it follows that the Sivers functions violate universality of the distribution functions. For example, the Sivers functions relevant in DIS and in the Drell-Yan process should have opposite sign. This is a striking prediction awaiting experimental testing.

## 2.3. Nuclear Modifications

The nucleus is traditionally described as a collection of weakly bound nucleons confined in a potential created by their mutual interaction. It came as a surprise when the EMC experiment (68) uncovered a systematic nuclear dependence to the nuclear structure function  $F_2^A(x, Q^2)$  in iron relative to that for Deuterium because the effect was as much as 20% for  $x \sim 0.5$ . This is significantly larger than the effect ( $< 5\%$ ) due to the natural scale for nuclear effects given by the ratio of the binding energy per nucleon to the nucleon mass. Several dedicated fixed target experiments (69–71) confirmed the existence of the nuclear dependence observed by the EMC albeit with significant modifications of the original EMC results at small  $x$ . The upper part of Figure 11 shows an idealized version of the nuclear modification of the relative structure functions per nucleon. It is  $2/A$  times the ratio of a measured nuclear structure function of nucleus  $A$  to that for Deuterium. The rise at the largest values of  $x$  is ascribed to the nucleons' Fermi momentum. The region above  $x \geq 0.2$  is referred to as the EMC effect region. When  $x \leq 0.05$ , the nuclear ratio drops below one and the region is referred to as the nuclear shadowing region, whereas the region with the slight enhancement in between the shadowing and EMC effect regions is called the anti-shadowing region. The lower part of Figure 11 presents a sample of high precision data of ratios of structure functions over a broad range in  $A$ ,  $x$ , and  $Q^2$ . We shall now discuss what is known about these regions, focusing in particular on the EMC effect and nuclear shadowing regions.

**2.3.1. THE EMC EFFECT** A review of the DIS data and various interpretations of the EMC effect since its discovery in the early 1980's can be found in Ref. (73). A common interpretation of the EMC effect is based on models where inter-nucleon interactions at a wide range of inter-nucleon distances are mediated by meson exchanges. The traditional theory (74, 75) of nuclear interactions predicts a net increase in the distribution of virtual pions with increasing nuclear density relative to that of free nucleons. This is because meson interactions are attractive in nuclei. In these models, nuclear pions may carry about 5% of the total momentum to fit the EMC effect at  $x \sim 0.3$ . Each pion carries a light-cone fraction of about 0.2–0.3 of that for a nucleon. Sea anti-quarks belonging to these nuclear pions may scatter

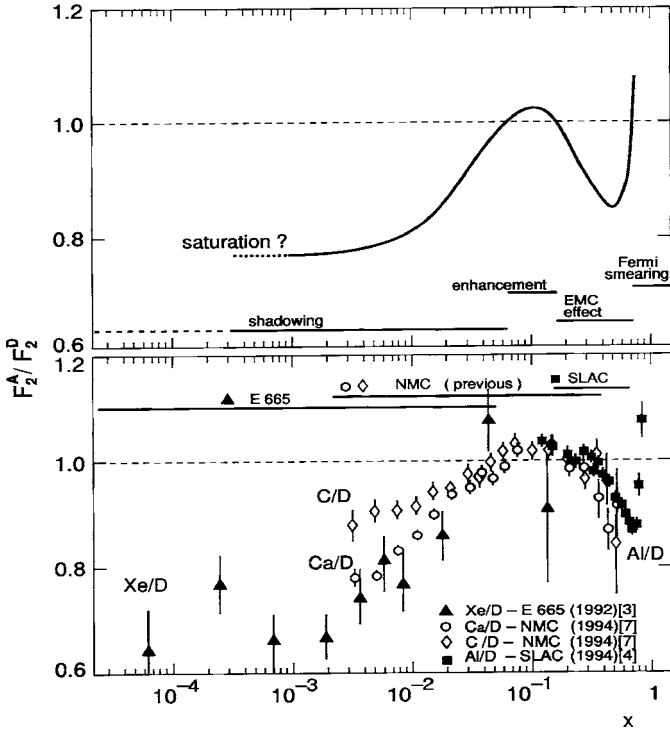


**Figure 11** Upper: An idealized depiction of the ratio of the structure function of a nucleus,  $F_2^A(x, Q^2)$  per nucleon to  $F_2^d(x, Q^2)$  of Deuterium. Lower: Measured  $F_2(x, Q^2)$  structure functions for C, Ca, and Xe relative to Deuterium. From (72).

off a hard probe. Hence the predicted enhancement of the nuclear sea of 10% to 15% for  $x \sim 0.1-0.2$  and for  $A \geq 40$ . The conventional view of nuclear binding is challenged by the constancy with  $A$  of the anti-quark distribution extracted from the production of Drell-Yan pairs in proton-nucleus collisions at Fermilab (76). These data are shown in Figure 12. No enhancement was observed at the level of 1% accuracy in the Drell-Yan experiments. The Drell-Yan data was also compared with and showed good agreement with the DIS EMC data for the  $F_2$  ratio of Tin to Deuterium.

Furthermore, first results (77) from the Jefferson Laboratory (TJNAF) experiment E91-003 indicate that there is no significant pion excess in the  $A(e, e', B)$  reaction. (It has however been pointed out (78) that parameters of pion interactions in nuclei can be readily adjusted to reduce the pion excess to conform with the Drell-Yan data.) In addition, the energy excitation for the residual nuclear system also reduces the contribution of pions to the nuclear parton densities (79). Thus all of these observations suggest that pions may not contribute significantly to  $F_2^A$  in the EMC region.

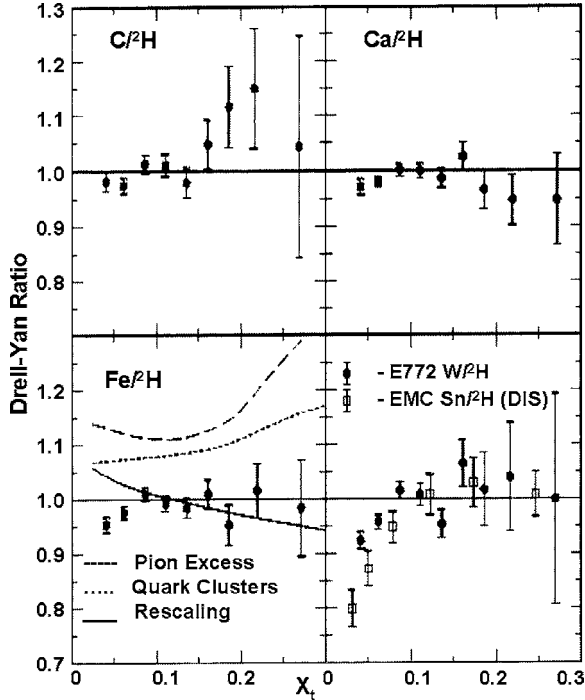


**Figure 12** The ratio of the anti-quark distribution per nucleon in several nuclei relative to Deuterium. Data are shown from a Drell-Yan experiment (76) and compared to theoretical predictions. Also shown is the ratio for Tungsten to Deuterium compared to DIS data from the EMC experiment (68) for the  $F_2$  ratio of Tin to Deuterium.

The chiral quark-soliton model (33) is a phenomenologically successful model that for instance explains the difference in the anti-quark up and down distributions as a function of  $x$  (80). Interestingly, it has been shown recently (80) to simultaneously provide a good description of both the EMC effect and the ratio of anti-quark distributions from Drell-Yan pairs. Recently, it has been argued that a key feature of the EMC effect, the factorization of the  $x$  and  $A$  dependence of the EMC ratio, can be understood in a model independent way in an effective field theory approach (81). Several joint leading order QCD analyses of the nuclear DIS and Drell-Yan data combined with the application of the baryon charge and momentum sum rules (82–85) provide further information on the nuclear effects on parton densities in this kinematic region. These analyses indicate that the valence quark distribution in nuclei is enhanced at  $x \sim 0.1$ – $0.2$ . Gluons in nuclei carry practically the same fraction of the momentum (within 1%) as in a free nucleon. If one assumes that gluon shadowing is similar to that for quarks, these analyses predict a significant enhancement of the gluon distribution in nuclei at  $x \sim 0.1$ – $0.2$  (86). A recent next-to-leading order (NLO) analysis of nuclear parton distributions

(87) however finds that this gluon “anti-shadowing” is much smaller than in the LO analysis.

**2.3.2. NUCLEAR SHADOWING** Nuclear shadowing is the phenomenon, shown in Figure 11, where the ratio of the nuclear electromagnetic structure function  $F_2^A$  relative to  $A/2$  times the Deuteron electromagnetic structure functions  $F_2^D$  is less than unity for  $x \leq 0.05$ . Shadowing is greater for decreasing  $x$  and with increasing nuclear size. For moderately small  $x$ , shadowing is observed to decrease slowly with increasing  $Q^2$ . Unfortunately, because  $x$  and  $Q^2$  are inversely correlated for fixed energies, much of the very small  $x$  data ( $x \leq 10^{-3}$ ) is at very low values of  $Q^2 \leq 1 \text{ GeV}^2$ . In addition, as results (72) from the fixed target E665 experiment at Fermilab and the New Muon Collaboration (NMC) experiment at CERN shown in Figure 11 suggest, good quality data exists only for  $x > 4 \times 10^{-3}$ . At high  $Q^2$ , the shadowing of  $F_2^A$  can be interpreted in terms of shadowing of quark and anti-quark distributions in nuclei at small  $x$ . Information on quark shadowing can also be obtained from proton-nucleus Drell-Yan experiments (88) and from neutrino-nucleus experiments—most recently from NuTeV at Fermilab (89).

The phenomenon of shadowing has different interpretations depending on the frame in which we consider the space-time evolution of the scattering. Consider for instance the rest frame of a nucleus in  $\gamma$ -p/A scattering. The  $\gamma$ p cross-section is only 0.1 mb for energies in excess of 2 GeV, corresponding to a mean-free-path of well over 100 fm in nuclear matter. However, although the high-energy  $\gamma$ A cross-section might be expected to be proportional to  $A$ , the observed increase in the cross-section is smaller than  $A$  times the  $\gamma$ p cross-section. This is because the photon can fluctuate into a  $q\bar{q}$ -pair that has a cross-section typical of the strong interactions ( $\sim 20$  mb) and is absorbed readily (with a mean free path of  $\sim 3.5$  fm). If the fluctuation persists over a length greater than the inter-nucleon separation distance (2 fm), its absorption shadows it from encountering subsequent nucleons. The coherence length of the virtual photon's fluctuation is  $l_{\text{coh.}} \sim 1/2m_N x$  where  $m_N$  is the nucleon mass. Therefore the onset of shadowing is expected and observed at  $x \approx 0.05$ . In this Gribov multiple scattering picture (90), there is a close relation between shadowing and diffraction. The so-called AGK cutting rules (91) relate the first nuclear shadowing correction to the cross-section for diffractively producing a final state in coherent scattering off a nucleon (integrated over all diffractive final states). See Figure 13(a) for an illustration of this correspondence. With these relations (and higher order re-scattering generalizations of these) and with the HERA diffractive DIS data as input, the NMC nuclear shadowing data can be reproduced as shown in the sample computation (92, 93) in Figure 13(b).

In the infinite momentum frame (IMF), shadowing arises due to gluon recombination and screening in the target. When the density of partons in the transverse plane of the nucleus becomes very large, many body recombination and screening effects compete against the growth in the cross-section, leading eventually to a saturation of the gluon density (94). In the IMF picture, one can again use

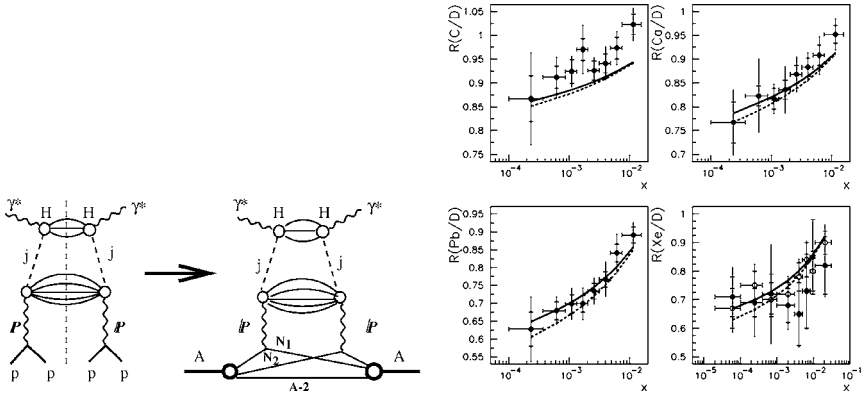


**Figure 13** Left: An illustration of the AGK rules relating shadowing corrections in nuclei to diffractive scattering on nucleons. Right: A calculation (92) which uses AGK to fit nuclear  $F_2$  data using HERA diffractive data. The two curves correspond to two different unitarization prescriptions.

the AGK rules we discussed previously to relate shadowing and diffraction (95), and the result is amenable to a partonic interpretation. The saturation regime is characterized by a scale  $Q_s(x, A)$ , called the saturation scale, which grows with decreasing  $x$  and increasing  $A$ . This saturation scale arises naturally in the Color Glass Condensate (CGC) framework which is discussed in section 3.

A natural consequence of saturation physics is the phenomenon of geometrical scaling. (See for instance the discussion on geometrical scaling of HERA data in section 2.1.) It has been argued that the NMC DIS data also display geometrical scaling (96)—the evidence here albeit interesting is not compelling owing to the paucity of nuclear data over a wide range of  $x$  and  $Q^2$ . It is widely believed that shadowing is a leading twist effect (97, 98), but some of the IMF discussion in the CGC saturation framework suggests higher twist effects are important for  $Q^2 \leq Q_s^2$  because of the large gluon density (99). Constraints from non-linear corrections to the DGLAP framework have also been discussed recently (100). The available data on the  $Q^2$  dependence of shadowing are inconclusive at small  $x$ .

Our empirical definition of shadowing in DIS refers to quark shadowing, likewise for quarks and anti-quarks in the Drell-Yan process in hadronic collisions. In DIS gluon distributions are inferred only indirectly because the virtual photon couples to quarks. The most precise extractions of gluon distributions thus far are from scaling violations of  $F_2^A$ . To do this properly, one needs a wide window in  $x$  and  $Q^2$ . In contrast to the highly precise data on nucleon gluon distributions from HERA, our knowledge of nuclear gluon structure functions ( $g_A(x, Q^2)$ ) is *nearly non-existent*. This is especially so relative to our knowledge of quark distributions in nuclei. The most precise data on the modification of gluon distributions in nuclei come from two NMC high precision measurements of the ratio of the

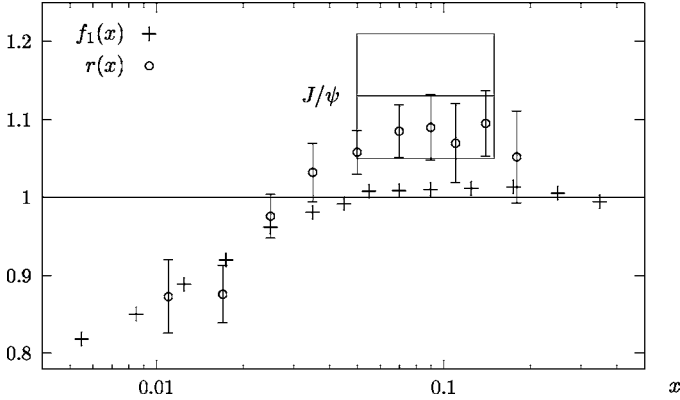


**Figure 14** The ratio  $r(x)$  of the gluon distributions in Sn relative to C and the ratio  $f_1(x)$  of their  $F_2(x)$  structure functions (101). The box represents the extraction of  $r(x)$  from  $J/\psi$  electro-production in the process  $\mu + A \rightarrow \mu + J/\psi + X$ .

scaling violations of the structure functions of Tin (Sn) and Carbon (C). The experiments measure ratios  $f_1 = F_2^{\text{Sn}}/F_2^{\text{C}}$  and  $f_2 = \frac{\partial}{\partial \ln Q^2} f_1$ . The ratio  $r = g_{\text{Sn}}/g_{\text{C}}$  can be determined (101) from  $f_1$  and  $f_2$  and the scaling violations of  $F_2^{\text{Deuterium}}$  (with minimal assumptions). The result for  $r$  is shown in Figure 14. At small  $x$ , gluon shadowing is observed. The trend suggests that gluon shadowing at small  $x$  is greater than that of  $F_2$ , even though the error bars are too large for a conclusive statement.

At larger  $x$  of  $0.1 < x < 0.2$ , one observes anti-shadowing of the gluon distributions. This result from scaling violations can be compared to the ratio of gluon distributions extracted from inclusive  $J/\psi$  production in DIS. The latter assumes the gluon fusion model of  $J/\psi$ -production. The results for  $r$  from the latter method are consistent with those from scaling violations. The large experimental uncertainties however leave the extent of anti-shadowing in doubt. Other measurements of scaling violations for the ratio of  $F_2^{\text{Sn}}/F_2^{\text{C}}$  showed an increase of the ratio with the increase of  $Q^2$  consistent with predictions (82, 83).

The limited data we have may be interpreted to suggest a provocative picture of nuclear parton densities in the  $x \sim 0.1$ – $0.2$  region, which corresponds to distances of  $\sim 1$ – $1.5$  fm, where medium range and short range inter-nucleon forces are expected to be important. In this region, if the gluon and valence quark fields are enhanced while the sea is somewhat suppressed, as some analyses suggest, gluon-induced interactions between nucleons, as well as valence quark interchanges between nucleons, may contribute significantly to nuclear binding (97, 101). Nuclear gluon distributions can also be further constrained by inclusive hadron distributions recently measured by the RHIC experiments (102–105) in Deuteron-Gold scattering at  $\sqrt{s} = 200$  GeV/nucleon. These RHIC results will be discussed in section 3.

## 2.4. Space-Time Correlations in QCD

The space-time picture of DIS processes strongly depends on the value of Bjorken  $x$ . An analysis of electromagnetic current correlators in DIS reveals that one probes the target wave function at space-time points separated by longitudinal distances  $l_{\text{coh.}}$  and transverse distances  $\sim 1/Q$ . At large  $x$  ( $x > 0.2$ ), the virtual photon transforms into a strongly interacting state very close to the active nucleon, typically in the middle of the nucleus. If  $Q^2$  is large enough as well, the produced partonic state interacts weakly with the medium. At smaller  $x$  ( $x < 0.05$ ), the longitudinal length scale  $l_{\text{coh.}}$  exceeds the nuclear size of the heaviest nuclei. At sufficiently small  $x$  ( $x < 0.005$  for the heaviest nuclei) DIS processes undergo several spatially separated stages. First, the virtual photon transforms into a quark-gluon wave packet well before the nucleus. Time dilation ensures that interactions amongst partons in the wave packet are frozen over large distances. (These can be several hundred fermis at EIC energies.) The partons in the wave packet interact coherently and instantaneously with the target. At high energies, these interactions are eikonal in nature and do not affect the transverse size of the wave packet. Finally, the fast components of the wave packet transform into a hadronic final state when well past the nucleus. This interval could be as large as  $2\nu/\mu^2$  where  $\nu$  is the energy of the virtual photon and  $\mu \leq 1$  GeV is a soft hadronic scale.

Space-time studies thus far have been limited to semi-exclusive experiments that investigate the phenomenon of color transparency, and more generic inclusive studies of quark propagation through nuclei. Both these studies involved fixed targets. They are briefly summarized below.

In pQCD, color singlet objects interact weakly with a single nucleon in the target. Additional interactions are suppressed by inverse powers of  $Q^2$ . This phenomenon is called “color transparency” because the nucleus appears transparent to the color singlet projectile (106–108). At very high energies, even the interaction of small color singlet projectiles with nuclei can be large. In this kinematic region, the phenomenon is termed “color opacity” (109, 110). The earliest study of color transparency in DIS was a study of coherent  $J/\psi$  photo-production off nuclei (111). The amplitude of the process at small  $t$  (momentum transfer squared) is approximately proportional to the nuclear atomic number  $A$ . This indicates that the pair that passes through the nucleus is weakly absorbed. For hadronic projectiles, a similar and approximately linear  $A$ -dependence of the amplitude was observed recently for coherent diffraction of 500 GeV pions into two jets (112), consistent with predictions (109).

A number of papers (113–115) predict that the onset of color transparency at sufficiently large  $Q^2$  will give for the coherent diffractive production of vector mesons

$$\frac{d\sigma(\gamma_L^* + A \rightarrow V + A)}{dt} \Big|_{t=0} \propto A^2. \quad 22.$$

For incoherent diffraction at sufficiently large  $t$  ( $> 0.1$  GeV<sup>2</sup>), they predict

$$R(Q^2) \equiv \frac{d\sigma(\gamma_L^* + A \rightarrow V + A')/dt}{A d\sigma(\gamma_L^* + N \rightarrow V + N)/dt} = 1. \quad 23.$$

The first measurements of incoherent diffractive production of vector mesons were performed by the E665 collaboration at Fermilab (116). A significant increase of the nuclear transparency, as reflected in the ratio  $R(Q^2)$ , was observed. The limited luminosity and center-of-mass energy however do not provide a statistically convincing demonstration of color transparency. In addition, the results are complicated by large systematic effects.

Measurements of the inclusive hadron distribution for different final states as a function of the virtual photon energy  $\nu$ , its transverse momentum squared  $Q^2$ , the fraction  $z_h$  of the photon energy carried by the hadron, and the nuclear size  $A$ , provide insight into the propagation of quarks and gluons in nuclear media. In addition to the time and length scales discussed previously, the “formation time”  $\tau_h$  of a hadron is an additional time scale. It is in principle significantly larger than the production time  $1/Q$  of a color singlet parton. If the formation time is large, the “pre-hadron” can multiple scatter in the nucleus, thereby broadening its momentum distribution, and also suffer radiative energy loss before hadronization. The QCD prediction for transverse momentum broadening resulting from multiple scattering is (for quarks) given by the expression (117)

$$\langle \Delta p_{\perp}^2 \rangle = \frac{\alpha_S C_F \pi^2}{2} x g(x, Q^2) \rho L \approx 0.5 \alpha_S \left( \frac{L}{5 \text{ fm}} \right) \text{GeV}^2. \quad 24.$$

Here,  $C_F = 4/3$  is the color Casimir of the quark,  $\rho$  is the nuclear matter density and  $L$  is the length of matter traversed. The Drell-Yan data in Ref. (118) agree with this expression and with the predicted small size of the effect (empirically,  $\langle \Delta p_{\perp}^2 \rangle \sim 0.12 \text{ GeV}^2$  for heavy nuclei). One also observes a large difference in the  $A$  dependence of the transverse momentum of Drell-Yan di-muons relative to those from  $J/\psi$  and  $\Upsilon$  production and decay (119). In the former process only the incident quark undergoes strong interactions, whereas in the latter, the produced vector mesons interact strongly as well. However, the size of the effect and the comparable broadening of the  $J/\psi$  and  $\Upsilon$  (albeit the latter is appreciably smaller than the former) need to be better understood. The  $p_{\perp}$  imbalance of dijets in nuclear photo-production suggests a significantly larger  $p_{\perp}$  broadening effect than in  $J/\psi$  production (120). This suggests non-universal behavior of  $p_{\perp}$  broadening effects but it may also occur from a contamination of the jets by soft fragments. Parton  $p_{\perp}$  broadening due to multiple scattering may also be responsible for the anomalous behavior of inclusive hadron production in hadron-nucleus scattering at moderate  $p_{\perp}$  of a few GeV. In this case, the ratio  $R_{pA}$  of inclusive hadron production in hadron-nucleus scattering to the same process on a nucleon is suppressed at low  $p_{\perp}$  but exceeds unity between 1–2 GeV. This “Cronin effect” (121) was discovered in proton-nucleus scattering experiments in the late 70’s. The flavor dependence of the Cronin effect provided an early hint that scattering of projectile partons off gluons dominates over scattering off quarks (122). The Cronin effect will be



discussed further in section 3 in light of the recent RHIC experiments on Deuteron-Gold scattering (102–105).

The energy loss of partons due to scattering in nuclear matter is complicated by vacuum induced energy loss in addition to the energy loss due to scattering. One computation suggests that vacuum energy loss is the dominant effect (123). For a quark jet, the medium induced energy loss increases quadratically with the length,  $L$ , and is independent of the energy for  $E \rightarrow \infty$ . For  $L = 5$  fm, the asymptotic energy loss,  $\Delta E$ , is estimated to be less than 1 GeV in a cold nuclear medium (117). This makes it difficult to empirically confirm this remarkable  $L$ -dependence of the energy loss. DIS data are qualitatively consistent with small energy loss (124–126). The data indicate that the multiplicity of the leading hadrons is moderately reduced (by 10%) for virtual photon energies of the order of 10–20 GeV for scattering off Nitrogen-14 nuclei. At higher energies, the leading multiplicities gradually become  $A$ -dependent, indicating absorption of the leading partons (125–129).

A pQCD description of partonic energy loss in terms of modified fragmentation functions is claimed to describe HERMES data (131). However, at HERMES energies, and perhaps even at EMC energies, descriptions in terms of hadronic re-scattering and absorption are at least as successful (130, 132). As previously discussed, however, the latter descriptions usually require that the color singlet “pre-hadrons” have a formation time  $\tau_h \sim 0.5$  fm (123, 130, 133). Figure 15 shows the results from one such model as a function of  $z_h$  (the fraction of the parton momentum carried by a hadron) and  $\nu$  (the virtual photon energy) compared to the HERMES data. At EIC energies, a pQCD approach in terms of modified fragmentation functions (134, 135) should be more applicable. The results from these

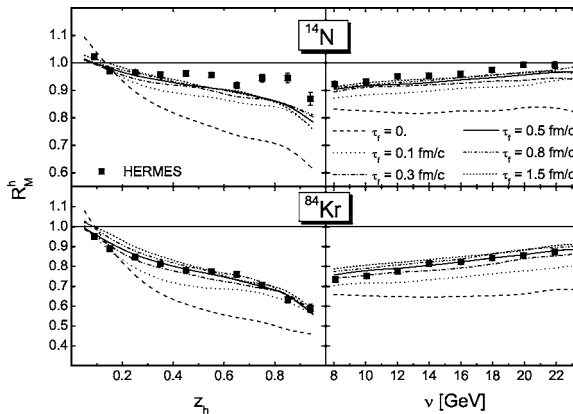


**Figure 15** Data from the HERMES experiment (124) showing the ratio of the inclusive hadron cross section in a nucleus relative to that in a nucleon, plotted as a function a) of  $z_h$ , which is the fraction of the quark’s momentum carried by a hadron, and b) as a function of  $\nu$ , the photon energy, for two different nuclei. Curves denote results of a “pre-hadron” scattering model (130), with differing formation times.

analyses will provide an important test of jet quenching in hot matter descriptions of the RHIC data.

### 3. SCIENTIFIC OPPORTUNITIES WITH AN ELECTRON-ION COLLIDER

This section will discuss the exciting scientific opportunities that will be made possible by the novel features of an electron-ion collider: the high luminosity, the possibility to do scans over a wide range in energy, polarization of the electron and hadronic beams, a range of light and heavy nuclear beams and, not least, the collider geometry of the scattering. Scientific firsts for the electron-ion collider will include a) the first high energy polarized electron-polarized proton collider, and b) the first high energy electron-nucleus collider.

#### 3.1. Unpolarized e-p Collisions at EIC

Unpolarized e-p collisions have been studied extensively most recently at the HERA collider at DESY. In the eRHIC option for an EIC, the center of mass energy in an e-p collision is anticipated to be  $\sqrt{s} = 100$  GeV compared to  $\sqrt{s}$  of over 300 GeV at HERA. Although the  $x$ - $Q^2$  reach of an EIC may not be as large as that of HERA, it has significant other advantages which we will itemize below.

- The current design luminosity is approximately 25 times the design luminosity of HERA. Inclusive observables will be measured with great precision. The additional luminosity will be particularly advantageous for studying semi-inclusive and exclusive final states.
- The EIC (particularly in the eRHIC version) will be able to vary the energies of both the electron and nucleon beams. This will enable a first measurement of  $F_L$  in the small  $x$  regime. The  $F_L$  measurement is very important in testing QCD fits of structure functions.
- Electron-Deuteron collisions, with tagging of spectator nucleons, will allow high precision studies of the flavor dependence of parton distributions.
- An eRHIC detector proposed by Caldwell et al. (136) would have a rapidity coverage nearly twice that of the ZEUS and H1 detectors at HERA. This would allow the reconstruction of the event structure of hard forward jets with and without rapidity gaps in the final state. With this detector, exclusive vector meson and DVCS measurements can be performed for a wider range of the photon-proton center of mass energy squared  $W^2$ . It also permits measurements up to high  $|t|$ , where  $t$  denotes the square of the difference in four-momenta of the incoming and outgoing proton. These will enable a precise mapping of the energy dependence of final states, as well as open a window into the spatial distribution of partons down to very low impact parameters.

We will briefly discuss the physics measurements that can either be done or improved upon with the above enumerated capabilities of EIC/eRHIC. For inclusive measurements,  $F_L$  is clearly a first, “gold plated” measurement. Current QCD fits predict that  $F_L$  is very small (and in some analyses negative) at small  $x$  and small  $Q^2 < 2 \text{ GeV}^2$ . An independent measurement can settle whether this reflects poor extrapolations of data (implying leading twist interpretations of data are still adequate in this regime), or whether higher twist effects are dominant. It will also constrain extractions of the gluon distribution because  $F_L$  is very sensitive to it. Another novel measurement would be that of structure functions in the region of large  $x \approx 1$ . These measurements can be done with  $1 \text{ fb}^{-1}$  of data for up to  $x = 0.9$  and for  $Q^2 < 250 \text{ GeV}^2$ . This kinematic window is completely unexplored to date. These studies can test perturbative QCD predictions of the helicity distribution of the valence partons in a proton (138) as well as the detailed pattern of SU(6) symmetry breaking (139). Moments of structure functions can be compared to lattice data. These should help quantify the influence of higher twist effects. Finally ideas such as Bloom-Gilman duality can be further tested in this kinematic region (140).

At small  $x$ , very little is understood about the quark sea. For instance, the origins of the  $\bar{u} - \bar{d}$  asymmetry and the suppression of the strange sea are not clear. High precision measurements of  $\pi^\pm$ ,  $K^\pm$ ,  $K_s$  and open charm will help separate valence and sea contributions in the small- $x$  region. We have already discussed Generalized Parton Distributions and DVCS measurements. The high luminosity, wide coverage and measurements at high  $|t|$  will quantify efforts to extract a 3-D snapshot of the distribution of partons in the proton.

### 3.2. Polarized $ep$ Collisions at EIC

We expect the EIC to dramatically extend our understanding of the spin structure of the proton through measurements of the spin structure function  $g_1$  over a wide range in  $x$  and  $Q^2$ , of its parity-violating counterparts  $g_4$  and  $g_5$ , of gluon polarization  $\Delta G$ , as well as through spin-dependent semi-inclusive measurements, the study of exclusive reactions, and of polarized photo-production.

**3.2.1. INCLUSIVE SPIN-DEPENDENT STRUCTURE FUNCTION** We have emphasized in Section 2.2.1 the need for further measurements of  $g_1(x, Q^2)$  at lower  $x$  and higher  $Q^2$ . A particularly important reason is that one would like to reduce the uncertainty in the integral  $\Gamma_1(Q^2)$  and hence in  $\Delta\Sigma$ . However, the behavior of  $g_1(x, Q^2)$  at small  $x$  is by itself of great interest in QCD.

At very high energies, Regge theory gives guidance to the expected behavior of  $g_1(x)$ . The prediction (141) is that  $g_1(x)$  is flat or even slightly vanishing at small  $x$ ,  $g_1(x) \propto x^{-\alpha}$  with  $-0.5 \leq \alpha \leq 0$ . It is an open question how far one can increase  $Q^2$  or decrease energy and still trust Regge theory. A behavior of the form  $g_1 \sim x^{-\alpha}$  with  $\alpha < 0$  is unstable under DGLAP evolution (142, 143) in the sense that evolution itself will then govern the small- $x$  behavior at higher  $Q^2$ . Under the assumption that Regge theory expectations are realistic at some (low) scale  $Q_0$  one

then obtains “perturbative predictions” for  $g_1(x, Q^2)$  at  $Q \gg Q_0$ . The fixed-target polarized DIS data indicate that although the non-singlet combination  $g_1^p - g_1^n$  is quite singular at small  $x$ , the singlet piece does appear to be rather flat (142, 144), so that the above reasoning applies here. It turns out that the leading eigenvector of small- $x$  evolution is such that the polarized quark singlet distribution and gluon density become of opposite sign. For a sizeable positive gluon polarization, this leads to the striking feature that the singlet part of  $g_1(x, Q^2)$  is negative at small  $x$  and large  $Q^2$  (142), driven by  $\Delta g$ . Figure 16 shows this dramatic behavior for different values of  $Q^2 = 2, 10, 20, 100 \text{ GeV}^2$  (145). The projected statistical uncertainties at eRHIC, corresponding to  $400 \text{ pb}^{-1}$  integrated luminosity with an almost  $4\pi$  acceptance detector, are also shown. Note that  $400 \text{ pb}^{-1}$  can probably be collected within about one week of e-p running of eRHIC. Thus, at eRHIC one will be well positioned to explore the evolution of the spin structure function  $g_1(x, Q^2)$  at small  $x$ . We note that at small  $x$  and toward  $Q^2 \rightarrow 0$ , one could also study the transition region between the Regge and pQCD regimes (144).

Predictions for the small- $x$  behavior of  $g_1$  have also been obtained from a perturbative resummation of double-logarithms  $\alpha_s^k \ln^{2k}(1/x)$  appearing in the splitting functions (147–150) at small  $x$  in perturbative QCD. Some of these calculations indicate a very singular asymptotic behavior of  $g_1(x)$ . It has been shown (148), however, that subleading terms may still be very important even far below  $x = 10^{-3}$ .

The neutron  $g_1$  structure function could be measured at eRHIC by colliding the electrons with polarized Deuterons or with Helium. If additionally the hadronic proton fragments are tagged, a very clean and direct measurement could be performed. As can be seen from Figure 7, information on  $g_1^n$  at small  $x$  is scarce. The small- $x$  behavior of the isotriplet  $g_1^p - g_1^n$  is particularly interesting for the Bjorken sum rule and because of the steep behavior seen in the fixed-target data (142, 144). It is estimated (151) that an accuracy of the order of 1% could be achieved for the Bjorken sum rule in a running time of about one month. One can also turn this argument around and use the accurate measurement of the non-singlet spin structure function and its evolution to determine the value of the strong coupling constant  $\alpha_s(Q^2)$  (31, 146). This has been tried, and the value one gets from this exercise is comparable to the world average for the strong coupling constant. It is expected that if precision low- $x$  data from the EIC is available and the above mentioned non-singlet structure functions are measured along with their evolutions, this may result in the most accurate value of the strong coupling constant  $\alpha_s(Q^2)$ .

Because of eRHIC’s high energy, very large  $Q^2$  can be reached. Here, the DIS process proceeds not only via photon exchange; also the  $W$  and  $Z$  contribute significantly. Equation 2 shows that in this case new structure functions arising from parity violation contribute to the DIS cross section. These structure functions contain very rich additional information on parton distributions (20, 152, 153). As an example, let us consider charged-current (CC) interactions. Events in the case of  $W$  exchange are characterized by a large transverse momentum imbalance caused by the inability to detect neutrinos from the event. The charge of the  $W$  boson is dictated by that of the lepton beam used in the collision. For  $W^-$  exchange one

then has for the structure functions  $g_1$  and  $g_5$  in Equation 6:

$$g_1^{W^-}(x) = \Delta u(x) + \Delta \bar{d}(x) + \Delta \bar{s}(x), \quad g_5^{W^-}(x) = \Delta u(x) - \Delta \bar{d}(x) - \Delta \bar{s}(x). \quad 25.$$

These appear in the double-spin asymmetry as defined in Ref. (20), where the asymmetry can be expressed in terms of structure functions as

$$A^{W^-} = \frac{2bg_1^{W^-} + ag_5^{W^-}}{aF_1^{W^-} + bF_3^{W^-}}. \quad 26.$$

Here  $a = 2(y^2 - 2y + 2)$ ,  $b = y(2 - y)$  and  $F_3$  is the unpolarized parity-violating structure function of Equation 2. Note that the typical scale in the parton densities is  $M_W$  here. Availability of polarized neutrons and positrons is particularly desirable. For example, one finds at lowest order:

$$g_1^{W^-,p} - g_1^{W^+,p} = \Delta u_v - \Delta d_v \quad 27.$$

$$g_5^{W^+,p} + g_5^{W^-,p} = \Delta u_v + \Delta d_v \quad 28.$$

$$g_5^{W^+,p} - g_5^{W^-,n} = -[\Delta u + \Delta \bar{u} - \Delta d - \Delta \bar{d}]. \quad 29.$$

The last of these relations gives, after integration over all  $x$  and taking into account the first-order QCD correction (152),

$$\int_0^1 dx [g_5^{W^+,p} - g_5^{W^-,n}] = -\left(1 - \frac{2\alpha_s}{3\pi}\right) g_A, \quad 30.$$

equally fundamental as the Bjorken sum rule.

A Monte Carlo study, including the detector effects, has shown that the measurement of the asymmetry in Equation 26 and the parity violating spin structure functions is feasible at eRHIC. Figure 17 shows simulations (154) for the asymmetry and the structure function  $g_5$  for CC events with an electron beam. The luminosity was assumed to be  $2 \text{ fb}^{-1}$ . The simulated data shown are for  $Q^2 > 225 \text{ GeV}^2$ . Similar estimates exist for  $W^+$ . Measuring this asymmetry would require a positron beam. The curves in the figure use the polarized parton distributions of (155). It was assumed that the unpolarized structure functions will have been measured well by HERA by the time this measurement would be performed at eRHIC. Standard assumptions used by the H1 collaboration about the scattered electrons for good detection were applied. The results shown could be obtained (taking into account machine and detector inefficiencies) in a little over one month with the eRHIC luminosity. It is possible that only one or both of the electron-proton and positron-proton collisions could be performed, depending on which design of the accelerator is finally chosen (see Section 4).

**3.2.2. SEMI-INCLUSIVE MEASUREMENTS** As we discussed in Section 2.2.1, significant insights into the nucleon's spin and flavor structure can be gained from semi-inclusive scattering  $ep \rightarrow ehX$ . Knowledge of the identity of the produced

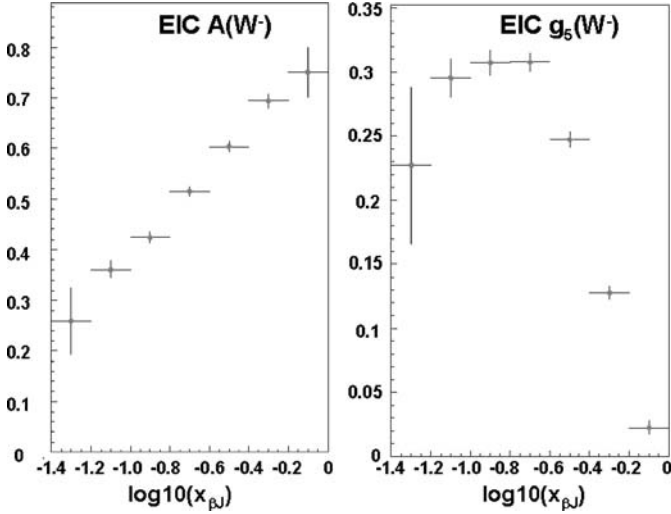


**Figure 17** Simulations (154) for the spin asymmetry  $A^{W^-}$  of Equation 26 and the structure function  $g_5^{W^-}$  as functions of  $\log_{10}(x)$ .

hadrons  $h$  allows separation of the contributions from the different quark flavors. In fixed target experiments, the so-called current hadrons are at forward angles in the laboratory frame. This region is difficult to instrument adequately, especially if the luminosity is increased to gain significant statistical accuracy. A polarized ep collider has the ideal geometry to overcome these shortfalls. The collider kinematics open up the final state into a large solid angle in the laboratory which, using an appropriately designed detector, allows complete identification of the hadronic final state both in the current and target kinematic regions of fragmentation phase space. At eRHIC energies the current and target kinematics are well separated and may be individually studied. At eRHIC higher  $Q^2$  will be available than in the fixed-target experiments, making the observed spin asymmetries less prone to higher-twist effects, and the interpretation cleaner.

Figure 18 shows simulations (156) of the precision with which one could measure the polarized quark and antiquark distributions at the EIC. The events were produced using the DIS generator LEPTO. The plotted uncertainties are statistical only. The simulation was based on an integrated luminosity of  $1 \text{ fb}^{-1}$  for 5 GeV electrons on 50 GeV protons, with both beams polarized to 70%. Inclusive and semi-inclusive asymmetries were analyzed using the leading order “purity” method developed by the SMC (34) and HERMES (35) collaborations. Excellent precision for  $\Delta q/q$  can be obtained down to  $x \approx 0.001$ . The measured average  $Q^2$  values vary as usual per  $x$  bin; they are in the range  $Q^2 = 1.1 \text{ GeV}^2$  at the lowest  $x$  to  $Q^2 \sim 40 \text{ GeV}^2$  at high  $x$ . With proton beams, one has greater sensitivity to up quarks than to down quarks. Excellent precision for the down quark polarizations could be obtained by using Deuteron or Helium beams.

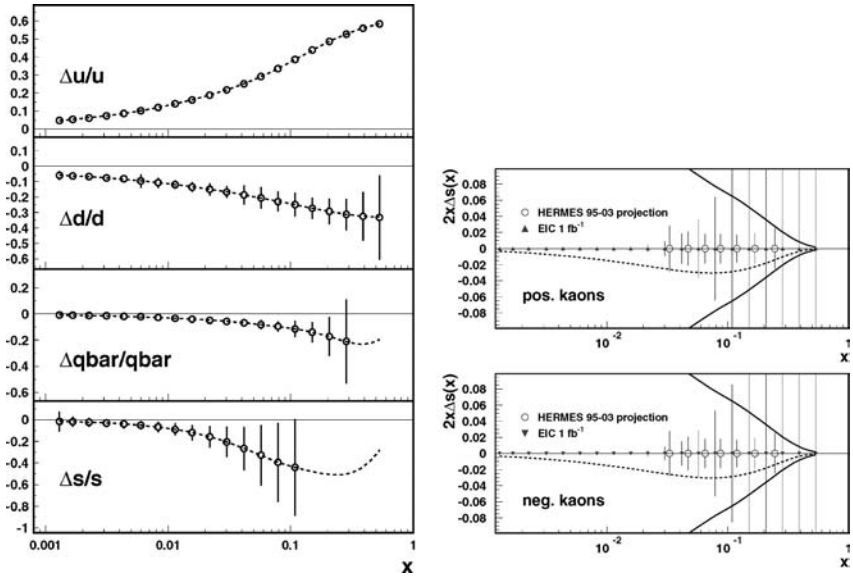


**Figure 18** Left: projected precision of eRHIC measurements of the polarized quark and antiquark distributions (156). Right: expected statistical accuracy of  $\Delta s(x)$  from spin asymmetries for semi-inclusive  $K^\pm$  measurements for  $1 \text{ fb}^{-1}$  luminosity operation of eRHIC, and comparison with the statistical accuracy of the corresponding HERMES measurements.

With identified kaons, and if the up and down quark distributions are known sufficiently well, one will have a very good possibility to determine the strange quark polarization. As we discussed in Section 2.2.1,  $\Delta s(x)$  is one of the most interesting quantities in nucleon spin structure. On the right-hand side of Figure 18, we show results expected for  $\Delta s(x)$  as extracted from the spin asymmetries for  $K^\pm$  production. As in the previous figure, only statistical uncertainties are indicated. The results are compared with the precision available in the HERMES experiment.

There is also much interest in QCD in more refined semi-inclusive measurements. For example, the transverse momentum of the observed hadron may be observed. Here, interesting azimuthal-angle dependences arise at leading twist (56, 157), as we discussed in Subsection 2.2.3. At small transverse momenta, resummations of large Sudakov logarithms are required (158). Measurements at eRHIC would extend previous results from HERA (159) and be a testing ground for detailed studies in perturbative QCD.

3.2.3. MEASUREMENTS OF THE POLARIZED GLUON DISTRIBUTION  $\Delta g(x, Q^2)$  One may extract  $\Delta g$  from scaling violations of the structure function  $g_1(x, Q^2)$ .

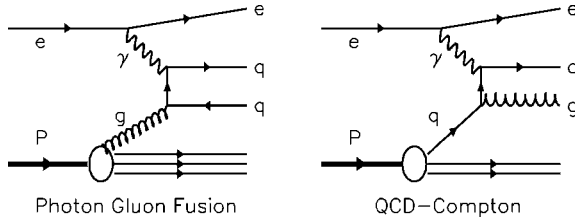


**Figure 19** Feynman diagrams for the photon-gluon fusion and the QCD Compton processes.

Figure 8 shows that indeed some initial information on  $\Delta g(x, Q^2)$  has been obtained in this way, albeit with very poor accuracy. The uncertainty of the integral of  $\Delta g$  is probably about 100% at the moment (31). Measurements at RHIC will vastly improve on this. eRHIC will offer independent and complementary information. Thanks to the large lever arm in  $Q^2$ , and to the low  $x$  that can be reached, scaling violations alone will constrain  $\Delta g(x, Q^2)$  and its integral much better. Studies (160) indicate for example that the total uncertainty on the integral of  $\Delta G$  could be reduced to about 5–10% by measurements at eRHIC with integrated luminosity of  $12 \text{ fb}^{-1}$  ( $\sim 2\text{--}3$  years of eRHIC operation).

Lepton-nucleon scattering also offers direct ways of accessing gluon polarization. Here one makes use of the photon-gluon fusion (PGF) process, for which the gluon appears at leading order. Charm production is one particularly interesting channel (161–163). It was also proposed (162–164) to use jet pairs, produced in the reaction  $\gamma^* g \rightarrow q\bar{q}$ , for a determination of  $\Delta g$ . This process competes with the QCD Compton process,  $\gamma^* q \rightarrow qg$ . Feynman diagrams for these processes are shown in Figure 19.

In the unpolarized case, dijet production has successfully been used at HERA to constrain the gluon density (165). Dedicated studies have been performed for dijet production in polarized collisions at eRHIC (166), using the MEPJET (167) generator. The two jets were required to have transverse momenta  $> 3 \text{ GeV}$ , pseudorapidities  $-3.5 \leq \eta \leq 4$ , and invariant mass  $s_{JJ} > 100 \text{ GeV}^2$ . A  $4\pi$  detector coverage was assumed. The results for the reconstructed  $\Delta g(x)$  are shown in Figure 20, assuming luminosities of  $1 \text{ fb}^{-1}$  (left) and  $200 \text{ pb}^{-1}$  (right). The best probe would be in the region  $0.02 \leq x \leq 0.1$ ; at higher  $x$ , the QCD Compton process becomes dominant. This region is indicated by the shaded areas in the figure. The region  $0.02 \leq x \leq 0.1$  is similar to that probed at RHIC. Measurements at eRHIC would thus allow an independent determination of  $\Delta g$  in a complementary physics environment.

Eventually data for the scaling violations in  $g_1(x, Q^2)$  and for dijet production in DIS will be analyzed jointly. Such a combined analysis would determine the gluon distribution with yet smaller uncertainties. A first preliminary study for eRHIC (168), following the lines of (169), indeed confirms this.



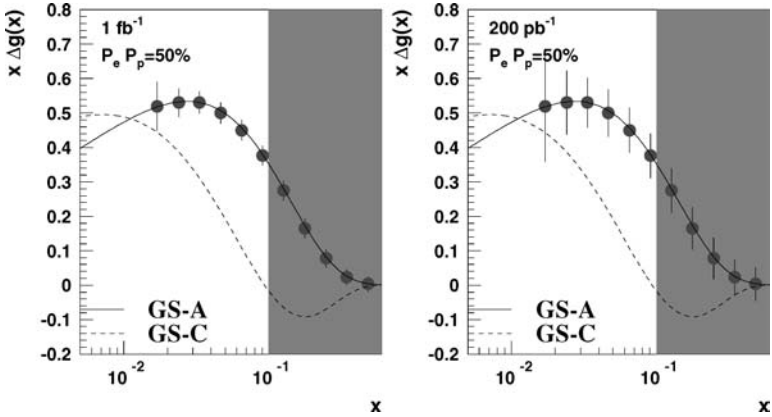


**Figure 20** The statistical precision of  $x \Delta g$  from dijets in LO for eRHIC, for two different luminosities, with predictions for sets A and C of the polarized parton densities of Ref. (155).

3.2.4. EXPLORING THE PARTONIC STRUCTURE OF POLARIZED PHOTONS In the photoproduction limit, when the virtuality of the intermediate photon is small, the  $ep$  cross-section can be approximated by a product of a photon flux and an interaction cross section of the real photon with the proton. Measurements at HERA in the photoproduction limit have led to a significant improvement in our knowledge of the *hadronic structure* of the photon.

The structure of the photon manifests itself in so-called “resolved” contributions to cross sections. We show this in Figure 21 for the case of photoproduction of hadrons. On the left, the photon participates itself in the hard scattering, through “direct” contributions. On the right, the photon behaves like a hadron. This

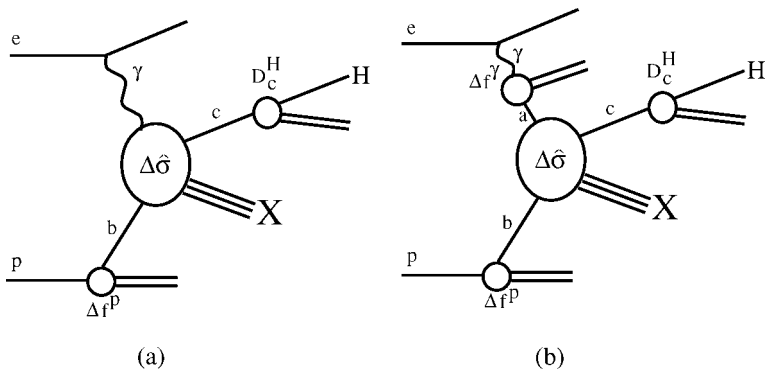


**Figure 21** Generic direct (a) and resolved (b) photon contributions to the process  $lp \rightarrow l'HX$ .

possibility occurs because of (perturbative) short-time fluctuations of the photon into  $q\bar{q}$  pairs and gluons, and because of (non-perturbative) fluctuations into vector mesons  $\rho$ ,  $\phi$ ,  $\omega$  with the same quantum numbers (170). The resolved contributions have been firmly established by experiments in  $e^+e^-$  annihilation and  $ep$  scattering (171).

A unique application of eRHIC would be to study the parton distributions of polarized quasi-real photons, defined as (172, 173)

$$\Delta f^\gamma(x) \equiv f_+^{\gamma+}(x) - f_-^{\gamma+}(x), \tag{31}$$

where  $f_+^{\gamma+}$  ( $f_-^{\gamma+}$ ) denotes the density of a parton  $f = u, d, s, \dots, g$  with positive (negative) helicity in a photon with positive helicity. The  $\Delta f^\gamma(x)$  give information on the spin structure of the photon; they are completely unmeasured so far.

Figure 22 shows samples from studies (174, 175) for observables at eRHIC that would give information on the  $\Delta f^\gamma(x)$ . Two models for the  $\Delta f^\gamma(x)$  were considered (173), one with a strong polarization of partons in the photon (“maximal” set), the other with practically unpolarized partons (“minimal” set). On the left, we show the double-spin asymmetry for photoproduction of high- $p_T$  pions, as a

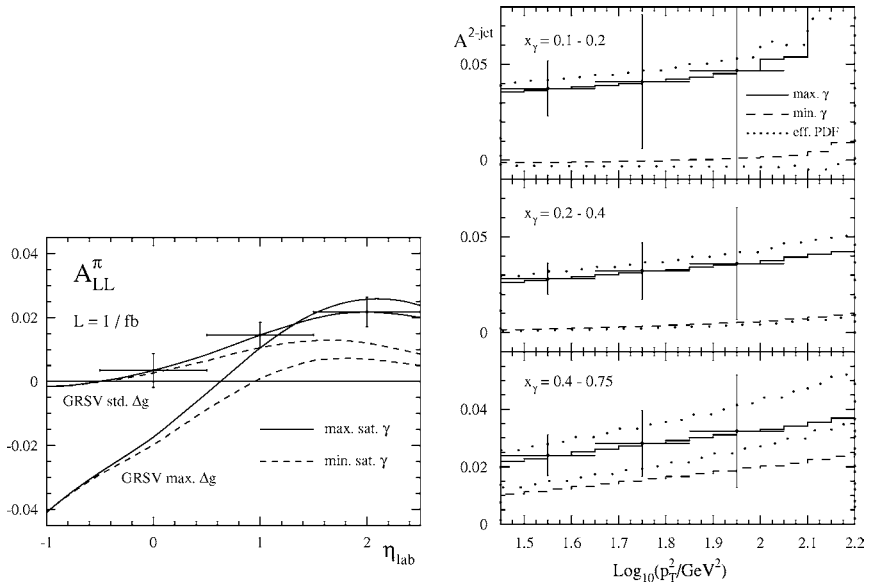


**Figure 22** Left: spin asymmetry for  $\pi^0$  photoproduction in NLO QCD for two sets of polarized photon densities and two different choices of spin-dependent proton distributions. The error bars indicate the statistical accuracy anticipated for eRHIC assuming an integrated luminosity of  $1 \text{ fb}^{-1}$ . Right: spin asymmetry for dijet production as a function of the jet transverse momentum, in three bins of the photon momentum fraction  $x_\gamma$ .

function of the pion’s pseudorapidity  $\eta_{\text{lab}}$  in the eRHIC laboratory frame. The advantage of this observable is that for negative  $\eta_{\text{lab}}$ , in the proton backward region, the photon mostly interacts “directly,” via the process  $\gamma g \rightarrow q\bar{q}$ , whereas its partonic content becomes visible at positive  $\eta_{\text{lab}}$ . This may be seen from the figure, for which we have also used two different sets of polarized parton distributions of the proton (26), mainly differing in  $\Delta g(x)$ .

The right part of Figure 22 shows predictions for the spin asymmetry in dijet photoproduction at eRHIC. If one assumes the jets to be produced by a  $2 \rightarrow 2$  partonic hard scattering, the jet observables determine the momentum fractions  $x_{p,\gamma}$  of the partons in the proton and the photon. Selecting events with  $x_\gamma < 1$ , one therefore directly extracts the “resolved”-photon contribution. At higher orders, this picture is somewhat diluted, but remains qualitatively intact. Such measurements of dijet photoproduction cross sections at HERA (176) have been particularly successful in providing information on photon structure. This makes the spin asymmetry a good candidate for learning about the  $\Delta f^\gamma$  at eRHIC. In the figure we show results for the asymmetry in three different bins of  $x_\gamma$ . One can see that with  $1 \text{ fb}^{-1}$  luminosity one should be able at eRHIC to establish the existence of polarized resolved-photon contributions, and distinguish between our “maximal” and “minimal” photon scenarios. For a first exploration one could also use the approach of “effective” parton densities considered in (174, 176–178).

We finally note that measurements of the polarized total photoproduction cross section at high energies would also give new valuable information on the high-energy contribution to the Drell-Hearn-Gerasimov sum rule (144). The latter relates the total cross sections with photon-proton angular momentum  $3/2$  and  $1/2$  to the anomalous magnetic moments of the nucleon (179):

$$\int_0^\infty \frac{d\nu}{\nu} [\sigma_{3/2}(\nu) - \sigma_{1/2}(\nu)] = \frac{2\pi^2\alpha}{M^2} \kappa^2 = \begin{cases} 204.5 \mu\text{b} & p \\ 232.8 \mu\text{b} & n \end{cases}, \quad 32.$$

where on the right we have given the numerical values of the sum rule. Currently, the experimental result for the proton is a few percent high, and the one for the neutron about 20% low (180). There is practically no information on the contribution to the sum rule from photon energies  $\nu \geq 3 \text{ GeV}$ ; estimates based on Regge theory indicate that it is possible that a substantial part comes from this region. Measurements at eRHIC could give definitive answers here. The H1 and ZEUS detectors at DESY routinely take data using electron taggers situated in the beam pipe 6–44 meters away from the end of the detectors. They detect the scattered electrons from events at very low  $Q^2$  and scattering angles. If electron taggers were included in eRHIC, similar measurements could be performed. The  $Q^2$  range of such measurements at eRHIC is estimated to be  $10^{-8} - 10^{-2} \text{ GeV}^2$ .

**3.2.5. HARD EXCLUSIVE PROCESSES** As we have discussed in Subsection 2.2.2, generalized parton distributions (GPDs) are fundamental elements of nucleon structure. They contain both the parton distributions and the nucleon form

factors as limiting cases, and they provide information on the spatial distribution of partons in the transverse plane. GPDs allow the description of exclusive processes at large  $Q^2$ , among them DVCS. It is hoped that eventually these reactions will provide information on the total angular momenta carried by partons in the proton. See for example Equation 15.

The experimental requirements for a complete investigation of GPDs are formidable. Many different processes need to be investigated at very high luminosities, at large enough  $Q^2$ , with polarization, and with suitable resolution to determine reliably the hadronic final state. The main difficulty, however, for experimental measurements of exclusive reactions is detecting the scattered proton. If the proton is not detected, a “missing-mass” analysis has to be performed. In case of the DVCS reaction, there may be a significant contribution from the Bethe-Heitler process. The amplitude for the Bethe-Heitler process is known and, as we discussed in Subsection 2.2.2, one may construct beam-spin and charge asymmetries to partly eliminate the Bethe-Heitler contribution. Early detector design studies have been performed for the EIC (181). These studies indicate that the acceptance can be significantly increased by adding stations of Silicon-strip-based Roman Pot Detectors away from the central detector in a HERA-like configuration. The detector recently proposed for low- $x$  and low- $Q^2$  studies at the EIC (136) (for details, see Section 5) may also be of significant use to measure the scattered proton. Further studies are underway and will proceed along with iterations of the design of the interaction region and of the beam line.

Although more detailed studies need yet to be performed, we anticipate that the EIC would provide excellent possibilities for studying GPDs. Measurements at the collider will complement those now underway at fixed target experiments and planned with the 12-GeV upgrade at the Jefferson Laboratory (137).

### 3.3. Exploring the Nucleus with an Electron-Ion Collider

In this section, we discuss the scientific opportunities available with the EIC in DIS off nuclei. At very high energies, the correct degrees of freedom to describe the structure of nuclei are quarks and gluons. The current understanding of partonic structure is just sufficient to suggest that their behavior is non-trivial. The situation is reminiscent of Quantum Electrodynamics. The rich science of condensed matter physics took a long time to develop even though the nature of the interaction was well understood. Very little is known about the condensed matter many-body properties of QCD, particularly at high energies. There are sound reasons based in QCD to believe that partons exhibit remarkable collective phenomena at high energies. Because the EIC will be the first electron-ion collider, we will be entering a *terra incognita* in our understanding of the properties of quarks and gluons in nuclei. The range in  $x$  and  $Q^2$  and the luminosity will be greater than at any previous fixed target DIS experiment. Further, the collider environment is ideal for studying semi-inclusive and exclusive processes. Finally, it is expected that a wide range of particle species and beam energies will be available to study

carefully the systematic variation of a wide range of observables with target size and energy.

We will begin our discussion in this section by discussing inclusive “bread and butter” observables such as the inclusive nuclear quark and gluon structure functions. As we observed previously, very little is known about nuclear structure functions at small  $x$  and  $Q^2 \gg \Lambda_{\text{QCD}}^2 \sim 0.04 \text{ GeV}^2$ . This is especially true of the nuclear gluon distribution. We will discuss the very significant contributions that the EIC can make in rectifying this situation. A first will be a reliable extraction of the longitudinal structure function at small  $x$ . Much progress has been made recently in defining universal diffractive structure functions (50, 182, 183). These structure functions can be measured in nuclei for the first time. Generalized parton distributions will help provide a three-dimensional snapshot of the distribution of partons in the nucleus (43).

We will discuss the properties of partons in a nuclear medium and the experimental observables that will enable us to tease out their properties. These include nuclear fragmentation functions that contain valuable information on hadronization in a nuclear environment. The momentum distributions of hadronic final states as functions of  $x$ ,  $Q^2$ , and the fraction of the parton energy carried by a hadron also provide insight into dynamical effects such as parton energy loss in the nuclear medium.

A consequence of small  $x$  evolution in QCD is the phenomenon of parton saturation (94). This arises from the competition between attractive Bremsstrahlung (184) and repulsive screening and recombination (many body) effects (95), which results in a phase space density of partons of order  $1/\alpha_s$ . At such high parton densities, the partons in the wavefunction form a Color Glass Condensate (CGC) for reasons we will discuss later (185). The CGC is an effective theory describing the remarkable universal properties of partons at high energies. It provides an organizing principle for thinking about high energy scattering and has important ramifications for colliders. The evolution of multi-parton correlations predicted by the CGC can be studied with high precision in lepton-nucleus collisions.

Experimental observables measured at the EIC can be compared and contrasted with observables extracted in proton/Deuteron-nucleus and nucleus-nucleus scattering experiments at RHIC and LHC. The kinematic reach of the EIC will significantly overlap with these experiments. Measurements of parton structure functions and multi-parton correlations in the nuclear wave function will provide a deeper understanding of the initial conditions for the formation of a quark gluon plasma (QGP). Final state interactions in heavy ion collisions such as the energy loss of leading hadrons in hot matter (often termed “jet quenching”) are considered strong indicators of the formation of the QGP. The EIC will provide benchmark results for cold nuclear matter which will help quantify energy loss in hot matter. Finally, recent results on inclusive hadron production in RHIC D-Au collisions at 200 GeV/nucleon show hints of the high parton density effects predicted by the CGC. We will discuss these and consider the similarities and differences between a p/D-A and an e-A collider.

3.3.1. NUCLEAR PARTON DISTRIBUTIONS The range of the EIC in  $x$  and  $Q^2$  was discussed previously (see Figure 2). It is significantly larger than for the previous fixed target experiments. The projected statistical accuracy, per inverse picobarn of data, of a measurement of the ratio  $\frac{\partial R}{\partial \ln Q^2}$  versus  $x$  at the EIC relative to data from previous NMC measurements and a hypothetical future e-A collider at HERA energies is shown in Figure 23. Here  $R$  denotes the ratio of nuclear structure functions,  $R = F_2^A/F_2^N$ . As discussed previously, the logarithmic derivative with  $Q^2$  of this ratio can be used to extract the nuclear gluon distribution. The EIC is projected to have an integrated luminosity of several hundred  $\text{pb}^{-1}$  for large nuclei, so one can anticipate high precision measurements of nuclear structure functions at small  $x$ . In particular, because the energy of the colliding beams can be varied, the nuclear longitudinal structure function can be measured for the first time at small  $x$ . At small  $x$  and large  $Q^2$ , it is directly proportional to the gluon distribution. At smaller values of  $Q^2$ , it may be more sensitive to higher twist effects than  $F_2$  (11).

Measurements of nuclear structure functions in the low  $x$  kinematic region will test the predictions of the QCD evolution equations in this kinematic region. The results of QCD evolution with  $Q^2$  depend on input from the structure functions at smaller values of  $Q^2$  for a range of  $x$  values. The data on these is scarce for nuclei. These results are therefore very sensitive to models of the small  $x$  behavior of structure functions at low  $Q^2$ . A nice plot from Ref. (187) reproduced in Figure 24 clearly illustrates the problem. Figure 24 shows results from theoretical models for the ratio of the gluon distribution in Lead to that in a proton as a function of  $x$ . Though all the models employ the same QCD evolution equations, the range in uncertainty is rather large at small  $x$ —about a factor of 3 at  $x \sim 10^{-4}$ . Although one can try to construct better models, the definitive constraint can only come from experiment.

The shadowing of gluon distributions shown in Figure 24 is not understood in a fundamental way. We list here some relevant questions which can be addressed by a future electron-ion collider.

- Is shadowing a leading twist effect; namely, is it unsuppressed by a power of  $Q^2$ ? Most models of nuclear structure functions at small  $x$  assume this is the case. (For a review, see Ref. (98).) Is there a regime of  $x$  and  $Q^2$ , where power corrections due to high parton density effects can be seen? (94, 95, 193).
- What is the relation of shadowing to parton saturation? As we will discuss, parton saturation dynamically gives rise to a semi-hard scale in nuclei. This suggests that shadowing at small  $x$  can be understood in a weak coupling analysis.
- Is there a minimum to the shadowing ratio for fixed  $Q^2$  and  $A$  with decreasing  $x$ ? If so, is it reached faster for gluons or for quarks?
- The Gribov relation between shadowing and diffraction that we discussed previously is well established at low parton densities. How is it modified

at high parton densities? The EIC can test this relation directly by measuring diffractive structure functions in ep (and e-A) and shadowing in e-A collisions.

- Is shadowing universal? For instance, would gluon parton distribution functions extracted from p-A collisions at RHIC be identical to those extracted from e-A in the same kinematic regime? The naive assumption that this is the case may be false if higher twist effects are important. Later in this review, we will discuss the implications of the possible lack of universality for p-A and A-A collisions at the LHC.

We now turn to a discussion of diffractive structure functions. At HERA, hard diffractive events were observed where the proton remained intact and the virtual photon fragmented into a hard final state producing a large rapidity gap between the projectile and target. A rapidity gap is a region in rapidity essentially devoid of particles. In pQCD, the probability of a gap is exponentially suppressed as a function of the gap size. At HERA though, gaps of several units in rapidity are relatively unsuppressed; one finds that roughly 10% of the cross-section corresponds to hard diffractive events with invariant masses  $M_X > 3$  GeV. The remarkable nature of this result is transparent in the proton rest frame: a 50 TeV electron slams into the proton and, 10% of the time, the proton is unaffected, even though the interaction causes the virtual photon to fragment into a hard final state.

The interesting question in diffraction is the nature of the color singlet object (the ‘‘Pomeron’’) within the proton that interacts with the virtual photon. This interaction probes, in a novel fashion, the nature of confining interactions within hadrons. (We will discuss later the possibility that one can study in diffractive events the interplay between strong fields produced by confining interactions and those generated by high parton densities.) In hard diffraction, because the invariant mass of the final state is large, one can reasonably ask questions about the quark and gluon content of the Pomeron. A diffractive structure function  $F_{2,A}^{D(4)}$  can be defined (182, 183, 194), in a fashion analogous to  $F_2$ , as

$$\frac{d^4\sigma_{eA \rightarrow eXA}}{dx_{Bj}dQ^2dx_p dt} = A \cdot \frac{4\pi\alpha_{\text{em}}^2}{xQ^4} \left\{ 1 - y + \frac{y^2}{2[1 + R_A^{D(4)}(\beta, Q^2, x_p, t)]} \right\} \times F_{2,A}^{D(4)}(\beta, Q^2, x_p, t), \quad 33.$$

where,  $y = Q^2/sx_{Bj}$ , and analogously to  $F_2$ , one has  $R_A^{D(4)} = F_L^{D(4)}/F_T^{D(4)}$ . Further,  $Q^2 = -q^2 > 0$ ,  $x_{Bj} = Q^2/2Pq$ ,  $x_p = q(P - P')/qP$ ,  $t = (P - P')^2$  and  $\beta = x_{Bj}/x_p$ . Here  $P$  is the initial nuclear momentum, and  $P'$  is the net momentum of the fragments  $Y$  in the proton fragmentation region. Similarly,  $M_X$  is the invariant mass of the fragments  $X$  in the electron fragmentation region. An illustration of the hard diffractive event is shown in Figure 25.

It is more convenient in practice to measure the structure function  $F_{2,A}^{D(3)} = \int F_{2,A}^{D(4)} dt$ , where  $|t_{\min}| < |t| < |t_{\max}|$ , where  $|t_{\min}|$  is the minimal momentum transfer to the nucleus, and  $|t_{\max}|$  is the maximal momentum transfer to the

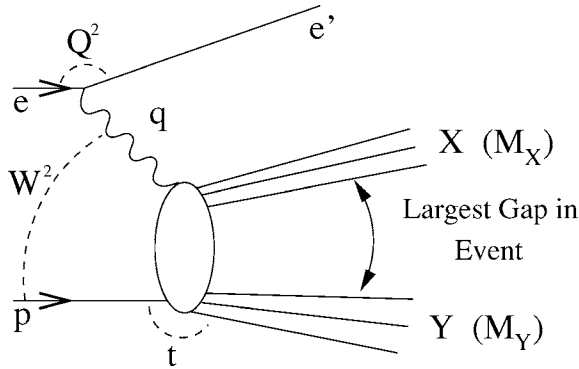


**Figure 25** The diagram of a process with a rapidity gap between the systems X and Y. The projectile nucleus is denoted here as p. Figure from Ref. (195).

nucleus that still ensures that the particles in the nuclear fragmentation region Y are undetected. An interesting quantity to measure is the ratio  $R_{A1,A2}(\beta, Q^2, x_p) = \frac{F_{2,A1}^{D(3)}(\beta, Q^2, x_p)}{F_{2,A2}^{D(3)}(\beta, Q^2, x_p)}$ . The A-dependence of this quantity will contain very useful information about the universality of the structure of the Pomeron. In a study for e-A collisions at HERA, it was argued that this ratio could be measured with high systematic and statistical accuracy (195)—the situation for eRHIC should be at least comparable, if not better. Unlike  $F_2$  however,  $F_2^D$  is not truly universal—it cannot be applied, for instance, to predict diffractive cross sections in p-A scattering; it can be applied only in other lepton-nucleus scattering studies (50, 182). This has been confirmed by a study where diffractive structure functions measured at HERA were used as an input in computations for hard diffraction at Fermilab. The computations vastly overpredicted the Fermilab data on hard diffraction (196). Some of the topics discussed here will be revisited in our discussion of high parton densities.

**3.3.2. SPACE-TIME EVOLUTION OF PARTONS IN A NUCLEAR ENVIRONMENT** The nuclear structure functions are inclusive observables and are a measure of the properties of the nuclear wavefunction. Less inclusive observables, which measure these properties in greater detail, will be discussed in the section on the Color Glass Condensate. In addition to studying the wave function, we are interested in the properties of partons as they interact with the nuclear medium. These are often called final state interactions to distinguish them from the initial state interactions in the wavefunction. Separating which effects arise from the wavefunction is not easy because our interpretation of initial state and some final state interactions may depend on the gauge in which the computations are performed (197). Isolating the two effects in experiments is difficult. A case in point is the study of energy loss effects on final states in p-A collisions (198). These effects are not easy to



distinguish from shadowing effects in the wavefunction. Nevertheless, in the right kinematics this can be done.

In section 2, we discussed various final state in-medium QCD processes such as color transparency, parton energy loss and the medium modification of fragmentation functions. The EIC will enable qualitative progress in studies of the space-time picture of strong interactions relative to previous fixed target DIS experiments. The reasons for this are as follows.

- The high luminosity of the EIC will increase by many orders of magnitude the current data sample of final states in DIS scattering off nuclei at high energies.
- The EIC will provide a much broader range of  $Q^2$  and  $x$ , making it possible to compare dynamics for approximately the same space-time coherence lengths as a function of  $Q^2$ . Fixing the coherence length of partons will allow one to distinguish events wherein a photon is transformed into a strongly interacting system either outside or inside the nucleus. This will help isolate initial state interactions from those in the final state.
- The collider geometry will enable measurements of final states currently impossible in fixed target kinematics. In particular, a hermetic detector would clearly isolate coherent processes as well as quasi-elastic processes in DIS off nuclei. In addition, one can study the sizes and distributions of rapidity gaps as a function of nuclear size and energy. These will provide a sensitive probe of the interplay between space-time correlations in the final state and in the nuclear wavefunction.
- The detection of nucleons produced in the nuclear fragmentation region would make it feasible to study DIS as a function of the number of the nucleons involved in the interaction. In particular, it may be possible to study impact parameter dependence of final states, which will be important to understand in detail the nuclear amplification of final state effects. In addition, the impact parameter dependence will help distinguish geometrical effects from dynamical effects in event-by-event studies of final states.

In section 2, we discussed Generalized Parton Distributions (GPDs) in the context of DIS scattering off nucleons. These GPDs can also be measured in DIS scattering off nuclei (42). The simplest system in which to study GPDs is the deuteron. The transition from  $D \rightarrow p + n$  in the kinematics where the neutron absorbs the momentum transfer in the scattering is sensitive to the GPD in the neutron with the proton playing the role of a spectator (199). Some preliminary studies have been done for heavier nuclei (51). Certain higher twist correlations in nuclei which scale as  $A^{4/3}$  are sensitive to nucleon GPDs (134). This leads us to a discussion of GPDs in nuclei at small  $x$ . As we will discuss, high parton density effects are enhanced in large nuclei.  $k_{\perp}$  dependent GPDs might provide the right approach to study this novel regime (200). The study of nuclear GPDs at moderate and small  $x$  is a very promising, albeit nascent, direction for

further research to uncover the detailed structure of hard space-time processes in nuclear media. These nuclear distributions can be studied for the first time with the EIC.

**3.3.3. THE COLOR GLASS CONDENSATE** The Color Glass Condensate (CGC) is an effective field theory describing the properties of the dominant parton configurations in hadrons and nuclei at high energies (185). The degrees of freedom are partons, which carry color charge, hence the “Color” in CGC. The matter behaves like a glass for the following reason. The kinematics of high energy scattering dictates a natural separation between large  $x$  and small  $x$  modes (201). The large  $x$  partons at high energies behave like frozen random light cone sources over time scales that are large compared to the dynamical time scales associated with the small- $x$  partons. One can therefore describe an effective theory where the small  $x$  partons are dynamical fields and the large- $x$  partons are frozen sources (193). Under quantum evolution (202), this induces a stochastic coupling between the wee partons via their interaction with the sources. This stochastic behavior is very similar to that of a spin glass. Finally, the Condensate in CGC arises because each of these colored configurations is very similar to a Bose-Einstein Condensate. The occupation number of the gluons can be computed to be of order  $1/\alpha_s$ , and the typical momentum of the partons in the configuration is peaked about a typical momentum—the saturation momentum  $Q_s$ . These properties are further enhanced by quantum evolution in  $x$ . Because the occupation number is so large, by the correspondence principle of quantum mechanics, the small  $x$  modes can be treated as classical fields. The classical field retains its structure while the saturation scale, generated dynamically in the theory, grows with energy:  $Q_s(x') > Q_s(x)$  for  $x' < x$ . The CGC is sometimes used interchangeably with “saturation” (203)—both refer to the same phenomenon, the behavior of partons at large occupation numbers.

The Jalilian-Marian-Iancu-McLerran-Weigert-Leonidov-Kovner (JIMWLK) renormalization group equations describe the properties of partons in the high density regime (202). They form an infinite hierarchy (analogous to the Bogoliubov-Born-Green-Kirkwood-Young (BBGKY) hierarchy in statistical mechanics) of ordinary differential equations for the gluon correlators  $\langle A_1 A_2 \cdots A_n \rangle_Y$ , where  $Y = \ln(1/x)$  is the rapidity. Thus the evolution, with  $x$ , of multi-gluon (semi-inclusive) final states provides precise tests of these equations. The full hierarchy of equations are difficult to solve<sup>2</sup> though there have been major theoretical developments in that direction recently (205).

A mean field version of the JIMWLK equation, called the Balitsky-Kovchegov (BK) equation (206), describes the inclusive scattering of the quark-anti-quark dipole off the hadron in deeply inelastic scattering. In particular, the virtual photon-proton cross-section at small  $x$  can be written as (207, 208)

<sup>2</sup>For a preliminary numerical attempt, see Ref. (204).

$$\sigma_{T,L}^{\gamma^*p} = \int d^2r_{\perp} \int dz |\psi_{T,L}(r_{\perp}, z, Q^2)|^2 \sigma_{q\bar{q}N}(r_{\perp}, x), \quad 34.$$

where  $|\psi_{T,L}|^2$  is the probability for a longitudinally (L) or transversely (T) polarized virtual photon to split into a quark with momentum fraction  $z$  and an anti-quark with momentum fraction  $1 - z$  of the longitudinal momentum of the virtual photon. For the quark and anti-quark located at  $\vec{x}_{\perp}$  and  $\vec{y}_{\perp}$  respectively from the target, their transverse size is  $\vec{r}_{\perp} = \vec{x}_{\perp} - \vec{y}_{\perp}$ , and the impact parameter of the collision is  $\vec{b} = (\vec{x}_{\perp} + \vec{y}_{\perp})/2$ . The probability for this splitting is known exactly from QED and it is convoluted with the cross-section for the  $q\bar{q}$ -pair to scatter off the proton. This cross-section for a dipole scattering off a target can be expressed as

$$\sigma_{q\bar{q}N}(x, r_{\perp}) = 2 \int d^2b \mathcal{N}_Y(x, r_{\perp}, b), \quad 35.$$

where  $\mathcal{N}_Y$  is the imaginary part of the forward scattering amplitude. The BK equation (206) for this amplitude has the operator form

$$\frac{\partial \mathcal{N}_Y}{\partial Y} = \bar{\alpha}_S \mathcal{K}_{\text{BFKL}} \otimes \{ \mathcal{N}_Y - \mathcal{N}_Y^2 \}. \quad 36.$$

Here  $\mathcal{K}_{\text{BFKL}}$  is the well known Balitsky-Fadin-Kuraev-Lipatov (BFKL) kernel (184). When  $\mathcal{N} \ll 1$ , the quadratic term is negligible and one has BFKL growth of the number of dipoles; when  $\mathcal{N}$  is close to unity, the growth saturates. The approach to unity can be computed analytically (209). The BK equation is the simplest equation including both the Bremsstrahlung responsible for the rapid growth of amplitudes at small  $x$  as well as the repulsive many body effects that lead to a saturation of this growth.

Saturation models, which incorporate key features of the CGC, explain several features of the HERA data. In section 2.1, we discussed the property of geometrical scaling observed at HERA which is satisfied by the LHS of Equation 34, where it scaled as a function of the ratio of  $Q^2$  to the saturation scale  $Q_s^2$ . We also mentioned briefly a simple saturation model, the Golec-Biernat model (13), which captured essential features of this phenomenon in both inclusive and diffractive cross sections at HERA. Geometric scaling arises naturally in the Color Glass Condensate (210, 211), and it has been studied extensively both analytically (212) and numerically (213–215) for the BK equation. The success of saturation models, as discussed in section 2.1, in explaining less inclusive features of the HERA data is also encouraging since their essential features can be understood to follow from the BK equation. Below we will discuss the implications of mean field studies with the BK equation, as well as effects beyond BK.

As mentioned previously, a very important feature of saturation is the dynamical generation of a dimensionful scale  $Q_s^2 \gg \Lambda_{\text{QCD}}^2$ , which controls the running of the coupling at high energies:  $\alpha_S(Q_s^2) \ll 1$ . From the BK equation, or more generally, from solutions of BFKL in the presence of an absorptive boundary (corresponding to a CGC-like regime of high parton densities), one can deduce

that, for fixed coupling,  $Q_s^2$  has the asymptotic form  $Q_s^2 = Q_0^2 \exp(cY)$ , where  $c = 4.8\alpha_s$  and  $Y = \ln(x_0/x)$ . Here,  $Q_0^2$  and  $x_0$  are parameters from the initial conditions. Pre-asymptotic  $Y$  dependent corrections can also be computed and are large. The behavior of  $Q_s^2$  changes qualitatively when running coupling effects are taken into account. The state of the art is a computation of the saturation scale to next-to-leading order in BFKL with additional resummation of collinear terms that stabilize the predictions of NLO BFKL (216). One recovers the form  $Q_s^2 = Q_0^2 \exp(\lambda Y)$ , now with small pre-asymptotic corrections, with  $\lambda \approx 0.25$ . Remarkably, this value is very close to the value extracted in the Golec-Biernat model from fits to the HERA data.

Figure 26 shows a schematic plot of the CGC and extended scaling regions in the  $x$ - $Q^2$  plane. Clearly, with the wide kinematic range of the EIC, and the large number of available measurements—to be discussed later—one has the opportunity to make this plot quantitative. One can further add an additional axis for the atomic number to see how the kinematic reach of the CGC scales with  $A$ . In principle, one can also study the impact parameter dependence of the saturation scale in addition to the  $A$ -dependence.

### 3.3.4. SIGNATURES OF THE CGC

**Inclusive signatures.** Inclusive measurements include  $F_2$  and  $F_L$  for a wide range of nuclei, the latter measurements being done independently for the first time. The data will be precise enough to extract derivatives of these with respect to  $\ln Q^2$  and  $\ln x$  in a wide kinematic range in  $x$  and  $Q^2$ . Logarithmic derivatives of  $F_2$  and  $F_L$  will enable the extraction of the coefficient  $\lambda$  of the saturation scale, which as discussed previously, is defined to be  $Q_s^2 = Q_0^2 e^{\lambda Y}$ , where  $Y = \ln(x_0/x)$ , and where  $x_0$  and  $Q_0^2$  are reference values corresponding to the initial conditions for small- $x$  evolution. Simulations suggest that a precise extraction of this quantity may be feasible (136). Except at asymptotic energies,  $\lambda \equiv \lambda(Y)$ . Predictions exist for “universal” pre-asymptotic  $Y$ -dependent corrections to  $\lambda$  (212). Second derivatives of  $F_2$  and  $F_L$  with respect to  $\ln(x_0/x)$  will be sensitive to these corrections. The logarithmic derivatives of  $F_2$  and  $F_L$  with  $Q^2$ , especially the latter, will be sensitive to higher twist effects for  $Q^2 \approx Q_s^2(x, A)$ . The saturation scale is larger for smaller  $x$  and larger  $A$ —thus deviations of predictions of CGC fits from DGLAP fits should systematically increase as a function of both. CGC fits have been shown to fit HERA data at small  $x$  (217, 218). These fits can be extended to nuclei and compared to scaling violation data relative to DGLAP fits. The  $A$  dependence of the saturation scale can also be extracted from nuclear structure functions at small  $x$ . Again, predictions exist for the pre-asymptotic scaling of the saturation scale with rapidity (or  $x$ ), for different  $A$  (219), that can be tested against the data.

In the BK equation (mean field approximation of the CGC renormalization group equations), we now have a simple way to make predictions for the effects of high parton densities on both inclusive and diffractive (220) structure functions. There are now a few preliminary computations for e-A DIS in this framework (221,

222). Much more remains to be done—in particular, comparisons with DGLAP for EIC kinematics and detector cuts.

*Semi-inclusive and exclusive signatures.* The collider geometry of the EIC will greatly enhance the semi-inclusive final states in e-A relative to previous fixed target experiments. Inclusive hadron production at  $p_{\perp} \sim Q_s$  should be sensitive to higher twist effects for  $Q^2 \approx Q_s^2(x, A)$ . For the largest nuclei, these effects should be clearly distinguishable from DGLAP based models. Important semi-inclusive observables are coherent (or diffractive) and inclusive vector meson production, which are sensitive measures of the nuclear gluon density (110, 115). Exclusive vector meson production was suggested by Mueller, Munier and Stasto (17) as a way to extract the S-matrix (and therefore the saturation scale in the Golec-Biernat–Wüsthoff parameterization) from the  $t$ -dependence of exclusive  $\rho$ -meson production. A similar analysis of  $J/\psi$  production was performed by Guzey et al. (223). These studies for e-A collisions will provide an independent measure of the energy dependence of the saturation scale in nuclei. An extensive recent theoretical review of vector meson production of HERA (relevant for EIC studies as well) can be found in Ref. (224).

In hard diffraction, for instance, one should be able to distinguish predictions based on the strong field effects of BK (or hard Pomeron based approaches in general) from the soft Pomeron physics associated with confinement. As we discussed previously, some saturation models predict that hard diffractive events will constitute 30–40% of the cross-section (225, 226). These computations can be compared with DGLAP predictions which match soft Pomeron physics with hard perturbative physics. One anticipates that the latter would result in a much smaller fraction of the cross-section and should therefore be easily distinguishable from CGC based “strong field” diffraction.

The BK renormalization group equation is not sensitive to multi-particle correlations. These are sensitive to effects such as Pomeron loops (205), although phenomenological consequences of these remain to be explored. These effects are reflected in multiplicity fluctuations and rapidity correlations over several units in rapidity (91, 227). One anticipates quantitative studies of these will be developed in the near future. A wide detector coverage able to resolve the detailed structure of events will be optimal for extracting signatures of the novel physics of high parton densities.

**3.3.5. EXPLORING THE CGC IN PROTON/DEUTERON-NUCLEUS COLLISIONS** Although high parton density hot spots may be studied in pp collisions, they are notoriously hard to observe. The proton is a dilute object, except at small impact parameters, and one needs to tag on final states over a wide  $4\pi$  coverage. Deuteron-nucleus experiments are more promising in this regard. They have been performed at RHIC and may be performed at LHC in the future. The Cronin effect discovered in the late 70’s (121) predicts a hardening of the transverse momentum spectrum in proton-nucleus collisions, relative to proton-proton collisions at transverse momenta of

order  $p_{\perp} \sim 1 - 2$  GeV. It disappears at much larger  $p_{\perp}$ . A corresponding depletion is seen at low transverse momenta. The effect was interpreted as arising from the multiple scatterings of partons from the proton off partons from the nucleus (122).

First data from RHIC on forward D-Au scattering at  $\sqrt{s} = 200$  GeV/nucleon demonstrate how the Cronin effect is modified with energy or, equivalently, with the rapidity. The  $x$  values in nuclei probed in these experiments, at  $p_{\perp} \sim 2$  GeV, range from  $10^{-2}$  in the central rapidity region down to  $10^{-4}$  at very forward rapidities.<sup>3</sup> At central rapidities, one clearly sees a Cronin peak at  $p_{\perp} \sim 1 - 2$  GeV. A dramatic result obtained by the BRAHMS (105) experiment at RHIC<sup>4</sup> is the rapid shrinking of the Cronin peak with rapidity shown in Figure 27. In Figure 28, the centrality dependence of the effect is shown. At central rapidities, the Cronin peak is enhanced in more central collisions. For forward rapidities, the trend is reversed: more central collisions at forward rapidities show a greater suppression than less central collisions!

Parton distributions in the classical theory of the CGC exhibit the Cronin effect (229–231). However, unlike this classical Glauber picture (232), quantum evolution in the CGC shows that it breaks down completely when the  $x_2$  in the target is such that  $\ln(1/x_2) \sim 1/\alpha_S$ . This is precisely the trend observed in the RHIC D-Au experiments (105). The rapid depletion of the Cronin effect in the CGC picture is due to the onset of BFKL evolution, whereas the subsequent saturation of this trend reflects the onset of saturation effects (233). The inversion of the centrality dependence can be explained as arising from the onset of BFKL anomalous dimensions, that is, the nuclear Bremsstrahlung spectrum changes from  $Q_s^2/p_{\perp}^2 \rightarrow Q_s/p_{\perp}$ . Finally, an additional piece of evidence in support of the CGC picture is the broadening of azimuthal correlations (234) for which preliminary data now exists from the STAR collaboration (235). We note that alternative explanations have been given to explain the BRAHMS data (236). These ideas can be tested conclusively in photon and di-lepton production in D-A collisions at RHIC (237) as well as by more detailed correlation studies.

Hadronic collisions in pQCD are often interpreted within the framework of collinear factorization. At high energies,  $k_{\perp}$  factorization may be applicable (238) where the relevant quantities are “unintegrated”  $k_{\perp}$  dependent parton densities. Strict  $k_{\perp}$ -factorization which holds for gluon production in p-A collisions (197, 239) is broken for quark production (240, 241), for azimuthal correlations (242) and diffractive final states (243). For a review, see Ref. (244). These cross-sections can still be written in terms of  $k_{\perp}$ -dependent multi-parton correlation functions (240) and will also appear in DIS final states (220). DIS will allow us to test the universality of these correlations, that is, whether such correlations extracted from p-A collisions can be used to compute e-A final states (230, 245).

<sup>3</sup>It has been argued (228), however, that the forward D-A cross section in the BRAHMS kinematic regime receives sizable contributions also from rather large  $x$  values.

<sup>4</sup>The trends seen by BRAHMS are also well corroborated by the PHOBOS, PHENIX and STAR experiments at RHIC in different kinematic ranges (102–104).

3.3.6. THE COLOR GLASS CONDENSATE AND THE QUARK GLUON PLASMA The CGC provides the initial conditions for nuclear collisions at high energies. The number and energy of gluons released in a heavy ion collision of identical nuclei can be simply expressed in terms of the saturation scale as (246–248)

$$\frac{1}{\pi R^2} \frac{dE}{d\eta} = \frac{c_E}{g^2} Q_s^3, \quad \frac{1}{\pi R^2} \frac{dN}{d\eta} = \frac{c_N}{g^2} Q_s^2, \quad 37.$$

where  $c_E \approx 0.25$  and  $c_N \approx 0.3$ . Here  $\eta$  is the space-time rapidity. These simple predictions led to correct predictions for the hadron multiplicity at central rapidities in Au-Au collisions at RHIC (246, 249) and for the centrality and rapidity dependence of hadron distributions (250). However, the failure of more detailed comparisons to the RHIC jet quenching data (251) and elliptic flow data (252) suggested that final state effects are important and significantly modify predictions based on the CGC alone. The success of hydrodynamic predictions suggests that matter may have thermalized to form a quark gluon plasma (253). Indeed, bulk features of multiplicity distributions may be described by the CGC precisely as a consequence of early thermalization—leading to entropy conservation (254). Initial-state effects will be more important in heavy ion collisions at the LHC because one is probing smaller  $x$  in the wave function. Measurements of saturation scales for nuclei at the EIC will independently corroborate equations such as Equation 37 and therefore the picture of heavy ion collisions outlined above. Further, a systematic study of energy loss in cold matter will help constrain extrapolations of pQCD (131) used to study jet quenching in hot matter.

3.3.7. PROTON/DEUTERON-NUCLEUS VERSUS ELECTRON-NUCLEUS COLLISIONS AS PROBES OF HIGH PARTON DENSITIES Both p/D-A and e-A collisions probe the small  $x$  region at high energies. Both are important to ascertain truly universal aspects of novel physics. e-A collisions, owing to the independent “lever” arm in  $x$  and  $Q^2$ , as well as the simpler lepton-quark vertex, are better equipped for precision measurements. For example, in e-A collisions, information about gluon distributions can be extracted from scaling violations and from photon-gluon fusion processes. In both cases, high precision measurements are feasible. In p-A collisions, one can extract gluon distributions from scaling violations in Drell-Yan and gluon-gluon and quark-gluon fusion channels such as open charm and direct photon measurements respectively. However, for both scaling violations and fusion processes, one has more convolutions and kinematic constraints in p-A than in e-A. These limit both the precision and range of measurements. In Drell-Yan, in contrast to  $F_2$ , clear scaling violations in the data are very hard to see and data are limited to  $M^2 > 16 \text{ GeV}^2$ , above the  $J/\psi$  and  $\psi'$  thresholds.

A clear difference between p/D-A and e-A collisions is in hard diffractive final states. At HERA, these constituted approximately 10% of the total cross section. At eRHIC, these may constitute 30–40% of the cross section (225, 226). Also, factorization theorems derived for diffractive parton distributions only apply to lepton-hadron processes (182). Spectator interactions in p/D-A collisions will

destroy rapidity gaps. A comparative study of p/D-A and e-A collisions thus has great potential for unravelling universal aspects of event structures in high energy QCD.

#### 4. ELECTRON-ION COLLIDER-ACCELERATOR ISSUES

With the scientific interest in a high luminosity lepton-ion collider gathering momentum during the last several years, there has been a substantial effort in parallel to develop a preliminary technical design for such a machine. A team of physicists from BNL, MIT-Bates, DESY and the Budker Institute have developed a realistic design (255) for a machine using RHIC, which would attain an e-p collision luminosity of  $0.4 \times 10^{33} \text{ cm}^{-2} \text{ s}^{-1}$  and could with minimal R&D start construction as soon as funding becomes available. Other more ambitious lepton-ion collider concepts which would use a high intensity electron linac to attain higher luminosity are under active consideration (255, 256). This section gives an overview of the activities currently underway related to the accelerator design.

The physics program described above sets clear requirements and goals for the lepton-ion collider to be a successful and efficient tool. These goals include: a sufficiently high luminosity; a significant range of beam collision energies; and polarized beam (both lepton and nucleon) capability. On the other hand, to be realistic, the goals should be based on the present understanding of the existing RHIC machine and limitations which arise from the machine itself. Realistic machine upgrades should be considered to overcome existing limitations and to achieve advanced machine parameters, but those upgrades should be cost-effective.

The intent to minimize required upgrades in the existing RHIC rings affects the choice of parameters and the set of goals. For example, the design assumed simultaneous collisions of both ion-ion and lepton-ion beams. In the main design line, collisions in two ion-ion interaction regions, at the “6” and “8 o’clock” locations, have to be allowed in parallel with electron-ion collisions.

Taking these considerations into account, the following goals were defined for the accelerator design:

- The machine should be able to provide beams in the following energy ranges: for the electron accelerator, 5–10 GeV polarized electrons, 10 GeV polarized positrons; for the ion accelerator, 50–250 GeV polarized protons, 100 GeV/u Gold ions.
- Luminosity: in the  $10^{32} - 10^{33} \text{ cm}^{-2} \text{ s}^{-1}$  range for e-p collisions; in the  $10^{30} - 10^{31} \text{ cm}^{-2} \text{ s}^{-1}$  range for e-Au collisions.
- 70% polarization for both lepton and proton beams.
- Longitudinal polarization in the collision point for both lepton and proton beams.

An additional design goal was to include the possibility of accelerating polarized ions, especially polarized  $^3\text{He}$  ions.



## 4.1. eRHIC: Ring-Ring Design

The primary eRHIC design centers on a 10 GeV lepton storage ring which intersects with one of the RHIC ion beams at one of the interaction regions (IRs), not used by any of the ion-ion collision experiments. RHIC uses superconducting dipole and quadrupole magnets to maintain ion beams circulating in two rings on a 3834 meter circumference. The ion energy range covers 10.8 to 100 GeV/u for gold ions and 25 to 250 GeV for protons. There are in total 6 intersection points where two ion rings, Blue and Yellow, cross each other. Four of these intersections points are currently in use by physics experiments.

A general layout of the ring-ring eRHIC collider is shown in Figure 29 with the lepton-ion collisions occurring in the “12 o’clock” interaction region. Plans have been made for a new detector, developed and optimized for electron-ion collision studies, to be constructed in that interaction region.

The electron beam in this design is produced by a polarized electron source and accelerated in a linac injector to energies of 5 to 10 GeV. To reduce the injector size and cost, the injector design includes recirculation arcs, so that the electron beam passes through the same accelerating linac sections multiple times. Two possible linac designs, superconducting and normal conducting, have been considered. The beam is accelerated by the linac to the required collision energy and injected into the storage ring. The electron storage ring is designed to be capable of electron beam storage in the energy range of 5 to 10 GeV with appropriate beam emittance values. It does not provide any additional acceleration for the beam. The electron ring should minimize depolarization effects in order to keep the electron beam polarization lifetime longer than the typical storage time of several hours.

The injector system also includes the conversion system for positron production. After production the positrons are accelerated to 10 GeV energy and injected into the storage ring similarly to the electrons. Obviously the field polarities of all ring magnets should be reversed in the positron operation mode. Unlike electrons, the positrons are produced unpolarized and have to be polarized using radiative self-polarization in the ring. Therefore, the design of the ring should allow for a sufficiently small self-polarization time. The current ring design provides a self-polarization time of about 20 min at 10 GeV. But with polarization time increasing sharply as beam energy goes down the use of a polarized positron beam in the present design is limited to 10 GeV energy.

The design of the eRHIC interaction region involves both accelerator and detector considerations. Figure 29 shows the electron accelerator located at the “12 o’clock” region. Another possible location for the electron accelerator and for electron-ion collisions might be the “4 o’clock” region. For collisions with electrons the ion beam in the RHIC Blue ring will be used, because the Blue ring can operate alone, even with the other ion ring, Yellow, being down. The interaction region design provides for fast beam separation for electron and Blue ring ion bunches as well as for strong focusing at the collision point. In this design, the other (Yellow) ion ring makes a 3 m vertical excursion around the collision

region, avoiding collisions both with electrons and the Blue ion beam. The eRHIC interaction region includes spin rotators, in both the electron and the Blue ion rings, to produce longitudinally polarized beams of leptons and protons at the collision point.

The electron cooling system in RHIC (257, 258) is one of the essential upgrades required for eRHIC. The cooling is necessary to reach the luminosity goals for lepton collisions with Gold ions and low (below 150 GeV) energy protons. Electron cooling is considered an essential upgrade of RHIC to attain higher luminosity in ion-ion collisions.

In addition, the present eRHIC design assumes a total ion beam current higher than that being used at present in RHIC operation. This is attained by operating RHIC with 360 bunches.

The eRHIC collision luminosity is limited mainly by the maximum achievable beam-beam parameters and by the interaction region magnet aperture limitations. To understand this, it is most convenient to use a luminosity expression in terms of beam-beam parameters ( $\xi_e \xi_i$ ) and rms angular spread in the interaction point ( $\sigma'_{xi}, \sigma'_{ye}$ ):

$$L = f_c \frac{\pi \gamma_i \gamma_e}{r_i r_e} \xi_{xi} \xi_{ye} \sigma'_{xi} \sigma'_{ye} \frac{(1 + K)^2}{K}.$$

The  $f_c = 28.15$  MHz is a collision frequency, assuming 360 bunches in the ion ring and 120 bunches in the electron ring. The parameter  $K = \sigma_y / \sigma_x$  presents the ratio of beam sizes in the interaction point. One of the basic conditions which defines the choice of beam parameters is a requirement on equal beam sizes of ion and electron beams at the interaction point:  $\sigma_{xe} = \sigma_{xi}$  and  $\sigma_{ye} = \sigma_{ye}$ . The requirement is based on the operational experience at the HERA collider and on the reasonable intention to minimize the amount of one beam passing through the strongly nonlinear field in the outside area of the counter-rotating beam.

According to the above expression, the luminosity reaches a limiting value at the maximum values of beam-beam parameters, or at the beam-beam parameter limits. For protons (and ions) the total beam-beam parameter limit was assumed to be 0.02, following the experience and observation from other proton machines as well as initial experience from RHIC operation. With three beam-beam interaction points, two for proton-proton and one for electron-proton collisions, the beam-beam parameter per interaction point should not exceed 0.007.

For the electron (or positron) beam a limiting value of the beam-beam parameter has been put at 0.08 for 10 GeV beam energy, following the results of beam-beam simulations, as well as from the experience at electron machines of similar energy range. Because the beam-beam limit decreases proportionally with the beam energy, the limiting value for 5 GeV is reduced to 0.04.

The available magnet apertures in the interaction region also put a limit on the achievable luminosity. The work on the interaction region design revealed considerable difficulties to provide an acceptable design for collisions of round beams. The IR has been designed to provide low beta focusing and efficient separation of elliptical beams, with beam size ratio  $K = 1/2$ . The main aperture

**TABLE 1** Luminosities and main beam parameters for  $e^\pm$ -p collisions

High energy tune	p	e	p	e
Energy, GeV	250	10	50	5
Bunch intensity, $10^{11}$	1	1	1	1
Ion normalized emittance, $\pi$ mm · mrad, $x/y$	15/15		5/5	
rms emittance, nm, $x/y$	9.5/9.5	53/9.5	16.1/16.1	85/38
$\beta^*$ , cm, $x/y$	108/27	19/27	186/46	35/20
Beam-beam parameters, $x/y$	0.0065/0.003	0.03/0.08	0.019/0.0095	0.036/0.04
$\kappa = \xi_y/\xi_x$	1	0.18	1	0.45
Luminosity, $1.0 \times 10^{32}$ cm <sup>-2</sup> s <sup>-1</sup>		4.4		1.5

limitation comes from the septum magnet, which leads to the limiting values of  $\sigma'_{xp} = 93 \mu\text{rad}$ .

Another limitation which must be taken into account is a minimum acceptable value of the beta-function at the interaction point ( $\beta^*$ ). With the proton rms bunch length of 20 cm, decreasing  $\beta^*$  well below this number results in a luminosity degradation due to the hour-glass effect. The limiting value  $\beta^* = 19$  cm has been used for the design, which results in a luminosity reduction of only about 12%. A bunch length of 20 cm for Au ions would be achieved with electron cooling.

Tables 1 and 2 show design luminosities and beam parameters. The positron beam intensity is assumed to be identical to the electron beam intensity, hence the luminosities for collisions involving a positron beam are equivalent to electron-ion collision luminosities. To achieve the high luminosity in the low energy tune in Table 1, the electron cooling has to be used to reduce the normalized transverse emittance of the lower energy proton beam to 5  $\pi$  mm · mrad. Also, in that case the

**TABLE 2** Luminosities and main beam parameters for  $e^\pm$ -Au collisions

High energy tune	Au	e	Au	e
Energy, GeV	100	10	100	5
Bunch intensity, $10^{11}$	0.01	1	0.0045	1
Ion normalized emittance, $\pi$ mm · mrad, $x/y$	6/6		6/6	
rms emittance, nm, $x/y$	9.5/9.5	54/7.5	9.5/9.5	54/13.5
$\beta^*$ , cm, $x/y$	108/27	19/34	108/27	19/19
Beam-beam parameters, $x/y$	0.0065/0.003	0.0224/0.08	0.0065/0.003	0.02/0.04
$\kappa = \xi_y/\xi_x$	1	0.14	1	0.25
Luminosity, $1.0 \times 10^{32}$ cm <sup>-2</sup> s <sup>-1</sup>		4.4		2.0

proton beam should have collisions only with the electron beam. Proton-proton collisions in the other two interaction points have to be avoided to allow for a higher proton beam-beam parameter. The maximum luminosity achieved in the present design is  $4.4 \times 10^{32} \text{ cm}^{-2} \text{ s}^{-1}$  in the high energy collision mode (10 GeV leptons on 250 GeV protons). Possible paths to luminosities as high as  $10^{33} \text{ cm}^{-2} \text{ s}^{-1}$  are being explored, with studies planned to investigate the feasibility of higher electron beam intensity operation. To achieve and maintain the Au normalized transverse beam emittances shown in Table 2, electron cooling of the Au beam will be used. For the lower energy tune of electron-Gold collisions, the intensity of the Gold beam is considerably reduced because of the reduced value of the beam-beam parameter limit for the electron beam.

## 4.2. eRHIC: Linac-Ring Design

A linac-ring design for eRHIC is also under active consideration. This configuration uses a fresh electron beam bunch for each collision and so the tune shift limit on the electron beam is removed. This provides the important possibility to attain significantly higher luminosity (up to  $10^{34} \text{ cm}^{-2} \text{ s}^{-1}$ ) than the ring-ring design. A second advantage of the linac-ring design is the ability to reverse the electron spin polarization on each bunch. A disadvantage of the linac-ring design is the inability to deliver polarized positrons. The realization of the linac beam is technically challenging and the polarized electron source requirements are well beyond present capabilities (259).

Figure 30 shows a schematic layout of a possible linac-ring eRHIC design. A 450 mA polarized electron beam is accelerated in an Energy Recovery Linac (ERL). After colliding with the RHIC beam in as many as four interaction points, the electron beam is decelerated to an energy of a few MeV and dumped. The energy thus recovered is used for accelerating subsequent bunches to the energy of the experiment.

## 4.3. Other Lepton-Ion Collider Designs: ELIC

A very ambitious electron-ion collider design seeking to attain luminosities up to  $10^{35} \text{ cm}^{-2} \text{ s}^{-1}$  is underway at Jefferson Laboratory (156). This Electron Light Ion Collider (ELIC) design (see Figure 31) is based on use of polarized 5 to 7 GeV electrons in a superconducting ERL upgrade of the present CEBAF accelerator and a 30 to 150 GeV ion storage ring (polarized p, d,  $^3\text{He}$ , Li and unpolarized nuclei up to Ar, all totally stripped). The ultra-high luminosity is envisioned to be achievable with short ion bunches and crab-crossing at 1.5 GHz bunch collision rate in up to four interaction regions. The ELIC design also includes a recirculating electron ring that would help to reduce the linac and polarized source requirements compared to the linac-ring eRHIC design of section 4.2.

The ELIC proposal is at an early stage of development. A number of technical challenges must be resolved, and several R&D projects have been started. These include development of a high average current polarized electron source with a high

bunch charge, electron cooling of protons/ions, energy recovery at high current and high energy, and the design of an interaction region that supports the combination of high luminosity and high detector acceptance and resolution.

## 5. DETECTOR IDEAS FOR THE EIC

The experience gained at HERA with the H1 and ZEUS detectors (260) provides useful guidance for the conceptual design of a detector that will measure a complete event ( $4\pi$ -coverage) produced in collisions of energetic electrons with protons and ions, at different beam energies and polarizations. The H1 and ZEUS detectors are general-purpose magnetic detectors with nearly hermetic calorimetric coverage. The differences between them are based on their approach to calorimetry. The H1 detector collaboration emphasized the electron identification and energy resolution, whereas the ZEUS collaboration puts more emphasis on optimizing hadronic calorimetry. The differences in their physics philosophy were reflected in their overall design: H1 had a liquid Argon calorimeter inside the large diameter magnet, whereas ZEUS chose to build a Uranium scintillator sampling calorimeter with equal response to electrons and hadrons. They put their tracking detectors inside a superconducting solenoid surrounded by calorimeters and muon chambers. H1 placed their tracking chambers inside the calorimeter surrounded by their magnet. In addition, both collaborations placed their luminosity and electron detectors downstream in the direction of the proton and electron directions, respectively. Both collaborations added low angle forward proton spectrometers and neutron detectors in the proton beam direction.

Both detectors have good angular coverage (approximately,  $3^\circ < \theta < 175^\circ$ , where the angle is measured with respect to the incoming proton beam direction) for electromagnetic (EM) calorimetry, with energy resolutions of 1–3% and for electromagnetic showers  $\sigma/E \sim 15\%/\sqrt{E(\text{GeV})} + 1\%$ . Hadronic energy scale uncertainties of 3% were achieved for both, with some differences in the  $\sigma/E$  for hadronic showers, which were  $\sim R/\sqrt{E(\text{GeV})} + 2\%$ , where  $R = 35\%$  and  $50\%$  for ZEUS and H1, respectively. With the central tracking fields  $\approx 1.5$  T covering a region similar to the calorimetric angular acceptance, momentum resolution  $\sigma/p_T < 0.01 p_T(\text{GeV})$  was generally achieved for almost all acceptances, except for the forward and backward directions. These directions were regarded at the beginning as being less interesting. However, the unexpected physics of low  $x$  and low  $Q^2$  (including diffraction in e-p scattering) came from this rather poorly instrumented region. And since the luminosity upgrade program, the low  $\beta^*$  magnets installed close to the interaction point to enhance the luminosity of e-p collisions (HERA-II) have further deteriorated the acceptance of detectors in these specific geometric regions.

The EIC detector design ideas are already being guided by the lessons learned from the triumphs and tribulations of the HERA experience. All advantages of the HERA detectors such as the almost  $4\pi$  coverage and the functionality with respect

to spatial orientation will be preserved. The EIC detector will have enhanced capability in the very forward and backward directions to measure continuously the low  $x$  and low  $Q^2$  regions that are not comprehensively accessible at HERA. The detector design directly impacts the interaction region design and hence the accelerator parameters for the two beam elements: the effective interaction luminosity and the effective polarization of the two beams at the interaction point. Close interaction between the detector design and the IR design is hence needed in the very early stage of the project, which has already started (255). It is expected that the detector design and the IR design will evolve over the next few years. The e-p and e-A collisions at EIC will produce very asymmetric event topologies, not unlike HERA events. These asymmetries, properly exploited, allow precise measurements of energy and color flow in collisions of large and small- $x$  partons. They also allow observation of interactions of electrons with photons that are coherently emitted by the relativistic heavy ions. The detector for EIC must detect: the scattered electrons, the quark fragmentation products and the centrally produced hadrons. It will be the first collider detector to measure the fragmentation region of the proton or the nucleus, a domain not covered effectively at HERA. The detector design, in addition, should pose no difficulties for important measurements such as precision beam polarization (electron as well as hadron beam) and collision luminosity.

The EIC detector design will allow measurements of partons from hard processes in the region around  $90^\circ$  scattering angle with respect to the beam pipes. This central region could have a jet tracker with an EM calorimeter backed by an instrumented iron yoke. Electrons from DIS are also emitted into this region and will utilize the tracking and the EM calorimetry. Electrons from photo-production and from DIS at intermediate and low momentum transfer will have to be detected by specialized backward detectors. With these guiding ideas, one could imagine that the EIC barrel might have a time projection chamber (TPC) backed by an EM Calorimeter inside a superconducting coil. One could use Spaghetti Calorimetry (SPACAL) for endcaps and GEM-type micro-vertex detector to complement the tracking capacity of the TPC in the central as well as forward/backward (endcap) regions. This type of central and end-cap detector geometry is now fairly standard. Details of the design could be finalized in the next few years using the state of the art technology and experience from more recent detectors such as BaBar at SLAC (USA) and Belle at KEK (Japan). To accommodate tracking and particle ID requirements for the different center-of-mass energy running ( $\sqrt{s} = 30\text{--}100$  GeV) resulting at different beam energies, the central spectrometer magnet will have multiple field strength operation capabilities, including radial dependence of field strengths. Possible spectrometry based on dipole and toroidal fields is also being considered at this time.

The forward and backward regions (hadron and electron beam directions) in e-p collisions were instrumented at HERA up to a pseudo-rapidity of  $\eta \approx 3$ . A specialized detector added later extended this range with difficulty to  $\eta \approx 4$ . Although acceptance enhancement in the regions beyond  $\eta = 4$  is possible with conventional ideas such as forward calorimetry and tracking using beam elements

and silicon strip based Roman Pot Detectors (181), it is imperative for the EIC that this region be well instrumented. A recent detector design for eRHIC developed by the experimental group at the Max-Planck Institute, Munich, accomplishes just this (136) by allowing continuous access to physics up to  $\eta \approx 6$ . The main difference with respect to a conventional collider detector is a dipole field, rather than a solenoid, that separates the low energy scattered electron from the beam. High precision silicon tracking stations capable of achieving  $\Delta p/p \sim 2\%$ , EM calorimetry with energy resolution better than  $20\%/\sqrt{E}$ , an excellent  $e/\pi$  separation over a large  $Q^2$  range, all in the backward region (in the electron beam direction) are attainable. In the forward region, the dipole field allows excellent tracking and a combination of EM and hadronic calorimetry with  $20\%/\sqrt{E(\text{GeV})}$  and  $50\%/\sqrt{E(\text{GeV})}$  energy resolution, respectively. This allows access to very high  $x \sim 0.9$  with excellent accuracy. This region of high  $x$  is largely unexplored both in polarized and in unpolarized DIS. A significant distance away from the EIC central detector and IR, there may be Roman Pots, high rigidity spectrometers including EM calorimetry and forward electron taggers, all placed to improve the measurement of low angle scattering at high energy.

Although significant effort will be made to avoid design conflicts, the conventional detector using a solenoid magnet and the one described above may not coexist in certain scenarios being considered for the accelerator designs of the EIC at BNL. The main design line, presently the ring-ring design, may be particularly difficult with only one IR. Options such as time sharing between two detectors at the same IR with the two detectors residing on parallel rails may be considered. In the case of the linac-ring scenario, several other options are available. Because the physics of low  $x$  and low  $Q^2$  does not require a large luminosity, nor is presently the beam polarization a crucial requirement for the physics (136), an interaction point with sufficient beam luminosity would be possible with innovative layouts of the accelerator complex. These and other details will be worked out in the next several years. Depending on the interest shown by the experimental community, accelerator designs that incorporate up to four collision points (while still allowing two hadron-hadron collision points at RHIC) will be considered and developed.

## ACKNOWLEDGMENTS

This review draws generously on the whitepaper for the Electron Ion Collider (BNL-68933-02/07-REV), and we thank all our co-authors on this publication for their efforts. We are especially grateful to Marco Stratmann and Mark Strikman for valuable advice, discussions and comments. W.V. and A.D. are grateful to RIKEN and Brookhaven National Laboratory. R.M. is supported by the Department of Energy Cooperative Agreement DE-FC02-94ER40818. W.V. and R.V. were supported by Department of Energy (contract number DE-AC02-98CH10886). R.V.'s research was also supported in part by a research award from the A. Von Humboldt Foundation.

The Annual Review of Nuclear and Particle Science is online at  
<http://nucl.annualreviews.org>

## LITERATURE CITED

1. Dokshitzer YL. *Sov. Phys. JETP* 46:641 (1977); Lipatov LN. *Sov. J. Nucl. Phys.* 20:95 (1975); Gribov VN, Lipatov LN. *Sov. J. Nucl. Phys.* 15:438 (1972)
2. Altarelli G, Parisi G. *Nucl. Phys.* B126:298 (1977)
3. Moch S, Vermaseren JAM, Vogt A. *Nucl. Phys.* B688:101 (2004); *Nucl. Phys.* B691:129 (2004)
4. Whitlow LM, et al. *Phys. Lett.* B282:475 (1992); Whitlow LM. SLAC-preprint, SLAC-357 (1990)
5. Arneodo M, et al. (New Muon Collab.) *Nucl. Phys.* B483:3 (1997); Adams MR, et al. (E665 Collab.) *Phys. Rev. D* 54:3006 (1996)
6. Aid S, et al. (H1 Collab.) *Nucl. Phys.* B470:3 (1996); Adloff C, et al. (H1 collab.) *Nucl. Phys.* 497:3 (1997)
7. Derrick M, et al. (ZEUS collab.) *Z. Phys. C* 69:607 (1996); Derrick M, et al. (ZEUS collab.) *Z. Phys. C* 72:399 (1996)
8. Rizvi E. Presented at the Int. Europhys. Conf. High Energy Phys., Aachen, Germany, July (2003)
9. Breitweg J, et al. (ZEUS collab.) *Eur. Phys. J. C* 7:609 (1999); Chekanov S, et al. (ZEUS collab.) *Phys. Rev. D* 67:012007 (2003)
10. Martin AD, Roberts RG, Stirling WJ, Thorne RS. *Eur. Phys. J. C* 35:325 (2004); Huston J, Pumplun J, Stump D, Tung WK. arXiv:hep-ph/0502080
11. Bartels J, Golec-Biernat K, Peters K. *Eur. Phys. J. C* 17:121 (2000)
12. Stasto AM, Golec-Biernat K, Kwiecinski J. *Phys. Rev. Lett.* 86:596 (2001)
13. Golec-Biernat K, Wüsthoff M. *Phys. Rev. D* 59:014017 (1999)
14. Golec-Biernat K, Wüsthoff M. *Phys. Rev. D* 60:114023 (1999)
15. Bartels J, Golec-Biernat K, Kowalski H. *Phys. Rev. D* 66:014001 (2002)
16. Kowalski H, Teaney D. *Phys. Rev. D* 68:114005 (2003)
17. Munier S, Stasto AM, Mueller AH. *Nucl. Phys.* B603:427 (2001)
18. Goncalves VP, Machado MVT. *Phys. Rev. Lett.* 91:202002 (2003)
19. Hughes EW, Voss R. *Annu. Rev. Nucl. Part. Sci.* 49:303 (1999); Filippone BW, Ji XD. *Adv. Nucl. Phys.* 26:1 (2001); Bass SD. arXiv:hep-ph/0411005
20. Anselmino M, Gambino P, Kalinowski J. *Z. Phys. C* 64:267 (1994); *Phys. Rev. D* 55:5841 (1997)
21. De Nardo L. (HERMES collab.) *Czech. J. Phys.* 52:A1 (2002)
22. Tobias WA. (E155 collab.) *Measurement of the proton and deuteron spin structure functions  $g_1$  and  $g_2$* . PhD thesis. Univ. Virginia, SLAC-R617 (January 2001)
23. Ahmed MA, Ross GG. *Nucl. Phys.* B111:441 (1976)
24. Mertig R, van Neerven W. *Z. Phys. C* 70:637 (1996); Vogelsang W. *Phys. Rev. D* 54:2023 (1996); *Nucl. Phys.* B475:47 (1996)
25. Blümlein J, Böttcher H. *Nucl. Phys.* B636:225 (2002)
26. Glück M, Reya E, Stratmann M, Vogelsang W. *Phys. Rev. D* 63:094005 (2001)
27. Asymmetry Analysis Collab., Hirai M, Kumano S, Saito N. *Phys. Rev. D* 69:054021 (2004)
28. Bjorken JD. *Phys. Rev.* 148:1467 (1966); *Phys. Rev. D* 1:1376 (1970)
29. Ellis J, Jaffe RL. *Phys. Rev. D* 9:1444 (1974); *Phys. Rev. D* 10:1669 (1974)
30. Kodaira J, et al. *Nucl. Phys.* B159:99 (1979); Gorishnii SG, Larin SA. *Phys. Lett.* B172:109 (1986); *Nucl. Phys.*



- B283:452 (1987); Larin SA, Vermaseren JAM. *Phys. Lett.* B259:345 (1991)
31. Ellis J, Karliner M. *Phys. Lett.* B341:397 (1995); Altarelli G, Ball RD, Forte S, Ridolfi G. *Nucl. Phys.* B496:337 (1997)
  32. Ratcliffe P. arXiv:hep-ph/0402063
  33. Diakonov D, Petrov V, Pobylitsa P, Polyakov MV, Weiss C. *Nucl. Phys.* B480:341 (1996); *Phys. Rev. D* 56:4069 (1997); Wakamatsu M, Kubota T. *Phys. Rev. D* 60:034020 (1999); Dressler B, Goeke K, Polyakov MV, Weiss C. *Eur. Phys. J. C* 14:147 (2000); Dressler B, et al. *Eur. Phys. J. C* 18:719 (2001); Kumano S. *Phys. Rept.* 303:183 (1998); *Phys. Lett.* B479:149 (2000); Glück M, Reya E. *Mod. Phys. Lett.* A15:883 (2000); Cao FG, Signal AI. *Eur. Phys. J. C* 21:105 (2001); Bhalerao RS. *Phys. Rev. C* 63:025208 (2001); Fries RJ, Schäfer A, Weiss C. *Eur. Phys. J. A* 17:509 (2003)
  34. Adeva B, et al. (Spin Muon collab.) *Phys. Lett.* B420:180 (1998)
  35. Airapetian A, et al. (HERMES collab.) *Phys. Rev. Lett.* 92:012005 (2004); *Phys. Rev. D* 71:012003 (2005)
  36. Stratmann M, Vogelsang W. *Phys. Rev. D* 64:114007 (2001); Glück M, Reya E. arXiv:hep-ph/0203063; Kotzinian A. *Phys. Lett.* B552:172 (2003); arXiv:hep-ph/0410093; Navarro G, Sassot R. *Eur. Phys. J. C* 28:321 (2003); Christova E, Kretzer S, Leader E. *Eur. Phys. J. C* 22:269 (2001); Leader E, Stamenov DB. *Phys. Rev. D* 67:037503 (2003); Bass SD. *Phys. Rev. D* 67:097502 (2003); de Florian D, Navarro GA, Sassot R. *Phys. Rev. D* 71:094018 (2005)
  37. Bunce G, Saito N, Soffer J, Vogelsang W. *Annu. Rev. Nucl. Part. Sci.* 50:525 (2000)
  38. Ji XD. *Phys. Rev. Lett.* 78:610 (1997)
  39. Jaffe RL, Manohar A. *Nucl. Phys.* B337:509 (1990); Bashinsky SV, Jaffe RL. *Nucl. Phys.* B536:303 (1998)
  40. Bravar A, von Harrach D, Kotzinian AM. *Phys. Lett.* B421:349 (1998); Airapetian A, et al. (HERMES collab.) *Phys. Rev. Lett.* 84:4047 (2000); Hedicke S. (COMPASS collab.) *Prog. Part. Nucl. Phys.* 50:499 (2003); Mielech A. (COMPASS collab.) *Nucl. Phys.* A752:191 (2005); Adeva B, et al. (Spin Muon Collab.) *Phys. Rev. D* 70:012002 (2004); Anthony PL, et al. (E155 collab.) *Phys. Lett.* B458:536 (1999); Afanasev A, Carlson CE, Wahlquist C. *Phys. Lett.* B398:393 (1997); *Phys. Rev. D* 58:054007 (1998); *Phys. Rev. D* 61:034014 (2000); Jäger B, Stratmann M, Vogelsang W. arXiv:hep-ph/0505157
  41. Dittes FM, et al. *Phys. Lett.* B209:325 (1988); Radyushkin AV. *Phys. Rev. D* 56:5524 (1997)
  42. Vanderhaeghen M. *Eur. Phys. J. A* 8:455 (2000); Goeke K, Polyakov MV, Vanderhaeghen M. *Prog. Part. Nucl. Phys.* 47:401 (2001); Belitsky AV, Müller D, Kirchner A. *Nucl. Phys.* B629:323 (2002); Diehl M. *Phys. Rept.* 388:41 (2003); Ji XD. *Annu. Rev. Nucl. Part. Sci.* 54:413 (2004)
  43. Burkardt M. *Phys. Rev. D* 62:071503 (2000); *Phys. Rev. D* 66:114005 (2002); *Int. J. Mod. Phys.* A18:173 (2003); Burkardt M. *Nucl. Phys.* A735:185 (2004); arXiv:hep-ph/0505189; Burkardt M, Hwang DS. arXiv:hep-ph/0309072; Ralston JP, Pire B. *Phys. Rev. D* 66:111501 (2002); Diehl M. *Eur. Phys. J. C* 25:223 (2002); Diehl M. *Eur. Phys. J. C* 31:277 (2003); Belitsky AV, Müller D. *Nucl. Phys.* A711:118 (2002); Ji XD. *Phys. Rev. Lett.* 91:062001 (2003); Belitsky AV, Ji XD, Yuan F. *Phys. Rev. D* 69:074014 (2004); Diehl M, Hägler P. arXiv:hep-ph/0504175
  44. Collins JC, Freund A. *Phys. Rev. D* 59:074009 (1999); Ji XD, Osborne J. *Phys. Rev. D* 58:094018 (1998); Radyushkin AV. *Phys. Lett.* B380:417 (1996); *Phys. Rev. D* 56:5524 (1997)
  45. Belitsky AV, Müller D, Niedermeier L, Schäfer A. *Phys. Lett.* B474:163 (2000); Belitsky AV, Freund A, Müller D. *Phys. Lett.* B493:341 (2000); Freund A, McDermott MF. *Phys. Rev. D* 65:091901 (2002);

- Phys. Rev. D* 65:074008 (2002); *Eur. Phys. J. C* 23:651 (2002)
46. Adloff C, et al. (H1 collab.) *Phys. Lett. B* 517:47 (2001); Aktas A, et al. (H1 collab.) arXiv:hep-ex/0505061; Chekanov S, et al. (ZEUS collab.) *Phys. Lett. B* 573:46 (2003)
47. Airapetian A, et al. (HERMES collab.) *Phys. Rev. Lett.* 87:182001 (2001)
48. Ellinghaus F, et al. (HERMES collab.) *Nucl. Phys. A* 711:171 (2002)
49. Stepanyan S, et al. (CLAS collab.) *Phys. Rev. Lett.* 87:182002 (2001)
50. Collins JC, Frankfurt L, Strikman M. *Phys. Rev. D* 56:2982 (1997); Belitsky AV, Müller D. *Phys. Lett. B* 513:349 (2001)
51. Cano F, Pire B. *Eur. Phys. J. A* 19:423 (2004); Strikman M, Guzey V. *Phys. Rev. C* 68:015204 (2003); Kirchner A, Müller D. *Eur. Phys. J. C* 32:347 (2003); Freund A, Strikman M. *Phys. Rev. C* 69:015203 (2004); Polyakov MV. *Phys. Lett. B* 555:57 (2003)
52. Ralston JP, Soper DE. *Nucl. Phys. B* 152:109 (1979); Artru X, Mekhfi M. *Z. Phys. C* 45:669 (1990); Jaffe RL, Ji X. *Phys. Rev. Lett.* 67:552 (1991); *Nucl. Phys. B* 375:527 (1992)
53. Collins JC. *Nucl. Phys. B* 394:169 (1993)
54. Collins JC. *Nucl. Phys. B* 396:161 (1993)
55. Ji XD, Ma JP, Yuan F. *Phys. Rev. D* 71:034005 (2005); *Phys. Lett. B* 597:299 (2004); *Phys. Rev. D* 70:074021 (2004)
56. Mulders PJ, Tangerman RD. *Nucl. Phys. B* 461:197 (1996); Mulders PJ, Tangerman RD. *Nucl. Phys. B* 484:538 (1997); Boer D, Mulders PJ. *Phys. Rev. D* 57:5780 (1998); Efremov AV, Goeke K, Schweitzer P. *Eur. Phys. J. C* 32:337 (2003)
57. Sivers DW. *Phys. Rev. D* 41:83 (1990); *Phys. Rev. D* 43:261 (1991)
58. Brodsky SJ, Hwang DS, Schmidt I. *Phys. Lett. B* 530:99 (2002)
59. Collins JC. *Phys. Lett. B* 536:43 (2002); Belitsky AV, Ji XD, Yuan F. *Nucl. Phys. B* 656:165 (2003); Boer D, Mulders PJ, Pijlman F. *Nucl. Phys. B* 667:201 (2003); Bomhof C, Mulders PJ, Pijlman F. *Phys. Lett. B* 596:277 (2004); Bacchetta A, Bomhof C, Mulders PJ, Pijlman F. arXiv:hep-ph/0505268
60. Ji XD, Ma JP, Yuan F. *Nucl. Phys. B* 652:383 (2003)
61. Bacchetta A, Kundu R, Metz A, Mulders PJ. *Phys. Lett. B* 506:155 (2001); *Phys. Rev. D* 65:094021 (2002); Bacchetta A, Metz A, Yang JJ. *Phys. Lett. B* 574:225 (2003); Gamberg LP, Goldstein GR, Oganessyan KA. *Phys. Rev. D* 67:071504 (2003); Gamberg LP, Goldstein GR, Oganessyan KA. *Phys. Rev. D* 68:051501 (2003); arXiv:hep-ph/0309137; Yuan F. *Phys. Lett. B* 575:45 (2003); Bacchetta A, Schweitzer P. *Nucl. Phys. A* 732:106 (2004); Efremov AV, Goeke K, Schweitzer P. *Phys. Lett. B* 568:63 (2003); *Eur. Phys. J. C* 32:337 (2003); Amrath D, Bacchetta A, Metz A. arXiv:hep-ph/0504124
62. Airapetian A, et al. (HERMES collab.) *Phys. Rev. Lett.* 94:012002 (2005); Diefenthaler M. (HERMES collab.) Talk presented at the 13th International Workshop on Deep Inelastic Scattering (DIS 2005), Madison, Wisconsin, April (2005)
63. Alexakhin VY, et al. (COMPASS collab.) arXiv:hep-ex/0503002
64. Seidl R. (Belle collab.) Talk presented at the 13th International Workshop on Deep Inelastic Scattering (DIS 2005), Madison, Wisconsin, April (2005); Collins JC, Metz A. *Phys. Rev. Lett.* 93:252001 (2004); Metz A. *Phys. Part. Nucl.* 35:S85 (2004)
65. D'Alesio U, Murgia F. *Phys. Rev. D* 70:074009 (2004); arXiv:hep-ph/0412317; Anselmino M, Boglione M, D'Alesio U, Leader E, Murgia F. *Phys. Rev. D* 71:014002 (2005); Qiu JW, Serman G. *Phys. Rev. D* 59:014004 (1999)
66. Adams DL, et al. (FNAL E704 collab.) *Phys. Lett. B* 261:201 (1991); Krueger K, et al. *Phys. Lett. B* 459:412 (1999); Adams J, et al. (STAR collab.) *Phys. Rev. Lett.*

- 92:171801 (2004); Rakness G. (STAR collab.) arXiv:nucl-ex/0501026
67. Boer D, Vogelsang W. *Phys. Rev. D* 69:094025 (2004); Efremov AV, Goeke K, Menzel S, Metz A, Schweitzer P. *Phys. Lett. B* 612:233 (2005)
68. Aubert JJ, et al. (EMC collab.) *Phys. Lett. B* 123:275 (1983)
69. Arnold RG, et al. *Phys. Rev. Lett.* 52:727 (1984)
70. Arneodo M, et al. (New Muon collab.) *Nucl. Phys. B* 441:3, 12 (1995)
71. Adams MR, et al. (E665 collab.) *Z. Phys. C* 67:403 (1995)
72. Arneodo M. *Phys. Rept.* 240:301 (1994)
73. Geesaman DF, Saito K, Thomas AW. *Annu. Rev. Nucl. Part. Sci.* 45:337 (1995)
74. Friman BL, Pandharipande VR, Wiringa RB. *Phys. Rev. Lett.* 51:763 (1983)
75. Pandharipande VR, et al. *Phys. Rev. C* 49:789 (1994)
76. Alde DM, et al. *Phys. Rev. Lett.* 51:763 (1990)
77. Gaskell D, et al. (E91-003 collab.) *Phys. Rev. Lett.* 87:202301 (2001)
78. Brown GE, Buballa M, Li Z, Wambach B. *J. Nucl. Phys. A* 593:295 (1995)
79. Kolton DS. *Phys. Rev. C* 57:1210 (1998)
80. Smith JR, Miller GA. *Phys. Rev. Lett.* 91: 212301 (2003)
81. Chen JW, Detmold W. arXiv:hep-ph/0412119
82. Frankfurt LL, Strikman MI, Liuti S. *Phys. Rev. Lett.* 65:1725 (1990)
83. Eskola KJ. *Nucl. Phys. B* 400:240 (1993)
84. Eskola KJ, Kolhinen VJ, Ruuskanen PV. *Nucl. Phys. B* 535:351 (1998)
85. Eskola KJ, Kolhinen VJ, Salgado CA, Thews RL. *Eur. Phys. J. C* 21:613 (2001)
86. Eskola KJ, Honkanen H, Kolhinen VJ, Salgado CA. arXiv:hep-ph/0302170
87. de Florian D, Sassot R. *Phys. Rev. D* 69: 074028 (2004)
88. Leitch MJ, et al. (E772 and E789 Collabs.) *Nucl. Phys. A* 544:197C (1992)
89. Naples D, et al. (NuTeV collab.) arXiv: hep-ex/0307005
90. Gribov VN. arXiv:hep-ph/0006158
91. Abramovsky VA, Gribov VN, Kancheli OV. *Yad. Fiz.* 18:595 (1973); *Sov. J. Nucl. Phys.* 18:308 (1974)
92. Armesto N, Capella A, Kaidalov AB, Lopez-Albacete J, Salgado CA. *Eur. Phys. J. C* 29:531 (2003)
93. Frankfurt L, Guzey V, McDermott M, Strikman M. *JHEP* 0202:027 (2002)
94. Gribov LV, Levin EM, Ryskin MG. *Phys. Rept.* 100:1 (1983)
95. Mueller AH, Qiu JW. *Nucl. Phys. B* 268: 427 (1986)
96. Freund A, Rummukainen K, Weigert H, Schäfer A. *Phys. Rev. Lett.* 90:222002 (2003)
97. Frankfurt LL, Strikman MI. *Phys. Rept.* 160:235 (1988)
98. Piller G, Weise W. *Phys. Rept.* 330:1 (2000)
99. Jalilian-Marian J, Wang XN. *Phys. Rev. D* 63:096001 (2001)
100. Eskola KJ, Honkanen H, Kolhinen VJ, Qiu JW, Salgado CA. *Nucl. Phys. B* 660: 211 (2003)
101. Goussset T, Pirner HJ. *Phys. Lett. B* 375: 349 (1996)
102. Adler SS, et al. (PHENIX collab.) *Phys. Rev. Lett.* 94:082302 (2005)
103. Ablikim M, et al. (STAR collab.) arXiv:nucl-ex/0408016; Rakness G (STAR collab.) arXiv:nucl-ex/0505062
104. Back BB, et al. (PHOBOS collab.) *Phys. Rev. C* 70:061901 (2004)
105. Arsene I, et al. (BRAHMS collab.) *Phys. Rev. Lett.* 93:242303 (2004)
106. Brodsky SJ. In Proc. 13th Int. Symp. Multiparticle Dynamics, ed. Kittel W, Metzger W, Stergiou A, p. 963. Singapore: World Sci. (1982)
107. Mueller AH. In Proc. of the 17th Rencontres de Moriond, ed. Tran Thanh Van J., Vol. 1, p. 13. Gif-sur-Yvette, France: Editions Frontieres (1982)
108. Jain P, Pire B, Ralston JP. *Phys. Rept.* 271:67 (1996)
109. Frankfurt L, Miller GA, Strikman MI. *Phys. Lett. B* 304:1 (1993)
110. Brodsky SJ, Frankfurt L, Gunion JF,

- Mueller AH, Strikman MI. *Phys. Rev. D* 50:3134 (1994)
111. Sokoloff MD, et al. (Fermilab Tagged Photon Spectrometer collab.) *Phys. Rev. Lett.* 57:3003 (1986)
112. Aitala EM, et al. (E791 collab.) *Phys. Rev. Lett.* 86:4773 (2001)
113. Brodsky SJ, Mueller AH. *Phys. Lett.* B206:685 (1988)
114. Frankfurt LL, Strikman MI. *Phys. Rept.* 160:235 (1988)
115. Kopeliovich BZ, Nemchik J, Nikolaev NN, Zakharov BG. *Phys. Lett.* B309:179 (1993)
116. Adams MR, et al. (E665 collab.) *Phys. Rev. Lett.* 74:1525 (1995)
117. Baier R, Schiff D, Zakharov BG. *Annu. Rev. Nucl. Part. Sci.* 50:37 (2000); Kopeliovich BZ, Tarasov AV, Schäfer A. *Phys. Rev. C* 59:1609 (1999)
118. McGaughey PL, Moss JM, Peng JC. *Annu. Rev. Nucl. Part. Sci.* 49:217 (1999)
119. Leitch ML. (E866 collab.) *New Measurements of the Nuclear Dependence of the and Resonances in High-energy Proton-Nucleus Collisions*. Presented at the Amer. Phys. Soc. Mtg., Long Beach, Calif. May (2000)
120. Naples D, et al. (E683 collab.) *Phys. Rev. Lett* 72:2341 (1994)
121. Cronin JW, et al. *Phys. Rev. Lett* 31:1426 (1973)
122. Krzywicki A, Engels J, Petersson B, Sukhatme U. *Phys. Lett.* B85:407 (1979)
123. Kopeliovich BZ, Nemchik J, Predazzi E, Hayashigaki A. *Nucl. Phys.* A740:211 (2004)
124. Airapetian A, et al. (HERMES collab.) *Eur. Phys. J. C* 20:479 (2001)
125. Adams MR, et al. (E665 collab.) *Phys. Rev. D* 50:1836 (1994)
126. Ashman J, et al. (European Muon collab.) *Z. Phys. C* 52:1 (1991)
127. Burkot W, et al. (BEBC WA21/WA59 Collabs.) *Z. Phys. C* 70:47 (1996)
128. Strikman MI, Tverskoi MG, Zhalov MB. *Phys. Lett.* B459:37 (1999)
129. Adams MR, et al. (E665 collab.) *Phys. Rev. Lett.* 74:5198 (1995); *Phys. Rev. Lett.* 80:2020 (1995)
130. Falter T, Cassing W, Gallmeister K, Mosel U. *Phys. Lett.* B594:61 (2004)
131. Wang E, Wang XN. *Phys. Rev. Lett.* 89:162301 (2002)
132. Accardi A, Muccifora V, Pirner HJ. *Nucl. Phys.* A720:131 (2003)
133. Cassing W, Gallmeister K, Greiner CJ. *Nucl. Phys.* G30:S801 (2004)
134. Osborne J, Wang XN. *Nucl. Phys.* A710:281 (2002)
135. Majumder A, Wang E, Wang XN. arXiv:nucl-th/0412061
136. Abt I, Caldwell A, Liu X, Sutiak J. arXiv:hep-ex/0407053
137. <http://www.jlab.org/12GeV/>
138. Farrar GR, Jackson DR. *Phys. Rev. Lett.* 35:1416 (1975); Brodsky SJ, Burkardt M, Schmidt I. *Nucl. Phys.* B441:197 (1995)
139. Close FE. *Phys. Lett.* B43:422 (1973)
140. Melnitchouk W, Ent R, Keppel C. *Phys. Rept.* 406:127 (2005)
141. Galfi L, Kuti J, Patkos A. *Phys. Lett.* B31:465 (1970); Heimann RL. *Nucl. Phys.* B64:429 (1973); Ellis J, Karliner M. *Phys. Lett.* B213:73 (1988); Close FE, Roberts RG. *Phys. Rev. Lett.* 60:1471 (1988)
142. Ball RD, Forte S, Ridolfi G. *Nucl. Phys.* B444:287 (1995); *Nucl. Phys.* B449:680 (1995)
143. Altarelli G, Ball RD, Forte S, Ridolfi G. *Acta Phys. Polon.* B29:1145 (1998); Gehrman T, Stirling WJ. *Phys. Lett.* B365:347 (1996)
144. Bass S, De Roeck A. *Eur. Phys. J. C* 18:531 (2001)
145. Deshpande A. *Proc. Yale-eRHIC Workshop*, BNL Report 52592 (2000)
146. Adeva B, et al. (Spin Muon Collab.) *Phys. Rev. D* 58:112002 (1998)
147. Bartels J, Ermolaev BI, Ryskin MG. *Z. Phys. C* 70:273 (1996); *Z. Phys. C* 72:627 (1996); Ermolaev B, Greco M, Troyan SI. *Phys. Lett.* B579:321 (2004)

148. Blümlein J, Vogt A. *Phys. Lett.* B370:149 (1996); *Phys. Lett.* B386:350 (1996)
149. Kiyo Y, Kodaira J, Tochimura H. *Z. Phys. C* 74:631 (1997)
150. Kwiecinski J, Ziaja B. *Phys. Rev. D* 60:054004 (1999); Badelek B, Kwiecinski J. *Phys. Lett.* B418:229 (1998); Badelek B, Kiryluk J, Kwiecinski J. *Phys. Rev. D* 61:014009 (2000)
151. Igo G. *Proc. Yale-eRHIC Workshop*, BNL Report 52592 (2000)
152. Stratmann M, Vogelsang W, Weber A. *Phys. Rev. D* 53:138 (1996)
153. Wray D. *Nuov. Cim.* 9A:463 (1972); Derman E. *Phys. Rev. D* 7:2755 (1973); Josphipura AS, Roy P. *Ann. Phys.* 104:460 (1977); Lampe B. *Phys. Lett.* B227:469 (1989); Vogelsang W, Weber A. *Nucl. Phys.* B362:3 (1991); Mathews P, Ravindran V. *Phys. Lett.* B278:175 (1992); *Int. J. Mod. Phys.* A7:6371 (1992); Ravishankar V. *Nucl. Phys.* B374:309; Blümlein J, Kochelev N. *Phys. Lett.* B381:296 (1996)
154. Contreras J, De Roeck A, Maul M. arXiv: hep-ph/9711418
155. Gehrmann T, Stirling WJ. *Phys. Rev. D* 53:6100 (1996)
156. Kinney ER, Stössl U. *AIP Conf. Proc.* 588:171 (2001)
157. Koike Y, Nagashima J. *Nucl. Phys.* B660:269 (2003)
158. Meng R, Olness FI, Soper DE. *Nucl. Phys.* B371:79 (1992); *Phys. Rev. D* 54:1919 (1996); Nadolsky P, Stump DR, Yuan CP. *Phys. Rev. D* 64:114011 (2001); *Phys. Lett.* B515:175 (2001)
159. Derrick M, et al. (ZEUS Collab.) *Z. Phys. C* 70:1 (1996); Adloff C, et al. (H1 Collab.) *Eur. Phys. J. C* 12:595 (2000)
160. Lichtenstadt J. *Nucl. Phys. B* (Proc. Suppl.) 105:86 (2002)
161. Watson AD. *Z. Phys. C* 12:123 (1982); Glück M, Reya E. *Z. Phys. C* 39:569 (1988); Guillet JPh. *Z. Phys. C* 39:75 (1988); Frixione S, Ridolfi G. *Phys. Lett.* B383:227 (1996); Bojak I, Stratmann M. *Phys. Lett.* B433:411 (1998); *Nucl. Phys.* B540:345 (1999)
162. Altarelli G, Stirling WJ. *Particle World* 1:40 (1989)
163. Glück M, Reya E, Vogelsang W. *Nucl. Phys.* B351:579 (1991)
164. Carlitz RD, Collins JC, Mueller AH. *Phys. Lett.* B214:229 (1988); Kunszt Z. *Phys. Lett.* B218:243 (1989); Vogelsang W. *Z. Phys. C* 50:275 (1991); Manohar A. *Phys. Lett.* B255:579 (1991)
165. Aid S, et al. (H1 Collab.) *Nucl. Phys.* B449:3 (1995); Wobisch M. (H1 collab.) *Nucl. Phys. Proc. Suppl.* 79:478 (1999); Hadig T. (ZEUS collab.) Presented at the 8th Int. Workshop on Deep Inelastic Scattering and QCD (DIS 2000), Liverpool, England, April (2000), arXiv:hep-ex/0008027
166. Rädcl G. *Proc. Yale-eRHIC Workshop*, BNL Report 52592 (2000); De Roeck A, Rädcl G. *Nucl. Phys. B* (Proc. Suppl.) 105:90 (2002)
167. Mirkes E, Zeppenfeld D. *Phys. Lett.* B380:205 (1996)
168. Lichtenstadt J. *Proc. Yale-eRHIC Workshop*, BNL Report 52592 (2000)
169. De Roeck A, Deshpande A, Hughes VW, Lichtenstadt J, Rädcl G. *Eur. Phys. J. C* 6:121 (1999)
170. Klasen M. *Rev. Mod. Phys.* 74:1221 (2002)
171. Nisius R. *Phys. Rept.* 332:165 (2000)
172. Irving AC, Newland DB. *Z. Phys. C* 6:27 (1980); Hassan JA, Pilling DJ. *Nucl. Phys.* B187:563 (1981); Xu ZX. *Phys. Rev. D* 30:1440 (1984); Bass SD. *Int. J. Mod. Phys.* A7:6039 (1992); Narison S, Shore GM, Veneziano G. *Nucl. Phys.* B391:69 (1993); Bass SD, Brodsky SJ, Schmidt I. *Phys. Lett.* B437:417 (1998)
173. Glück M, Vogelsang W. *Z. Phys. C* 55:353 (1992); *Z. Phys. C* 57:309 (1993); Glück M, Stratmann M, Vogelsang W. *Phys. Lett.* B337:373 (1994)
174. Stratmann M, Vogelsang W. *Proc. Yale-eRHIC Workshop*, BNL Report 52592 (2000); Stratmann M, Vogelsang W. *Z.*

- Phys. C* 74:641 (1997); Butterworth JM, Goodman N, Stratmann M, Vogelsang W. arXiv:hep-ph/9711250
175. Jäger B, Stratmann M, Vogelsang W. *Phys. Rev. D* 68:114018 (2003)
176. Adloff C, et al. (H1 collab.) *Eur. Phys. J. C* 1:97 (1998)
177. Combridge BL, Maxwell CJ. *Nucl. Phys.* B239:429 (1984)
178. Stratmann M, Vogelsang W. arXiv:hep-ph/9907470
179. Drell SD, Hearn AC. *Phys. Rev. Lett.* 162:1520 (1966); Gerasimov SB. *Yad. Fiz.* 2:839 (1965)
180. Helbing K. (GDH collab.) *AIP Conf. Proc.* 675:33 (2003); Ahrens J. et al. (GDH Collab.) *Phys. Rev. Lett* 87:022003 (2001)
181. Deshpande A (for Sandacz A). *Acceptance studies for DVCS and DES physics using PP2PP roman pots in eRHIC hadron beam lattice*. Presented at the EIC Conf., Jefferson Lab, Newport News, Virginia, April (2004)
182. Collins JC. *Phys. Rev. D* 57:3051 (1998); *Phys. Rev. D* 61:019902 (1998)
183. Grazzini M, Trentadue L, Veneziano G. *Nucl. Phys.* B519:394 (1998)
184. Kuraev EA, Lipatov LN, Fadin VS. *Sov. Phys. JETP* 45:199 (1977); Balitsky II, Lipatov LN. *Sov. J. Nucl. Phys.* 28:822 (1978)
185. Iancu E, Venugopalan R. arXiv:hep-ph/0303204, in *Quark Gluon Plasma 3*, ed. R Hwa, XN Wang. Singapore: World Sci. (2004)
186. Sloan T. *Proc. Yale-eRHIC Workshop*, BNL Report BNL-52592 (2000)
187. Armesto N, Salgado CA. arXiv:hep-ph/0301200
188. Hirai M, Kumano K, Miyama M. *Phys. Rev. D* 64:034003 (2001)
189. Eskola KJ, Kolhinen VJ, Salgado CA. *Eur. Phys. J. C* 9:61 (1999)
190. Huang Z, Lu HJ, Sarcevic I. *Nucl. Phys.* A637:79 (1998)
191. Armesto N. *Eur. Phys. J. C* 26:35 (2002)
192. Wang XN, Li SY. *Phys. Lett. B* 527:85 (2002)
193. McLerran L, Venugopalan R. *Phys. Rev. D* 49:2233 (1994); *Phys. Rev. D* 49:3352 (1994); *Phys. Rev. D* 50:2225 (1994)
194. Berera A, Soper DE. *Phys. Rev. D* 53:6162 (1996)
195. Arneodo M, et al. In *Proc. Future Physics at HERA*, DESY, September arXiv:hep-ph/9610423 (1995)
196. Alvero L, Collins JC, Terron J, Whitmore JJ. *Phys. Rev. D* 59:074022 (1999)
197. Kovchegov YV, Mueller AH. *Nucl. Phys.* B529:451 (1998)
198. Johnson MB, et al. *Phys. Rev. C* 65:025203 (2002)
199. Cano F, Pire B. *Eur. Phys. J. A* 19:423 (2004)
200. Martin AD, Ryskin MG. *Phys. Rev. D* 64:094017 (2001)
201. Susskind L. *Phys. Rev.* 65:1535 (1968)
202. Jalilian-Marian J, Kovner A, Leonidov A, Weigert H. *Nucl. Phys.* B504:415 (1997); *Phys. Rev. D* 59:014014 (1999); Kovner A, Milhano G, Weigert H. *Phys. Rev. D* 62:114005 (2000); Jalilian-Marian J, Kovner A, McLerran LD, Weigert H. *Phys. Rev. D* 55:5414 (1997); Iancu E, Leonidov A, McLerran LD. *Nucl. Phys.* A692:583 (2001); *Phys. Lett.* B510:133 (2001); Ferreiro E, Iancu E, Leonidov A, McLerran LD. *Nucl. Phys.* A703:489 (2002)
203. Mueller AH. arXiv:hep-ph/9911289; McLerran LD. *Acta Phys. Polon.* B34:5783 (2003); Armesto N. *Acta Phys. Polon.* B35:213 (2004); Stasto AM. *Acta Phys. Polon.* B35:3069 (2004)
204. Rummukainen K, Weigert H. *Nucl. Phys.* A739:183 (2004)
205. Iancu E, Triantafyllopoulos DN. *Phys. Lett.* B610 (2005); Mueller AH, Shoshi AI, Wong SMH. *Nucl. Phys.* B715:440 (2005); Kovner A, Lublinsky M. *Phys. Rev. D* 71:085004 (2005)
206. Balitsky I. *Nucl. Phys.* B463:99 (1996); Kovchegov YV. *Phys. Rev. D* 61:074018 (2000)
207. Mueller AH. *Nucl. Phys.* B415:373 (1994)

- 
208. Nikolaev NN, Zakharov BG. *Z. Phys. C* 49:607 (1991)
209. Levin EM, Tuchin K. *Nucl. Phys. B*573: 833 (2000)
210. Iancu E, Itakura K, McLerran LD. *Nucl. Phys. A*724:181 (2003)
211. Mueller AH, Triantafyllopoulos DN. *Nucl. Phys. B*640:331 (2002)
212. Munier S, Peschanski R. *Phys. Rev. Lett.* 91:232001 (2003); *Phys. Rev. D* 69:034008 (2004); *Phys. Rev. D* D70: 077503 (2004)
213. Braun MA. arXiv:hep-ph/0101070; Armesto N, Braun MA. *Eur. Phys. J. C* 20: 517 (2001)
214. Albacete JL, Armesto N, Milhano G, Salgado CA, Wiedemann UA. *Phys. Rev. D* 71:014003 (2005)
215. Golec-Biernat K, Motyka L, Stasto AM. *Phys. Rev. D* 65:074037 (2002)
216. Triantafyllopoulos DN. *Nucl. Phys. B*648: 293 (2003)
217. Iancu E, Itakura K, Munier S. *Phys. Lett. B*590:199 (2004)
218. Forshaw JR, Shaw G. *JHEP* 0412:052 (2004)
219. Mueller AH. *Nucl. Phys. A*724:223 (2003)
220. Kovchegov YV, Tuchin K. *Phys. Rev. D* 65:074026 (2002)
221. Albacete JL, et al. arXiv:hep-ph/0502167
222. Levin EM, Lublinsky M. *Nucl. Phys. A*730:191 (2004)
223. Rogers T, Guzey V, Strikman MI, Zu X. *Phys. Rev. D* 69:074011 (2004)
224. Ivanov IP, Nikolaev NN, Savin AA. arXiv:hep-ph/0501034
225. Levin EM, Lublinsky M. *Nucl. Phys. A*712:95 (2002)
226. Frankfurt L, Guzey V, Strikman MI. *Phys. Lett. B*586:41 (2004)
227. Kovchegov YV, Levin E, McLerran LD. *Phys. Rev. C* 63:024903 (2001)
228. Guzey V, Strikman M, Vogelsang W. *Phys. Lett. B*603:173 (2004)
229. Dumitru A, Jalilian-Marian J. *Phys. Rev. Lett.* 89:022301 (2002)
230. Gelis F, Jalilian-Marian J. *Phys. Rev. D* 66:094014 (2002); *Phys. Rev. D* 66: 014021 (2002)
231. Blaizot JP, Gelis F, Venugopalan R. *Nucl. Phys. A*743:13 (2004)
232. Accardi A. arXiv:hep-ph/0212148; Accardi A, Gyulassy M. *Phys. Lett. B*586: 244 (2004)
233. Kharzeev D, Kovchegov YV, Tuchin K. *Phys. Rev. D* 68:094013 (2003); Baier R, Kovner A, Wiedemann UA. *Phys. Rev. D* 68:054009 (2003); Albacete JL, et al. *Phys. Rev. Lett.* 92:082001 (2004); Jalilian-Marian J, Nara Y, Venugopalan R. *Phys. Lett. B*577:54 (2003); Iancu E, Itakura K, Triantafyllopoulos DN. *Nucl. Phys. A*742:182 (2004)
234. Kharzeev D, Levin EM, McLerran LD. *Nucl. Phys. A*748:627 (2005)
235. Ogawa A. (STAR collab.) arXiv:nucl-ex/0408004
236. Qiu JW, Vitev I. arXiv:hep-ph/0405068; Hwa RC, Yang CB, Fries RJ. *Phys. Rev. C* 71:024902 (2005); Kopeliovich BZ, et al. arXiv:hep-ph/0501260
237. Baier R, Mueller AH, Schiff D. *Nucl. Phys. A*741:358 (2004); Betemps MA, Gay Ducati MB. *Phys. Rev. D* 70:116005 (2004); Jalilian-Marian J. *Nucl. Phys. A*739:319 (2004)
238. Catani S, Ciafaloni M, Hautmann F. *Nucl. Phys. B*366:135 (1991); Collins JC, Ellis RK. *Nucl. Phys. B*360:3 (1991)
239. Kharzeev D, Kovchegov YV, Tuchin K. *Phys. Rev. D* 68:094013 (2003)
240. Blaizot JP, Gelis F, Venugopalan R. *Nucl. Phys. A*743:57 (2004); Gelis F, Venugopalan R. *Phys. Rev. D* 69:014019 (2004)
241. Nikolaev NN, Schäfer W. *Phys. Rev. D* 71:014023 (2005); Nikolaev NN, Schäfer W, Zakharov BG. arXiv:hep-ph/0502018
242. Jalilian-Marian J, Kovchegov YV. *Phys. Rev. D* 70:114017 (2004)
243. Kovner A, Wiedemann UA. *Phys. Rev. D* 64:114002 (2001)
244. Jalilian-Marian J, Kovchegov YV. arXiv: hep-ph/0505052

245. Kopeliovich BZ, Raufeisen J, Tarasov AV, Johnson MB. *Phys. Rev. C* 67:014903 (2003)
246. Krasnitz A, Venugopalan R. *Nucl. Phys. B* 557:237 (1999); *Phys. Rev. Lett.* 84:4309 (2000); *Phys. Rev. Lett.* 86:1717 (2001)
247. Krasnitz A, Nara Y, Venugopalan R. *Phys. Rev. Lett.* 87:192302 (2001); *Nucl. Phys. A* 717:268 (2003)
248. Lappi T. *Phys. Rev. C* 67:054903 (2003); Krasnitz A, Nara Y, Venugopalan R. *Nucl. Phys. A* 727:427 (2003)
249. Armesto N, Pajares C. *Int. J. Mod. Phys. A* 15:2019 (2000)
250. Kharzeev D, Nardi M. *Phys. Lett. B* 507:121 (2001); Kharzeev D, Levin EM. *Phys. Lett. B* 523:79 (2001); Kharzeev D, Levin EM, Nardi M. arXiv:hep-ph/0111315
251. Kharzeev D, Levin EM, McLerran LD. *Phys. Lett. B* 561:93 (2003)
252. Krasnitz A, Nara Y, Venugopalan R. *Phys. Lett. B* 554:21 (2003)
253. Huovinen P. arXiv:nucl-th/0305064
254. Hirano T, Nara Y. *Nucl. Phys. A* 743:305 (2004)
255. *The eRHIC Zero<sup>th</sup> Order Design Report*, ed. M Farkhondeh, V Ptitsyn. BNL Report C-A/AP/142, March (2004)
256. Merminga L, Derbenev Y. *AIP Conf. Proc.* 698:811 (2004)
257. Koop I, et al. *Electron Cooling for RHIC*. Presented at the IEEE Particle Accelerator Conference (PAC2001), Chicago, June 2001; *Proc. IEEE Particle Accelerator Conference (PAC2001)*, ed. P Lucas, S Webber, Chicago, June (2001); Parkhomchuk VV, Ben-Zvi I. *Electron Cooling for RHIC Design Report*, BNL Report C-A/AP/47 (2001)
258. Ben-Zvi I, et al. *Nucl. Instrum. Meth. A* 532:177 (2004)
259. Farkhondeh M. Polarized electron sources for a linac-ring electron-ion collider. In *Proc. EIC Accelerator Workshop*, ed. M Davis, A Deshpande, S Ozaki, R Venugopalan. BNL Report-52663-V.1 (2002)
260. Abramowicz H, Caldwell A. *Rev. Mod. Phys.* 71:1275 (1999)



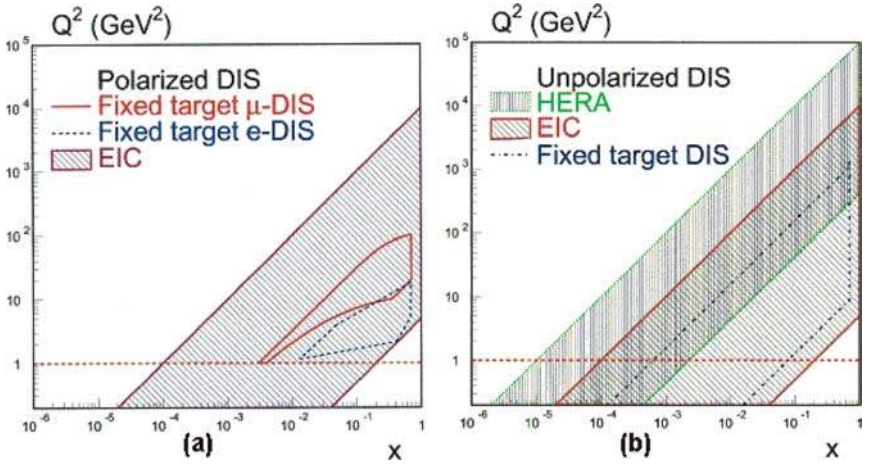


**Figure 2** The  $x$ - $Q^2$  range of the proposed lepton-ion collider at Brookhaven National Laboratory (eRHIC) in comparison with the past and present experimental DIS facilities. The left plot is for polarized DIS experiments, and the right corresponds to the unpolarized DIS experiments.

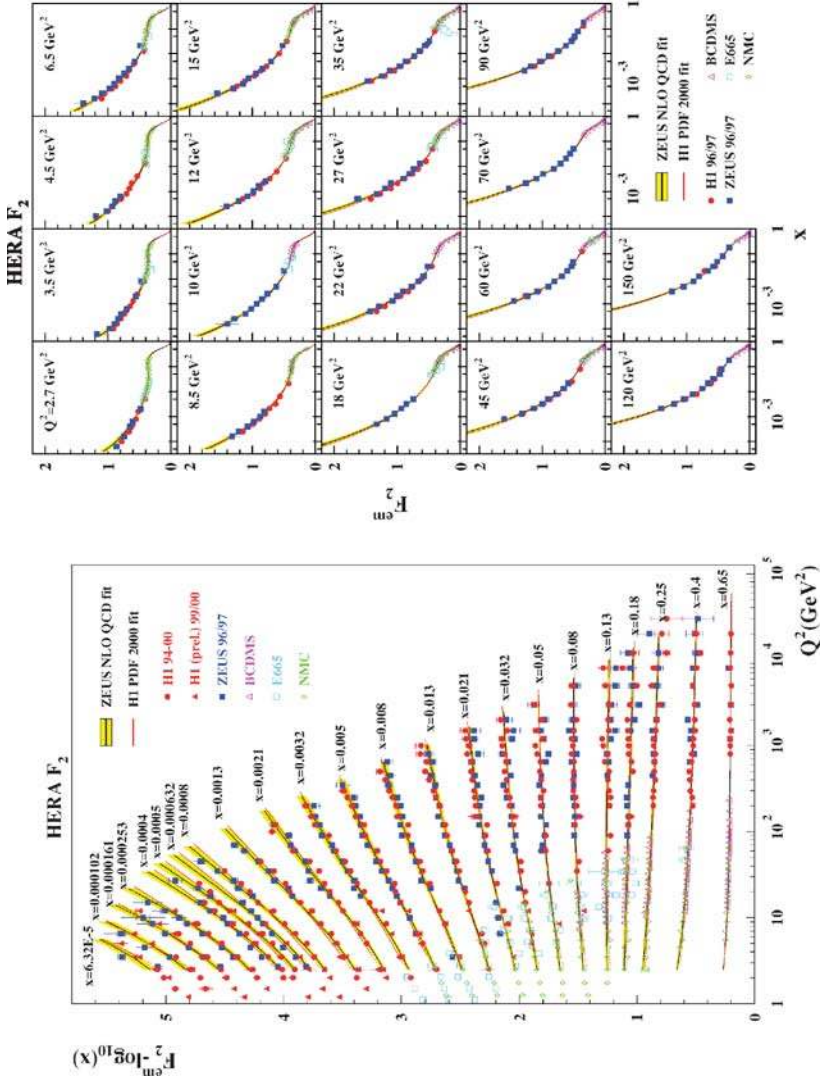


**Figure 4** The plot on the left shows the world data on  $F_2$  as a function of  $Q^2$  for fixed values of  $x$ . On the right we show the converse:  $F_2$  as a function of  $x$  for fixed values of  $Q^2$ . From (8).

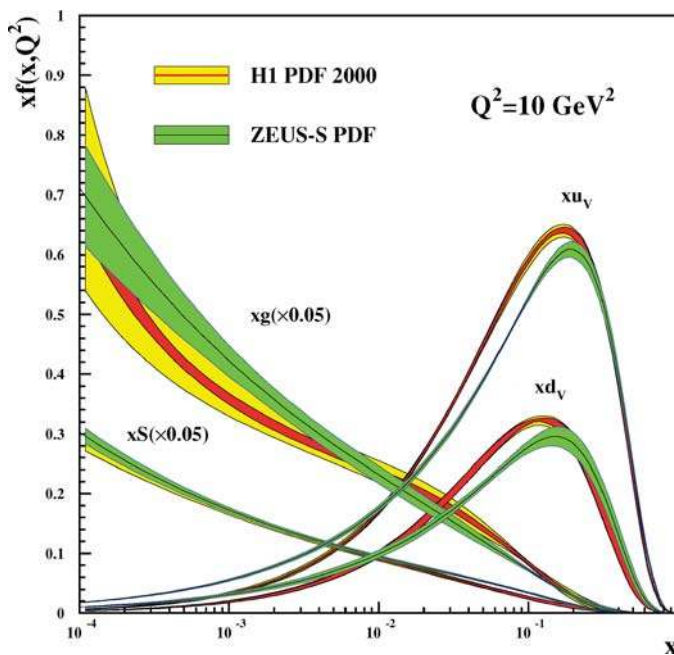


**Figure 5** The valence (up and down) quark, sea quark, and gluon distributions plotted as a function of  $x$  for fixed  $Q^2 = 10 \text{ GeV}^2$ . Note that the sea and glue distributions are scaled down by a factor of  $1/20$ . From (8).

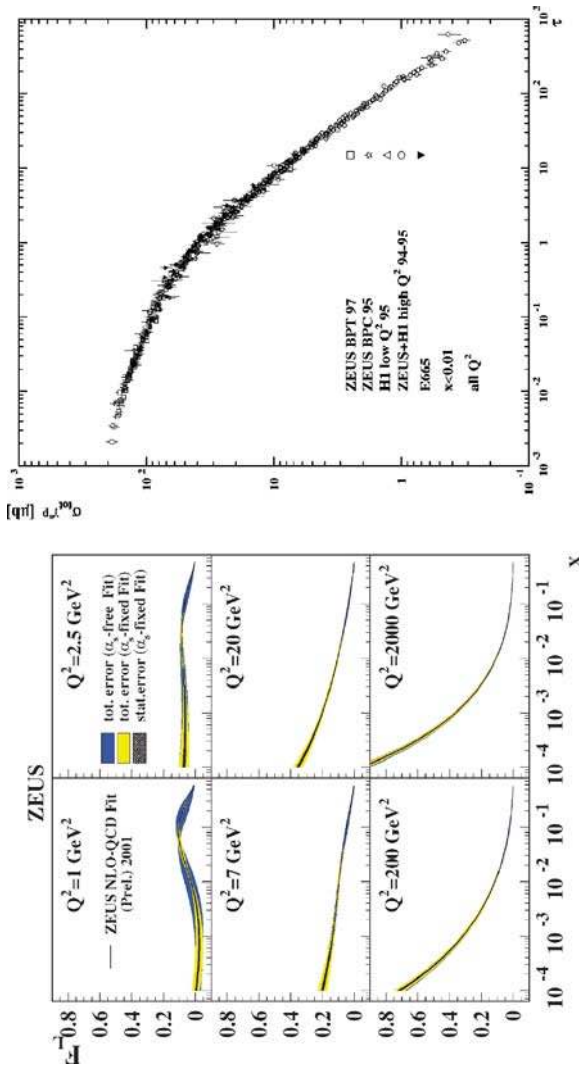


**Figure 6** The plot on the left shows the longitudinal structure function  $F_L$  as a function of  $x$  for different  $Q^2$  bins (9). On the right (from Ref. 12) is a plot of the virtual photon-proton cross-section plotted as a function of  $\tau = Q^2/Q_s^2$ . See text for further explanation.

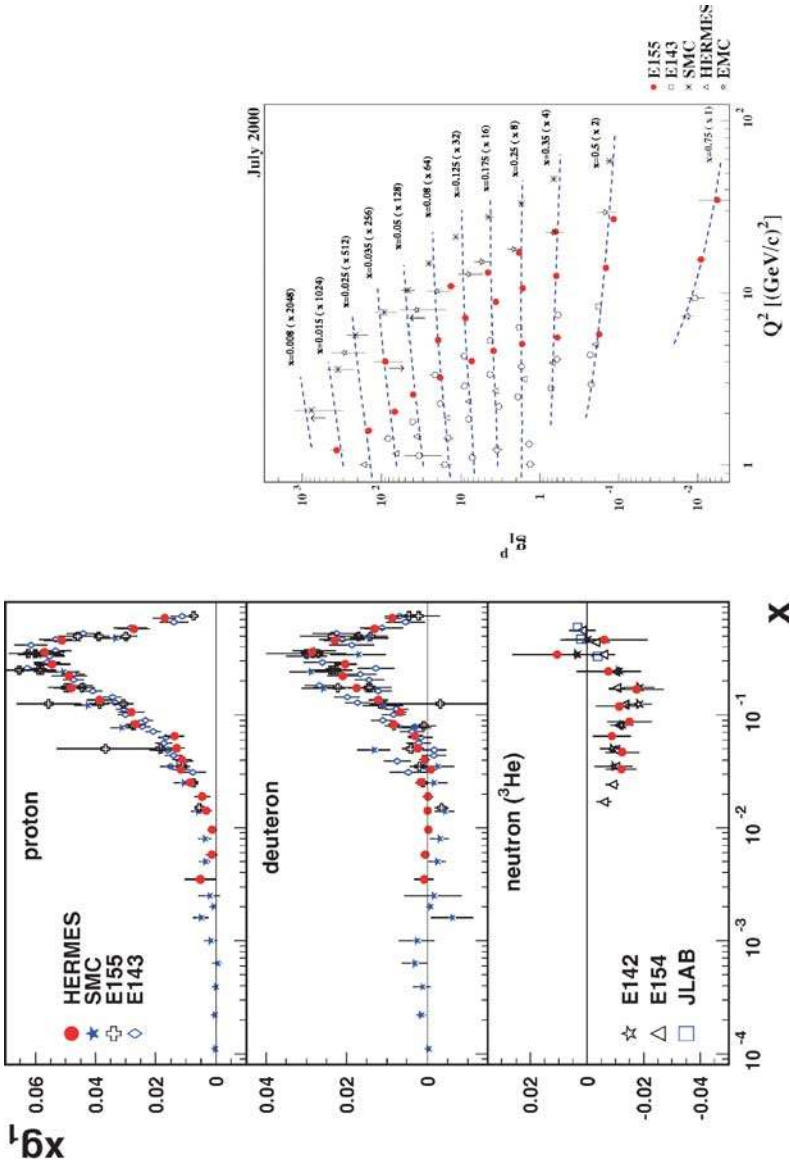


**Figure 7** Left: world data on the spin structure function  $g_1$  as compiled and shown in (21). Right:  $g_1(x, Q^2)$  as a function of  $Q^2$  for various  $x$ . The curves are from a phenomenological fit. Taken from (22).

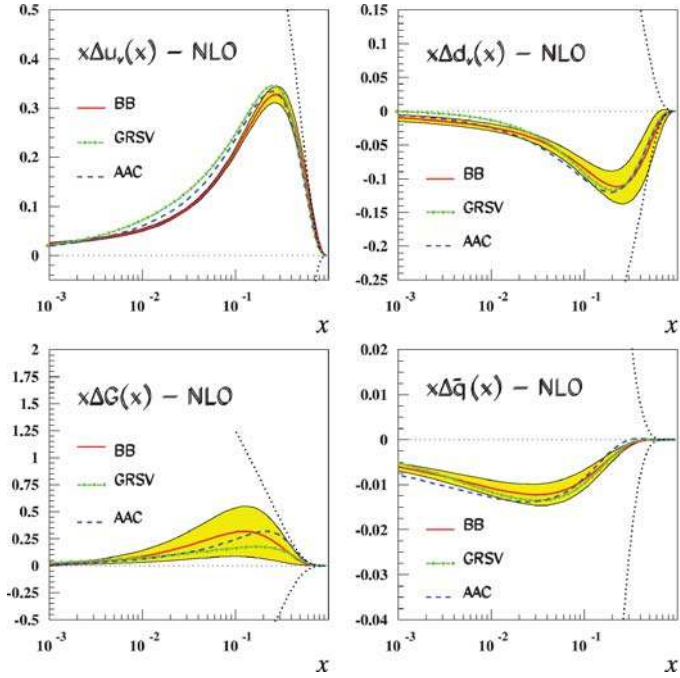


**Figure 8** Recent analysis of polarized parton densities of the proton. Taken from (25) (“BB”). The additional curves represent the central fits from the analyses of (26) (“GRSV”) and (27) (“AAC”).

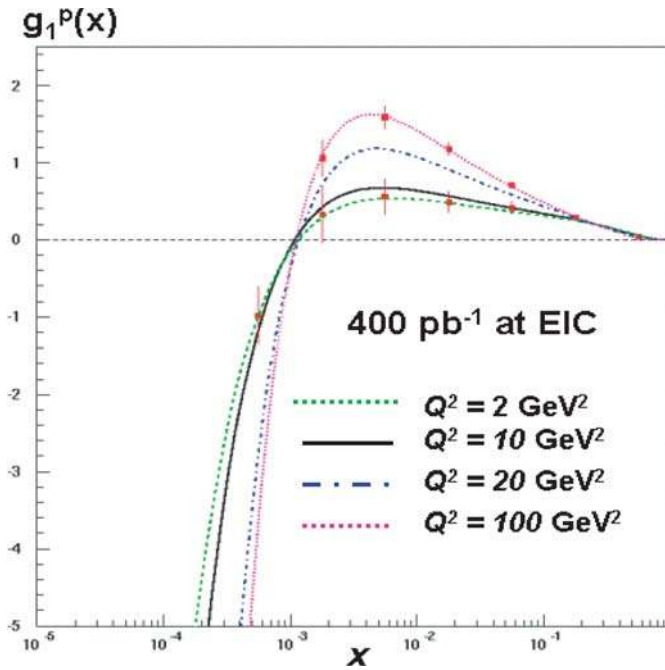


**Figure 16** Possible eRHIC data (statistical accuracy) with  $250 \times 10$  GeV collisions are shown for  $400 \text{ pb}^{-1}$ . Also shown is the evolution of  $g_1(x, Q^2)$  at low  $x$  for different values of  $Q^2$  for a positive gluon polarization (31, 146).

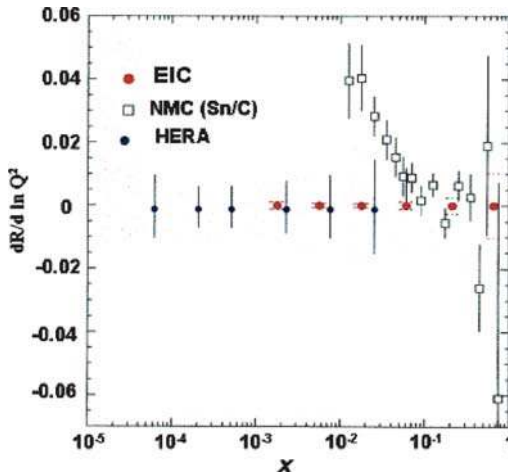


**Figure 23** The projected statistical accuracy of  $\frac{\partial F_1^A/F_2^A}{\partial \ln Q^2}$  as a function of  $x$  for an integrated luminosity of  $1 \text{ pb}^{-1}$  at the EIC (186). The simulated data are compared to previous data from the NMC and to data from a hypothetical e-A collider at HERA energies.

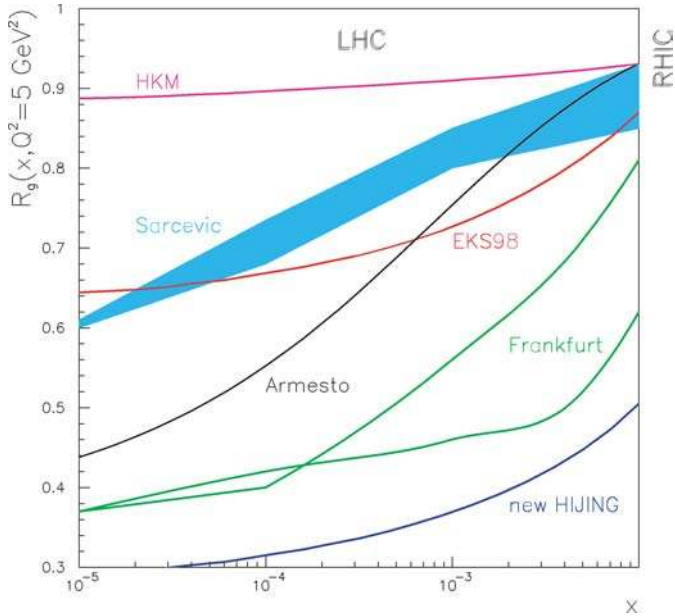


**Figure 24** Ratio of the gluon distribution in Lead to that in a proton, normalized by the number of nucleons, plotted as a function of  $x$  for a fixed  $Q^2 = 5 \text{ GeV}^2$ . From Ref. (187). Captions denote models-HKM (188), EKS98 (189), Sarcevic (190), Armesto (191), Frankfurt (93), Hijing (192). The vertical bands denote the accessible  $x$  regions at central rapidities at RHIC and LHC.



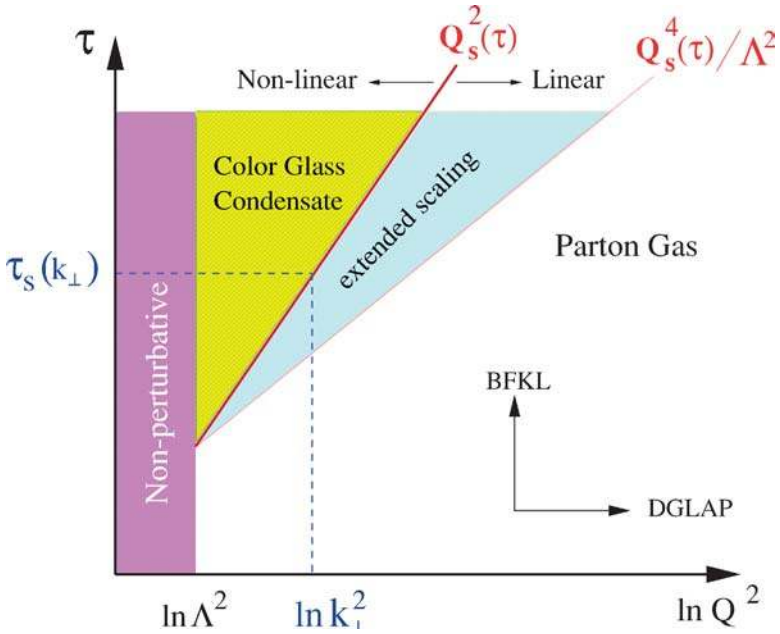


**Figure 26** A schematic plot of the Color Glass Condensate and extended scaling regimes in the  $x$ - $Q^2$  plane. Here  $\tau = \ln(1/x)$  denotes the rapidity. From Ref (185).

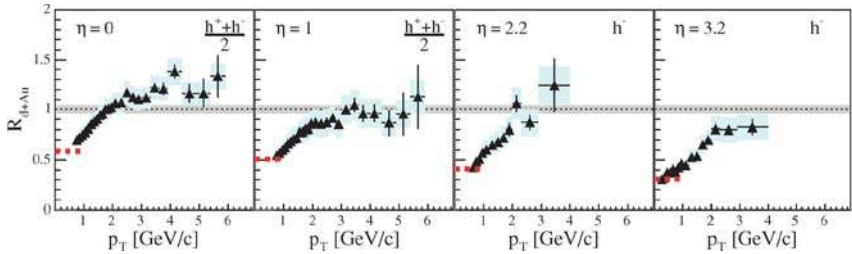


**Figure 27** Depletion of the Cronin peak from  $\eta = 0$  to  $\eta = 3$  for minimum bias events. From Ref. (105).

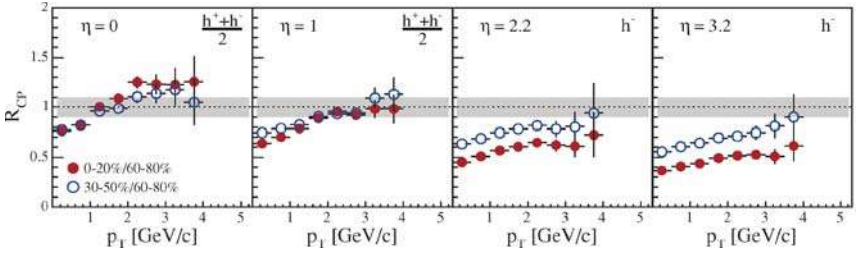


**Figure 28** Centrality dependence of the Cronin ratio as a function of rapidity. From Ref. (105).

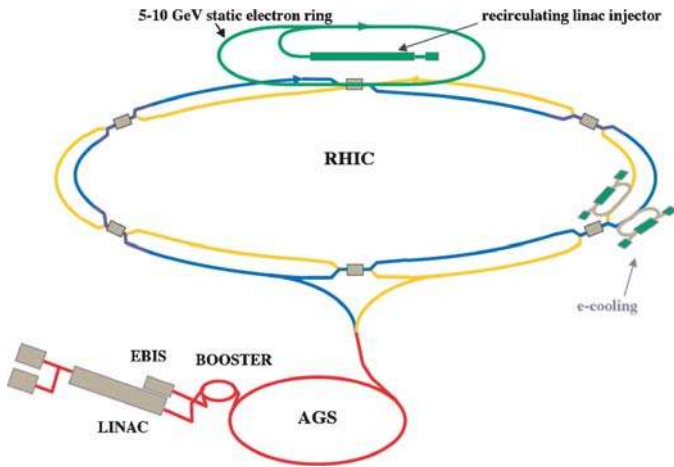


**Figure 29** Schematic layout of the ring-ring eRHIC collider.

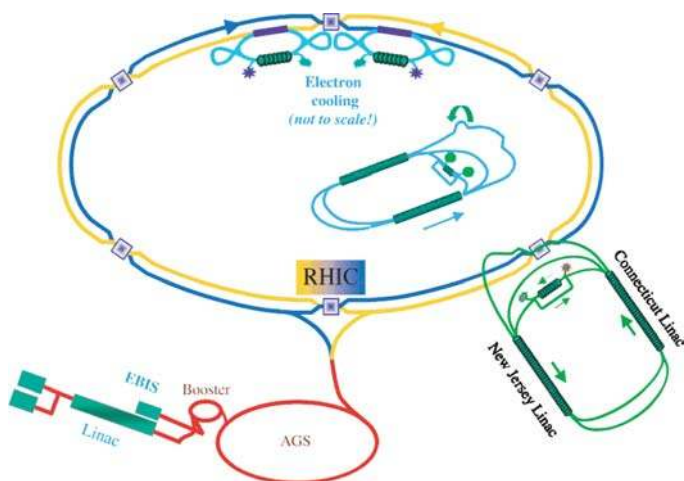


**Figure 30** Schematic layout of a possible linac-ring eRHIC design.

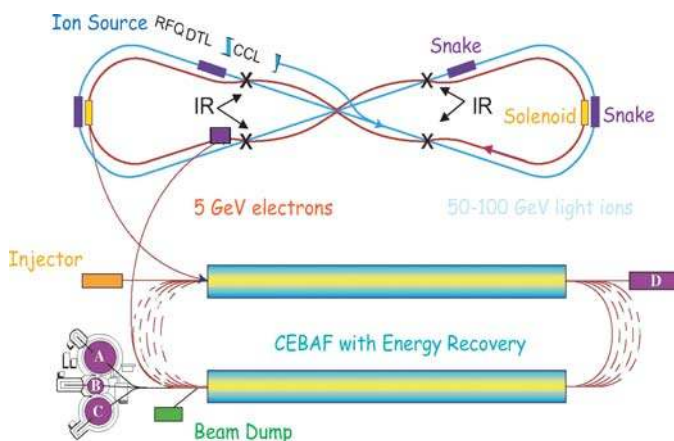


**Figure 31** Schematic layout of a possible electron light ion collider at Jefferson Laboratory.